2014

Advanced graphene-metal oxide nanostructured composites for supercapacitors

Alfred Tawirirana Chidembo
University of Wollongong

UNIVERSITY OF WOLLONGONG

Institute for Superconducting and Electronic Materials

Advanced graphene-metal oxide nanostructured composites for supercapacitors

Alfred Tawirirana Chidembo

This thesis is presented as part of the
requirement for the Award of the Degree of
Doctor of Philosophy
of the
University of
Wollongong

July 2014

ABSTRACT

The development of alternative energy storage systems is undoubtedly one of the greatest challenges facing our modern society as a result of emerging ecological concerns. The ever-increasing environmental concerns and the need for efficient energy storage devices have catapulted research in this field, mainly focused on electric double layer capacitors (EDLC's), also known as supercapacitors, which consist of carbon based materials. The ultimate performance of these devices strongly depends on the intrinsic properties of their constituent materials and their eventual architectural design.

The main focus of this doctoral thesis is to develop high performance supercapacitor electrodes utilising simple and cost effective methods ideal for industrial and commercial use. The materials reported herein are therefore traditional pseudocapacitive metal oxides incorporated onto an electrical double layer material (graphene sheets and carbon nanotubes) to produce a synergistic network with high conductivity. The development of this work stems from previous work where we developed a graphene oxide-carbon nanotube composite for stable and high performance supercapacitor electrodes. It is against this background that the work reported herein was developed to incorporate metal oxides onto large graphene sheets and additionally a ternary system comprising metal oxide nanoparticles, carbon nanotubes and graphene.

In this work, an in-situ spray pyrolysis approach to fabricate different metal oxide-graphene composites with highly porous morphologies for cost-effective high performance supercapacitor devices was used for the first time. An efficient encapsulation of metal oxide particles with graphene oxide (GO) while simultaneously reducing the GO is reported. In the first experiment, a high surface

area (BET surface area of 139 m^2g^{-1}) self–organized, micron sized urchin-like composite made up of reduced graphene oxide (rGO) and needle-shaped manganese oxide (rGO-Mn_2O_3/Mn_3O_4) is reported. Maximum capacitances of 425 Fg^{-1} at 5 mVs^{-1} from a three electrode set up and 133 Fg^{-1} at a current density of 0.2 Ag^{-1} are reported from an asymmetric two electrode set up with graphene as the anode. The composite material also shows capacitance retention of 83% over 1000 cycles. These remarkable performances are attributed to the high specific surface area due to the "urchin-like" hollow structures and synergy between the manganese oxide and reduced graphene oxide materials within the composite. Apart from the outstanding performance, the synthesis technique can be exploited further in the bulk synthesis of cost effective graphene-metal oxide hybrid materials for energy storage applications.

In a development of the first work, composites consisting of NiO and Co_3O_4 and rGO were synthesized and tested. As a result of spray pyrolysis, the composites exhibit unique globular lettuce-like structures comprising NiO or Co_3O_4 nanoparticles embedded between graphene sheets. An impressive overall performance arises from such structures by exploiting the pseudocapacitive nature of the metal oxide and conductive EDLC nature of the rGO. Specific capacitances as high as 687 and 656 Fg^{-1}(three electrode set up) for rGO- Co_3O_4 and rGO-NiO composites were recorded respectively. Based on the same principle a more developed experiment, this time utilising reduced graphene oxide, functionalized multiwalled carbon nanotubes and nickel oxide nanoparticles is reported. Electrodes fabricated from this novel ternary system exhibit exceptionally high capacitance (2074 Fg^{-1} from a three electrode set up) due to the highly conductive network, synergistic link between graphene oxide and carbon nanotubes and achieving high surface area monodispersed NiO decorated rGO/CNTs composite employing the

liquid crystallinity of GO dispersions. To further assess the practicality of this material for supercapacitor manufacture, we assembled an asymmetric supercapacitor device incorporating activated carbon as the anode. The asymmetric supercapacitor device showed remarkable capacity retention (>96%), high energy density (23 $Whkg^{-1}$) and a coulombic efficiency of 99.5%. In all three experiments, the benefits of fabricating composites of EDLC and pseudocapacitive metal oxide nanoparticles are reflected by the high specific capacitances, high energy densities and long cycle life.

ACKNOWLEDGEMENTS

Firstly, I would like to thank God for guiding me and leading me throughout my studies. I would like to express my sincere gratitude to all my colleagues at the Institute for Superconducting and Electronic Materials (ISEM) who supported me during the course of my studies. Thanks to Dr Peleckis and Crystal Mahfouz for being supportive and always willing to take a tea break and offering valuable advice. Special thanks go to my supervisor Dr. Konstantinov and co-supervisor Professor Liu for their academic guidance. In the same breadth, I would like to thank my former supervisor Professor Kenneth Ozoemena who introduced me to this field and has continued to provide direction and support. I would like to thank my family and friends who have stood by me and given me enormous support all the time. Last but not least, I would like to thank my wife Precious for her support and endurance during my studies and conscientiously editing this thesis without any technical know-how of the subject. Such an act can only be inspired by love.

CERTIFICATION

I, Alfred Tawirirana Chidembo declare that this thesis submitted in fulfilment of the requirements for the award of Doctor of Philosophy, in the Institute for Superconducting and Electronic Materials, Faculty of Engineering, University of Wollongong, is entirely my own work unless otherwise referenced or acknowledged. This manuscript has not been submitted for qualifications at any other academic institution.

TABLE OF CONTENTS

LIST OF FIGURES

LIST OF TABLES

1 INTRODUCTION

A technological revolution has been sweeping across the globe over the past few decades. During this time, a host of portable devices ranging from mobile phones, tablets, hand-held tools and GPS have become essential for everyday living as shown in figure 1.1. Although most of these devices largely depend on batteries for prolonged power supply, supercapacitors provide peak current for different power loads thereby reducing stress on the battery. The proliferation in technology has subsequently fuelled interest in the area of supercapacitor and battery research, with a view to produce cheap and sustainable energy storage devices. It is against this background that this work will focus on the development of high performance supercapacitor electrodes using simple materials and cost effective methods.

Supercapacitors, also known as ultracapacitors or electrochemical capacitors (ECs) are charge storage devices that utilize the electrical double layer on the electrode/electrolyte interface to store charges. Their electrodes are usually fabricated using high surface area materials with high porosity and excellent conductivity. Due to these characteristics, supercapacitors are able to charge and discharge quickly resulting in a high power delivery over a short space of time hence their increased use in portable electronics. Figure 1.1 shows the trend in shipments of portable devices and forecasts until 2017, which have a direct impact on the amount of supercapacitors produced. Of particular interest, is the surge in tablet and smartphone shipments over the next few years where they are expected to surpass PC’s by the year 2017 hence the increased activity in energy storage device research.

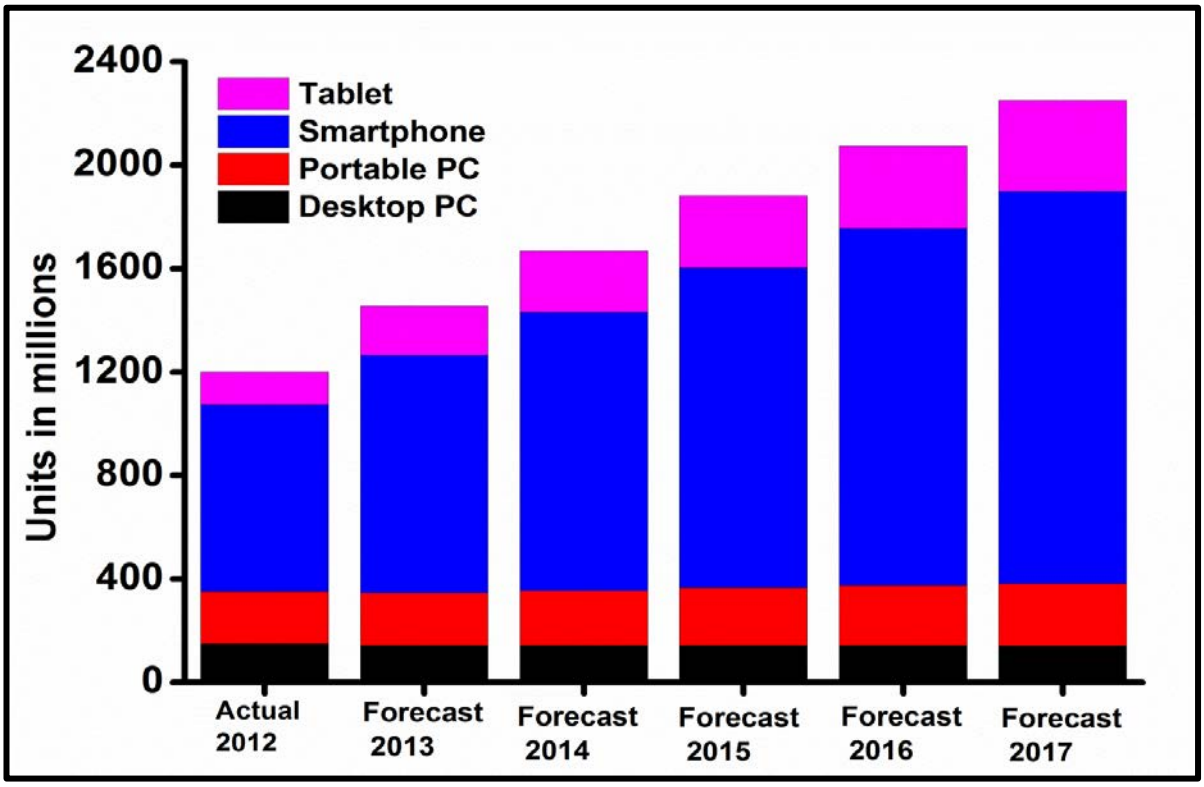

Figure 1.1: Worldwide smart connected device market focus unit shipments (in millions).

(Source: http://www.idc.com/getdoc.jsp?containerId=prUS24037713, September 4, 2013)

Another area, where supercapacitor research has burgeoned is the hybrid electric vehicle (HEV) industry. HEV's typically make use of an internal combustion system and an electric motor driven by energy stored in a battery. Batteries and supercapacitors are employed in these systems to suit the varied energy and power demands. Thus, most HEV's produced nowadays make use of supercapacitors in regenerative braking to harness energy in stop-start situations. All these transformations are due to the drive by most companies to reduce their carbon footprint. While most portable electronic devices mentioned earlier are small and only require small supercapacitors, the power demands in HEV's are much greater due to the size of car engines. In 2005 alone, the supercapacitor market was between US $272 million and $400 million, and has since grown especially in the automotive

sector as suggested by the increase in the number of electric vehicles being produced as shown in figure 1.2.[1] Although batteries can store more energy (high energy density), the rate at which they dispense this energy is very slow. On the other hand, supercapacitors store less energy which they can deliver very quickly (high power density). In light of these limitations of both devices, combinations of supercapacitors with batteries, fuel cells and internal combustion engines (ICE's) are currently being utilized to provide maximum performance of HEV's. To fully understand the sudden growth in supercapacitor research it is important to analyse the production trends of electronic devices that utilise these energy storage devices as shown in figures 1.1 and 1.2. It is also important to look back into the history of the supercapacitor and it's development over the years.

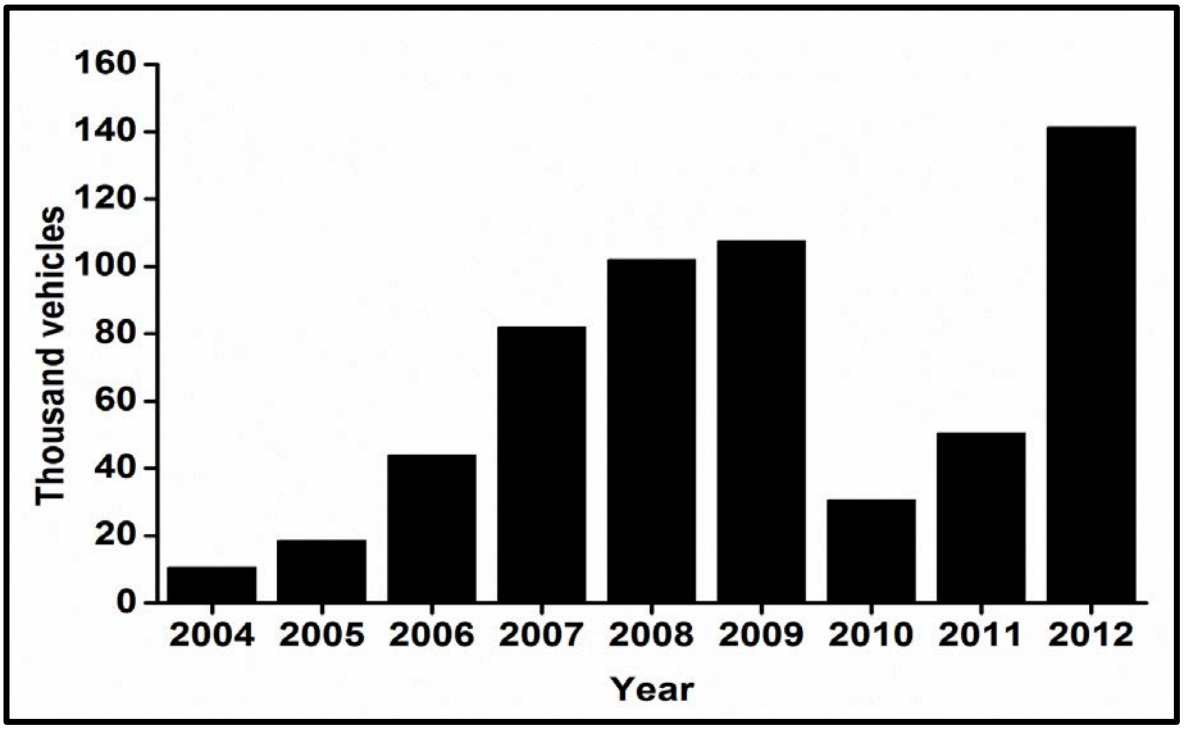

Figure 1.2: Number of Hybrid Electric vehicles (HEVs) on the road in a given year. Figures dropped in 2010 as efforts were made to ensure that only vehicles that were in Clean Cities fleets or refuelling at Clean Cities stations were counted (Source: Clean Cities annual metrics reports, 2004-2012.http://www.afdc.energy.gov/data/?q=HEV, September 4, 2013)

1.1 History of supercapacitors

Recent trends show an increased demand for efficient high energy density supercapacitors although these devices have been around for a while now. The first supercapacitor based on an electrical double layer system was developed by General Electric Corp. in 1957.[2] Limited research in this area existed at this time until 1966 when Standard Oil of Ohio Research Center (SOHIO) scientists reinvented the electrical double layer capacitor (EDLC). In their model, they used activated carbon electrodes immersed in an aqueous electrolyte on battery terminals to make a supercapacitor. They went a step further to test organic electrolytes on the same system.[3] Even until the early 1970's commercial activity on the supercapacitor was still non-existent forcing SOHIO to licence their technology to Nippon Electric Company **(**NEC) in 1978. It was at NEC where the device was first marketed as a "supercapacitor" for computer memory backup although mass production only began in the 1980's. With time, knowledge of the device grew and other companies such as Elna/Asahi Glass, and Matsushita began producing supercapacitors for watches, cameras, and portable electronics. Around this time, they produced organic electrolytes Dynacap EC for the US market. Elna/Asahi were the first company to manufacture asymmetric capacitors utilising an electrical double layer electrode and a battery electrode to produce a high energy device.

During the 1990's major advances in the production of supercapacitors were realised by the extensive research on electrode materials in a bid to increase its performance. At that time, while Panasonic were producing their "Goldcap", Maxwell Technologies had their own versions called "Boostcaps". Since then, the latter have become one of the leading manufacturers of supercapacitors in the USA where their impact is already evident both in the automotive and portable device

industry as reflected by the data in figures 1.1 and 1.2. To date, supercapacitor research continues to grow in leaps and bounds with even more companies producing their own different versions. The next section therefore highlights features of this device that make it a probable device to solve the energy storage crisis currently being experienced worldwide.

1.2 Why supercapacitors

Batteries and fuel cells are currently being developed for a wide range of applications similar to those of supercapacitors. These three electrochemical energy storage devices differ in their mechanisms of charge storage, which consequently determine their energy storage capabilities. While supercapacitors and batteries are closed systems where charge is stored on the electrode material, fuel cells are open systems which rely on the supply of fuel (hydrogen or methanol) and an oxidant (oxygen or air) to operate.[4] Different types of fuel cells exist: namely, Polymer Electrolyte Fuel Cells (PEM FC), Direct Methanol Fuel Cells (DMFC) Phosphoric Acid Fuel Cell (PAFC), Molten Carbonate Fuel Cell (MCFC), Solid Oxide Fuel Cell (SOFC) and Alkaline Fuel Cells (AFC). All these devices use different types of electrolyte which consequently influence their operating temperature, design, and field of application.[5] As long as a constant supply of fuel (hydrogen, methanol or oxygen depending on the type of fuel cell) is maintained, the life cycle of a fuel cell is much longer than that of a battery. Due to their high energy storage capability, fuel cells are more attractive than batteries and find their use in space applications. However, when compared with combustion engines and gas/steam turbines, they have an inferior power, energy performance and are still more expensive to manufacture.

Of all three devices, batteries find more applications in day to day applications with even more attractive future markets. This is due to their simple energy generation concept based on chemical reactions at the anode and cathode resulting in high energy density although the rate of energy delivery is not very striking. Currently Lithium-ion batteries (LiBs), are receiving a lot of attention in both the portable electronic markets and transportation applications due to the large amount of energy per unit weight or volume. Despite the tremendous achievements reported on the Li-ion batteries, they still face major challenges in terms of cycle life and maintaining thermodynamic stability. Their short cycle life is due to the chemical reactions that occur on the electrode/electrolyte interphase. In light of this, researchers are now focussing on optimizing the electrode material for effective Li ion intercalation and improving the power density at the same time maintaining the energy storage capacity.

While batteries rely mainly on chemical energy stored in the bulk of the electrode material which is a limiting factor for long cycle life and fast charging, supercapacitors store energy by charge separation. Because of this charging mechanism, supercapacitors possess high power and can be charged or discharged in seconds while possessing a long cycle life. Supercapacitors are distinguished mainly by the type of electrode material used in their manufacture. Even though the type of electrode material has a large bearing on the performance, the fabrication process is equally important. Two types of supercapacitors exist, namely: Electrical double layer capacitors (EDLCs) and pseudocapacitors. The former make use of the electrical double layer on the electrode surface for charge storage while the latter rely on Faradaic reactions occurring on the electrode-electrolyte interface. [6] Although these supercapacitors possess high power density, they still offer low energy density

when compared to batteries and fuel cells due to the differences in their charging mechanisms.[7] The challenge therefore is to find a single energy storage device with both high energy and power densities or alternatively to improve the energy density of ECs to match those of lithium ion batteries. Another alternative could be the coupling of both devices to produce hybrid energy storage devices to ensure longevity in power supply. The working principle together with the types of supercapacitors that exist will be discussed in detail in the following chapter. Thereafter, the experimental methods used in this work to fabricate supercapacitor electrodes will then be discussed, followed by the analysis and discussion of experimental results, and conclusions obtained for different composites.

2 LITERATURE OVERVIEW

2.1 Principle of operation

Supercapacitors store energy on the electrical double layer (Helmholtz double layer) formed at the electrode/electrolyte interface.[7] When an electrode is immersed in an electrolyte, the ions penetrate the porous electrode while charges on the electrode surface spontaneously rearrange themselves in a particular order.[4] Helmholtz is accredited with the first discovery of the double layer in 1853. However, the theoretical modeling of the electrical double layer is a result of a combination of theories by many researchers over a long period of time. According to Helmholtz, ions at the electrode/electrolyte interface are displaced and diffuse between the electrodes through the electrolyte. This results in the formation of an electrical double layer (about 5-10 Å thick) which consists of one layer on the electrode surface and the other layer in the electrolyte.[7] The nature of this double layer which consequently determines the capacitance of the electrode is governed by the composition of the electrolyte, the morphology of the electrode as well as the voltage across the two electrodes in a typical set up shown in figure 2.1.

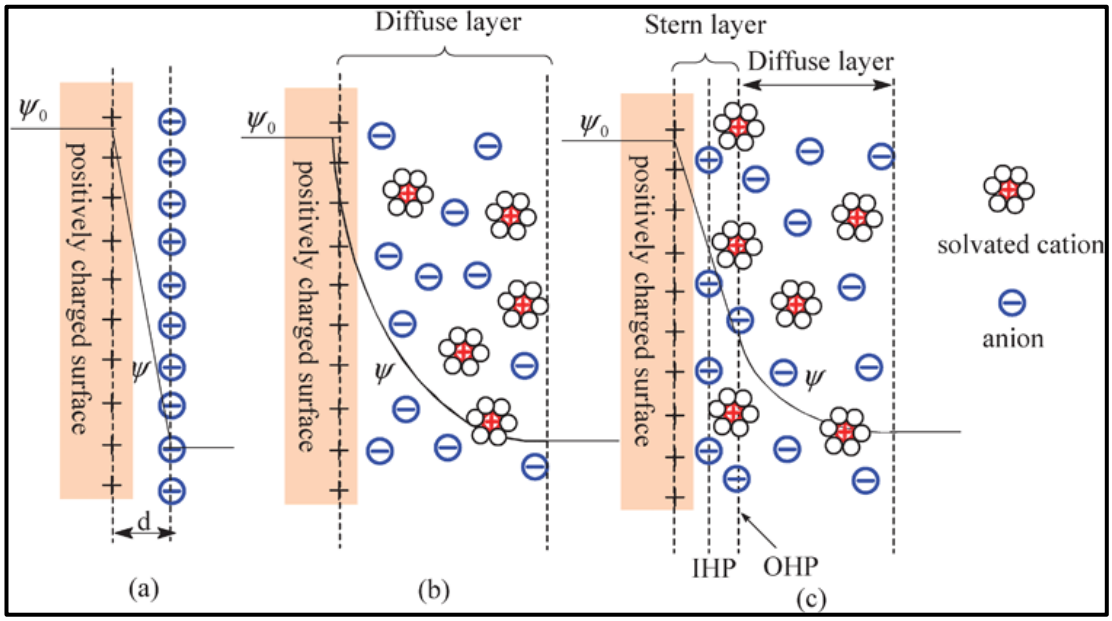

Figure 2.1: A Helmholtz model of the formation of the electrical double layer showing the location of the Inner Helmholtz plane (IHP) and Outer Helmholtz plane (OHP) next to a positively charged electrode.[8]

A closer look at this model reveals an inner Helmholtz plane (IHP) which is located closest to the electrode surface where specifically adsorbed anions are arranged. Adjacent to the IHP is the outer Helmholtz plane (OHP) which refers to the closest distance of approach by cations that exist as solvated ions and are therefore larger than the anions. [9] The Helmholtz model was further developed in 1910 by Gouy to account for the voltage dependence of the capacitance. In his model, Gouy introduced random thermal motion, which led him to consider a space distribution of the ionic charge in the electrolyte. This is known today as diffused layer. In 1913, Chapman mathematically modelled the diffused layer to explain the distribution of ions in the electrolyte. Gouy had assumed earlier that the ions were point charges. However this same assumption led to the failure of the Gouy -Chapman model as it resulted in an overestimation of the overall capacitance of the electrodes due to an incorrect potential profile.

In 1924, Stern improved the Gouy - Chapman theory, first by introducing dimensions of ions and solvent molecules. Secondly, he described the overall double layer capacitance C_{dl} with respect to a compact double layer with a capacitance C_H. This also constituted of adsorbed ions at the electrode surface, and the diffused layer having a capacitance C_{diff} as defined by Gouy and Chapman.[3]

$$\frac{1}{C_{dl}} = \frac{1}{C_H} + \frac{1}{C_{diff}} \qquad (1)$$

Although Stern's model was good in terms of explaining general interpretations of electrode –interface, perhaps the most detailed work on the double layer was done by Grahame in 1940.[10] This model was based on work performed on the mercury electrode in aqueous electrolyte to distinguish three regions namely: the Inner Helmholtz Plane, the outer Helmholtz Plane and the diffuse ion distribution region furthest from the electrode surface. This specific arrangement, due to the different sizes of cations and anions and also the polarization of the electrode surface is essential in understanding properties of supercapacitors.

A practical supercapacitor is made up of two electrodes, with one being oppositely charged with respect to the other as shown in figure 2.2. The properties of a supercapacitor are therefore heavily dependent on the type of electrode material used. Ideally, porous materials that possess a high surface area are used in the assembly in order to store more charge while a highly conductive and stable electrolyte is also preferred.

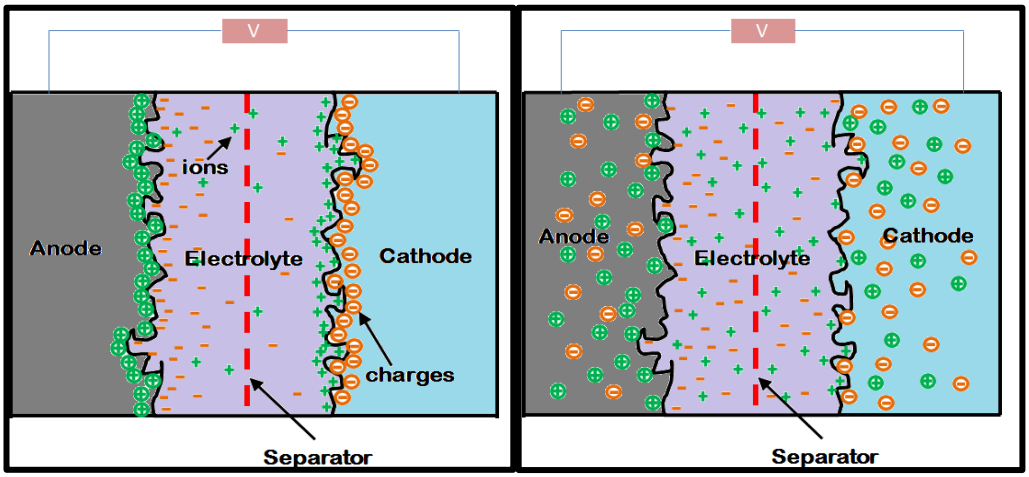

Figure 2.2: Schematic representation of a porous carbon electrical double layer capacitor in a charged (left) and discharged state (right).[11]

In some cases, supercapacitors can be arranged in series in order to boost the voltage consequently reducing the internal resistance of the device as shown in equation 2.[3, 4]

$$\frac{1}{C} = \frac{1}{C_A} + \frac{1}{C_B} \qquad (2)$$

If the capacitances of the two devices are the same, then equation 3 holds where

$$\frac{1}{C} = \frac{1}{C_A} + \frac{1}{C_A} = \frac{1}{2} C_A \qquad (3)$$

The voltage of a supercapacitor is mainly determined by the nature of the electrolyte used. Aqueous electrolytes are well known to give higher capacitance compared to organic electrolytes due to their conductive nature. However, they have a low operating voltage which consequently affects the amount of energy stored as given by:

$$\mathrm{E} = \frac{1}{2} C V^2 \qquad (4)$$

To circumvent the limitations presented by aqueous electrolytes which decompose above an operating voltage of 1.2 V, organic electrolytes with a maximum operating voltage of 3.5 V are used.[12] By increasing the operating voltage of the electrolyte, the amount of stored energy consequently increases by an order of magnitude.[13]

Nevertheless, organic electrolytes (The most common organic electrolytes being acetonitrile and propylene carbonate.[14]) possess low electrical double layer capacitance as well as poor conductivity.

Even higher operating voltages of around 4.5V can be achieved by using ionic liquids which possess high thermal and chemical stability coupled with low flammability and low vapor pressure. These properties make ionic liquids ideal for supercapacitor fabrication. However, their use is limited by their dear price and difficulty in handling. In order to fabricate a robust device, there is therefore always a tradeoff between achieving high energy density and obtaining a high overall specific capacitance which translates into high power density. These two parameters are of vital importance when it comes to describing the performance of a supercapacitor.

2.2 Relevance of Supercapacitors in Energy Storage

The Energy density (expressed in Wh/kg) and Power Density (expressed in W/kg) of an energy storage device are essential parameters in comparing its energy contents and rate capabilities. These two terms are defined as the amount of energy and power stored per unit mass or volume respectively. The theoretical maximum energy and power densities of a supercapacitor can be expressed as follows:

$$E = \frac{1}{2}\frac{CV^2}{m} \quad (5)$$

$$P = \frac{V^2}{4Rm} \quad (6)$$

In equations 5 and 6, C represents the capacitance, while m is the mass of the electrode and V is the operating voltage of the device. R is the equivalent series resistance (ESR) from the cell.

A Ragone plot makes use of both quantities to map out the performance of different energy storage devices. It is therefore a log-plot of a device's energy density versus its power density.[15, 16] These plots have been well documented as a comparison tool for different battery technologies and can also be used to select an optimum working point (i.e., discharge rate) or the optimum size of an energy storage device (ESD) for a specific application.[17] It is worthwhile to note that the energy and power densities presented are for packaged devices, rather than an electrode or a half cell (electrode, solvent, and electrolyte).[15]

Figure 2.3 shows a typical Ragone plot showing the performance of different energy storage devices. Situated in the top left corner are conventional capacitors which typically possess high power density and lower energy density when compared with batteries and fuel cells. In the bottom right corner are fuel cells and batteries that possess high energy density but low power density. This implies that batteries and fuel cells can store more energy than a capacitor but the delivery time of this energy is longer. On the other hand, a capacitor, stores less energy but has the ability to quickly discharge and rapidly release large amounts of power resulting in a high power density. This is due to the interfacial nature of its charge storage mechanism while batteries rely on the use of deep lying pores and chemical reactions situated within the electrode.

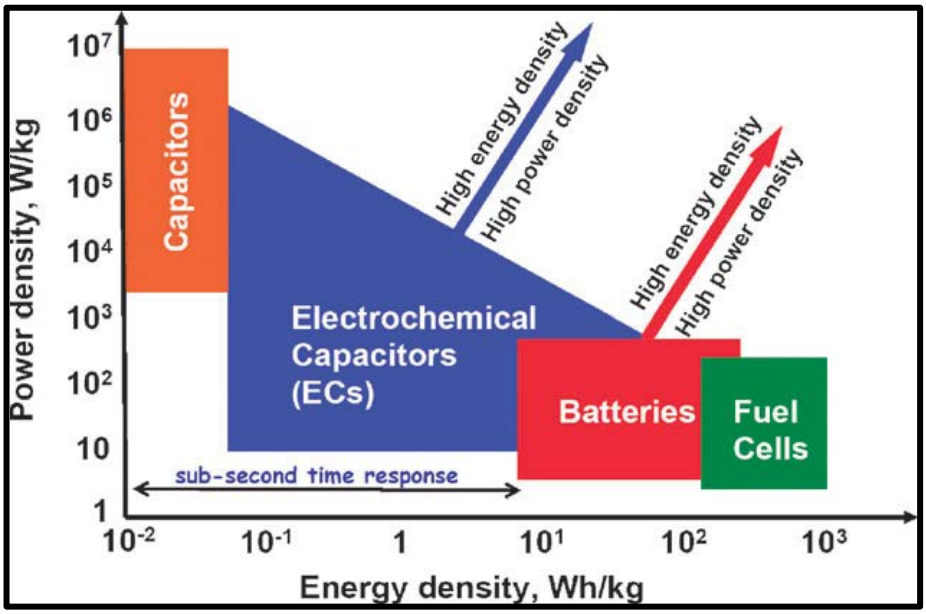

Figure 2.3: A simplified Ragone plot of specific power versus specific energy for various energy storage devices.[7, 18]

Supercapacitors, located in the middle of the Ragone plot serve as intermediate systems that bridge the power/energy gap between traditional capacitors (high power) and batteries (high energy).[7] From the Ragone plot, it is evident that the ideal electrochemical energy storage device's performance should be as close to that of the internal combustion engine as possible. Most research therefore is now focused on increasing the energy storage capabilities of supercapacitors with little or no penalty in the power capabilities by developing functional materials for electrode manufacture. To achieve this goal, the ideal electrode materials are required to possess the following characteristics:[19]

1. high surface area which governs specific capacitance,
2. high thermal and chemical stability that determines cycle life,
3. high conductivity,
4. high porosity, which has an influence on the power capability and
5. be inexpensive in order to reduce the overall cost of the device.

2.3 Classification of Supercapacitors

The development of alternative energy storage systems is undoubtedly one of the greatest challenges facing our modern society as a result of emerging ecological concerns.[20-25] The ever-increasing environmental problems and the need for efficient energy storage devices have catapulted research in this field, mainly focused on electric double layer capacitors (EDLCs), also known as supercapacitors, which consist of carbon based materials. The ultimate performance of these devices strongly depends on the intrinsic properties of their constituent materials and their eventual architectural design.[26] As a result, many research efforts have been directed towards the combination of pseudocapacitve (metal oxide and polymer based) and carbon based materials to capture high capacitance values of the former without any cycle life penalty typically associated with their use.[27, 28]

The types of materials that make up supercapacitor electrodes have a large bearing on the performance, cost and overall stability of the device. It is against this background that carbonaceous materials emerge as the materials of choice for the fabrication of supercapacitor electrodes. They possess all the favorable characteristics listed in the previous chapter which renders them useful as a support for polymer materials and metal oxides. A high surface area (~1 to > 2000 m^2/g) and high conductivity are essential for improved charge storage on the electrode /electrolyte interphase.

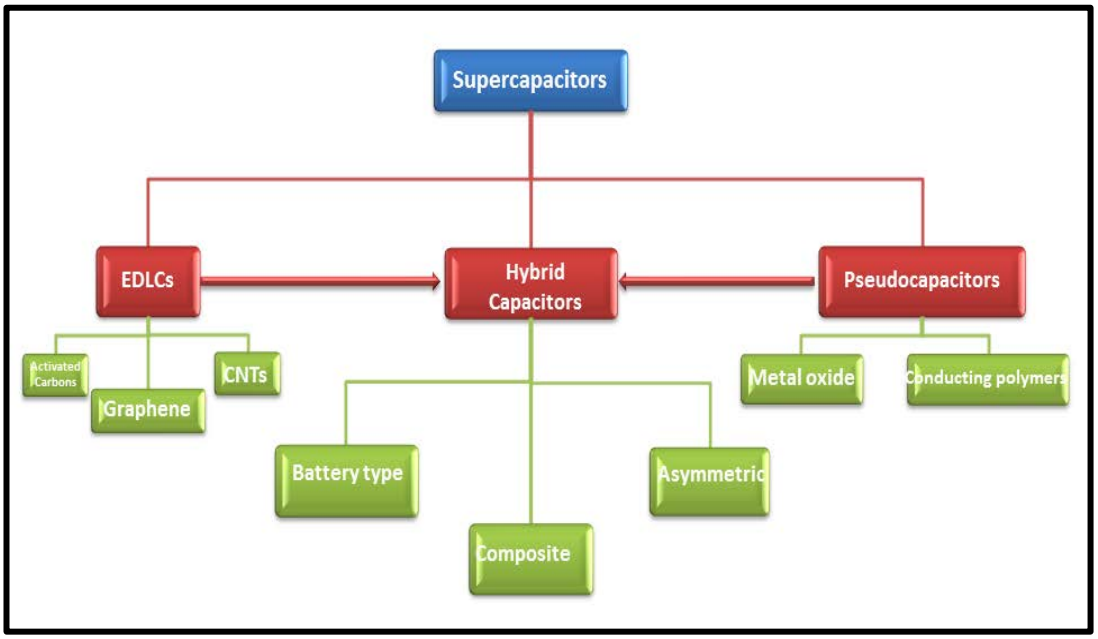

Figure 2.4: Classification of supercapacitors

Among the carbon-based materials, carbon nanotubes (CNTs) and graphene based structures, which store charges based on non-Faradaic processes relying on their conducting nature and high specific surface area, have been extensively investigated.[29-33] By manipulating their structure and dimensions of, their remarkable properties can be exploited for hydrogen storage, fuel cells, batteries and supercapacitors applications. Expectedly, a wide variety of carbons have been investigated for possible applications in supercapacitor technology. However, in this work, we will only focus on carbon nanotubes and graphene.

2.3.1 Electric Double Layer Capacitors (EDLCs) and materials

High surface area carbons include activated carbons, carbon aerogels, CNTs, graphene and carbon nanofibres. Out of these, activated carbons are the most widely used material for commercial supercapacitor electrodes due to their low cost, high conductivity and porous nature. Of particular interest, is the complex porous nature of the material that makes it very attractive for charge storage and use as an

absorbent in water treatment. Not only does the material possesses micro pores (< 20 Å wide) but also, mesopores (20-500 Å) and macropores (>500 Å). However, more focus has been recently directed towards CNTs and graphene due to their large surface area and excellent electrochemical characteristics.

2.3.1.1 Carbon nanotubes

*Structure and properties of carbon nanotube*s

Carbon nanotubes are the most commonly used building blocks in nanotechnology due to their favorable physico-chemical characteristics.[34] They exist mainly as single walled carbon nanotubes (SWCNTs) and multi walled carbon nanotubes (MWCNTs) and are widely reported in literature in energy conversion and storage devices,[35-40,41] biomedical applications,[42, 43] catalysis,[44, 45] waste water treatment [46] and separation science.[47-49] SWCNTs are essentially strips of single layer graphene sheets rolled around a central hollow core to form a tube with nanoscale diameter (~1 nm) whereas MWCNTs are made up of two or more graphene layers rolled up in a similar way. The entire structure of the CNTs is composed of sp^2 hybridized carbons which differs from the sp^3 hybridization found in diamond.

Several methods have been developed over the years for the manufacture of CNTs. To date, four methods namely: arc discharge,[50] laser ablation,[51] gas-phase catalytic growth[52] and chemical vapor deposition (CVD) have been largely reported. Of these, laser ablation and arc discharge method were the first to be used by Iijima to produce carbon nanotubes.[53, 54] However, these two methods have limitations when it comes to producing large amounts of material as both methods require additional steps for the purification of the product. The two gas phase techniques, gas

phase catalytic growth and CVD are therefore preferred as they produce larger amounts of high purity CNTs. Another extra advantage of the CVD technique is the possibility of synthesizing aligned CNT arrays. This method has been reported by Ren and co-workers where plasma-enhanced hot filament chemical vapor deposition was performed on free nickel-coated glass below 666°C.[55] It is noteworthy to mention that all the techniques for the synthesis of CNTs result in different chirality, length, diameter as well as metal impurities in the final product.[56] The presence of metal impurities however can be beneficial for supercapacitor applications where their pseudocapacitive contribution is vital.

CNTs due to their structure, exhibit various favorable properties such as high tensile strength (*i.e.*, 100 times stronger than steel), outstanding elastic Young's modulus (*i.e.*, 7 times that of steel).[57], high surface area, good electrical conductivity and exceptional chemical stability. Additionally they have an astonishing thermal conductivity that is twice that of diamonds.[56] These properties make CNTs ideal materials for a variety of applications. Although their advantages are apparent, their use in certain applications is hampered by agglomeration due to strong intertube van der Waals forces. For this reason, it is very difficult to disperse pristine CNTs in many solvents.

To overcome this problem, it is essential to functionalize them using harsh chemical treatment with HNO_3 and H_2SO_4 in order to introduce –COOH, -OH and –C=O groups thereby making CNTs wettable.[6, 13] Harsh chemical treatment serves to introduce defects on the outer walls of the nanotubes thereby exposing the surface to oxidation and increasing the specific capacitance from 70 Fg^{-1} to 120 Fg^{-1}.[6]

In some cases, SWCNTs and MWCNTs have been extensively used as catalysts in fuel cells in place of carbon black due to their favorable electrochemical characteristics. Recently, Jha and colleagues investigated the effect of chemical functionalization of SWCNTs on the electrochemical activity on a supported platinum catalyst.[58] In solar cells, CNTs are used to facilitate charge transport in the photoactive layer and to improve the photo conversion efficiency by reducing charge recombination.[59, 60] Another area that has seen an increase in CNT use is battery research and technology. The quest to improve lithium ion intercalation on the anode material has resulted in the intensive investigation of CNT nanocomposites for electrode materials. Several metal oxide/CNT composites[61-66] have been reported in literature since CNTs act as an excellent intercalation host for metal oxide nanoparticles while reducing their agglomeration.[67] Additionally, they serve as a conductive matrix that effectively reduce resistivity thereby boosting the electrochemical performance of composite electrodes.[68]

Carbon nanotubes in Supercapacitors

Apart from the different applications mentioned above, CNTs find their place in a vast majority of supercapacitor research. These materials store charge on the electrochemical double layer on the electrode/electrolyte interphase where the capacitance is directly affected by the surface area. Electrodes fabricated from the tubular nanostructure exhibit a near perfect rectangular cyclic voltammograms characteristic of EDLCs.[6] Although they possess modest surface area of ~120 $m^2 g^{-1}$ to 400$m^2 g^{-1}$ their specific capacitance ranges from 15 Fg^{-1} to 80 Fg^{-1} depending on their purity and morphology. When deposited on the electrode, the CNTs are

entangled and form a mesoporous network on the surface ideal for charge storage. These mesopores are a remarkable feature for fast release of energy resulting in high power density since electrolyte ions can diffuse into the mesoporous network unhindered thereby reducing the electrochemical series resistance (ESR).[13] Thus, the bulk of the surface area of the CNTs is effectively utilized for charge storage. To achieve such surfaces with a large proportion of mesopores, the introduction of surface groups has to be effected.[6] As mentioned earlier, pristine MWCNTs are reported to exhibit a meagre specific capacitance of up to 4 Fg^{-1} in aqueous electrolyte which can be boosted by initially functionalizing the nanotubes using different methods to achieve values as high as 135 Fg^{-1}.[69] It has also been reported that the diameter of the CNTs as well as the accessibility of their inner channel by electrolyte ions has a positive influence on the amount of charge stored by the materials.[66]

Further, the defects on the surface of the nanostructures serve as pseudocapacitive sites due to the redox reactions brought about by the oxygenated groups. The introduction of surface carboxyl groups by oxidation with an extremely aggressive oxidizing agent such as mixed acid H_2SO_4/HNO_3 can increase capacitance by up to 3.2 times.[69] However, excessive oxidation can produce an opposite effect by reducing the conductivity. It is therefore critical to achieve a compromise between increasing capacitance and reducing conductivity.

To this end, other researchers have employed plasma etching[70] and argon irradiation[71] as some of the methods for functionalizing CNTs. Lu and co-workers used a prolonged plasma etching method to cause defects on the graphitic structure of the CNTs without damaging the structure of the nanotubes.[70] A host of functional groups were added on to the CNTs increasing the pseudocapacitance of the electrode

material. Additionally, they managed to open up the ends of the CNTs significantly increasing the active surface area by making the internal surfaces accessible for charge storage. This effect was also reported by Peigney et.al. to enhance the performance of CNT electrodes.[72] Elsewhere, CNT end opening was achieved by heat treatment of SWCNTs in carbon dioxide and air. This resulted in an increase in surface area up to 1400 m^2g^{-1}.[73] The specific capacitance for electrodes fabricated from these materials was reported to have increased 1.6 times higher than as-grown CNTs.

Another way to increase the specific capacitance of these nano tubular materials is the employment of different techniques to tailor specific morphologies on the electrode surface. Different forms such as fibers,[74] mats,[75] yarns,[76] vertically aligned,[77] and sheets[78] are therefore widely reported in literature. The challenge, however is to keep the intrinsic characteristics of the individual CNTs while producing them on a macroscopic scale. The work by Futaba and co-workers is one example were a unique morphology was obtained using a simple efficient method. The group synthesized SWCNT- solid using the liquid induced collapse method on densely packed aligned CNTs.[79] As-grown SWCNT forests removed from the substrate were immersed in water and "zipped" together by introducing a liquid between the sparse SWCNTs and drying them. Upon evaporation van der Waals forces adhere the tubes together to form an ideal packing order to produce a single body. Collapses were observed with different liquids such as water, alcohols, hexane, cyclohexane etc. The resulting SWCNT-solid still exhibited high surface area (1,000 $m^2\ g^{-1}$), flexibility and electrical conductivity (showing ohmic behavior with resistance less than 1Ω). They further went on to fabricate an EDLC supercapacitor device using the two electrode set up where a specific capacitance of 20 Fg^{-1} was

obtained with tetraethyl ammonium tetrafluoroborate (Et_4NBF_4)/propylene carbonate electrolyte.

A promising approach for the enhancement of the performance of CNTs in supercapacitor electrodes has been the use of composite electrodes. In such instances, CNTs act as a conducting support of active materials such as conducting polymers[80-82] and metallic oxides [64, 65, 83]. Recently, a lot of work has been focused on carbon-carbon composites where CNTs have been mixed with graphene/graphene oxide to fabricate high performing electrodes. This will be discussed in more detail in section 2.3.4.

2.3.1.2 Graphene

The term ‘‘graphene’’ was recommended by the relevant IUPAC commission to replace the older term ‘‘graphite layers’’ that was unsuitable in the research of single carbon layer structure because a three-dimensionally (3D) stacking structure is identified as ‘‘graphite’’. The recent definition of graphene can be given as a two-dimensional monolayer of carbon atoms, which is the basic building block of graphitic materials (i.e. fullerene, nanotube, graphite). [84]

Andre Geim and Konstantin Novoselov received the Nobel Prize for Physics for their groundbreaking research on graphene: a two dimensional material found in pencil.[85] Graphene, one of the allotropes (carbon nanotube, fullerene, diamond) of elemental carbon, is a planar monolayer of carbon atoms arranged into a two-dimensional (2D) honeycomb structure. The discovery of this allotrope has quickly overshadowed carbon nanotubes and activated carbons as electrode materials of choice for supercapacitors due to its exceptional thermal conductivity, outstanding mechanical strength, anomalous quantum Hall effect and high specific surface area.

Although graphene has been studied for the past 40 years [86] a sharp rise in publications can be traced back to the past 7 years (see figure 2.4) due to the many syntheses methods that have been developed. In most of these works, in order to fully utilize the many favorable properties mentioned earlier, researchers have had to synthesize the material with great caution and avoid restacking of the individual graphene sheets. A number of methods have therefore been proposed.

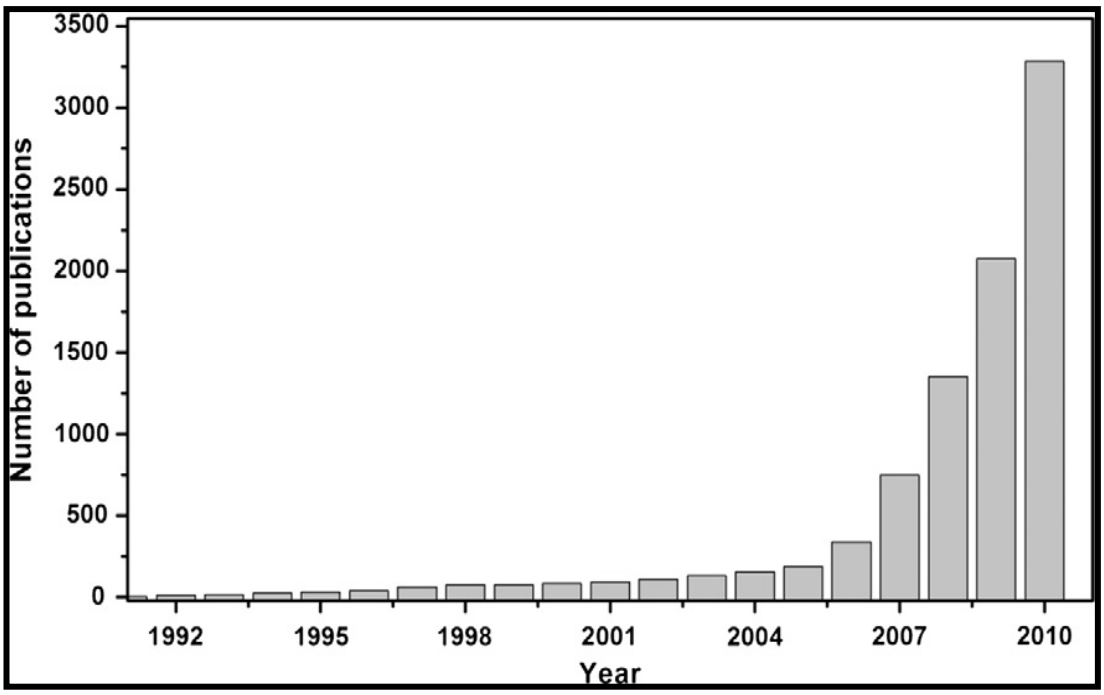

Figure 2.5: Number of publications on graphene in the past 20 years.

Synthesis of graphene

Graphene syntheses can be classified as either top down or bottom up approaches. In the former, graphene is synthesized from layered graphite. On the other hand, a bottom up approach involves the synthesis of the material from different carbon sources.[87] A host of methods reported in literature for the preparation of graphene have a large bearing on the properties and consequently its

applications. Thus, different forms of graphene ranging from graphene nano ribbons, graphene sheets (GNS), nano-platelets (which are characterized by stacks consisting of between two and ten graphene sheets) and graphene oxide (GO) exist.[88] While some methods may be ideal for selected applications (such as single layer graphenes in field-effect transistors), they do not provide the large amounts required for electrochemical applications.[89] For instance, in supercapacitor and battery research, bulk material is required while thin films are ideal for transparent electrodes in sensors.

Perhaps the most reported of these synthesis methods is the Hummer's method which will be discussed here. In their work, Hummers and Offeman oxidised graphite to graphitic oxide using a water-free mixture of concentrated sulphuric acid, sodium nitrate and potassium permanganate.[90] With this method, a considerable amount of graphene can be obtained. Also, by controlling the amount of GO, the electronic properties of the final product can be altered.[91] Another exceptional advantage of this method is that chemically modified graphene can be attained afterwards by treating the GO with hydrazine[92] or thermal treatment to obtain chemically modified graphene oxide or reduced graphene oxide(rGO) (see figure 2.6).[93] The resulting material is thus named as the GO is never fully reduced to pure graphene and contains some oxygenated groups. The starting GO material is semiconducting but due to the disruption in electronic structure, the conductivity can be improved immensely.[92] Although the conductivity of rGO is magnitudes higher than that of GO, the removal of oxygen results in low hydrophilicity which is unfavorable for many applications.[84]

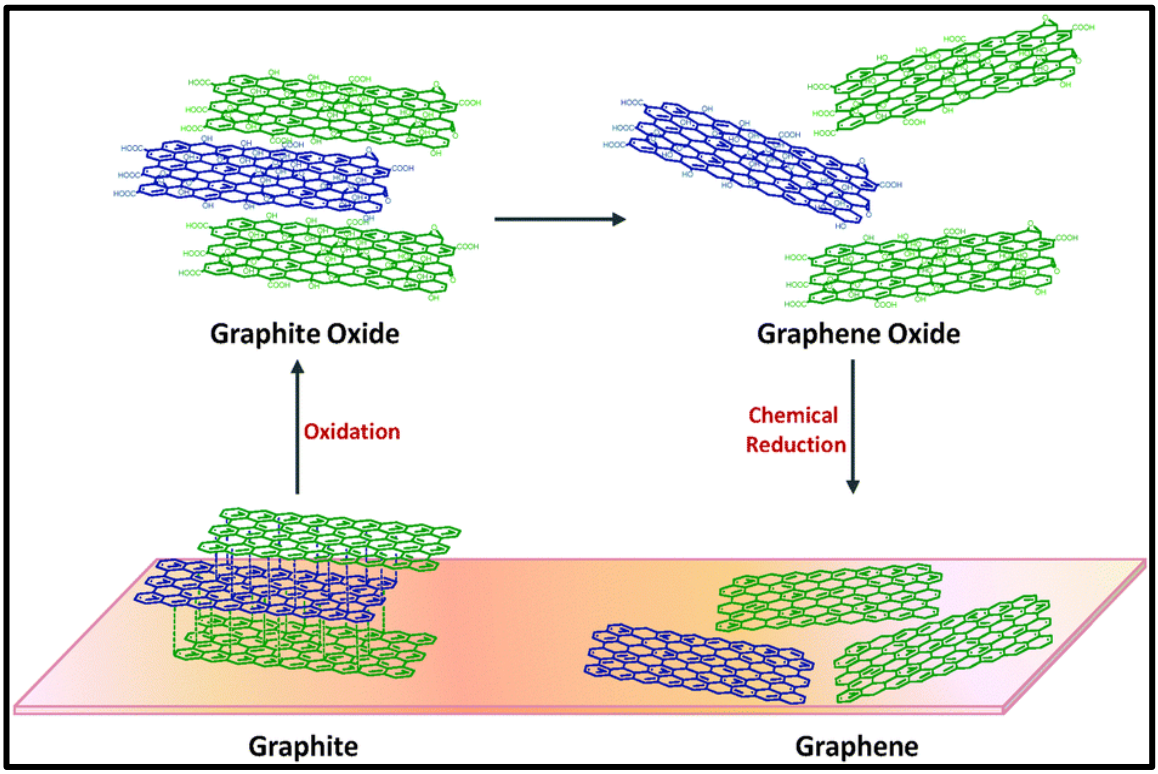

Figure 2.6: Schematic showing the synthesis of graphene from graphite.

Properties and applications of graphene in energy storage devices

It is no surprise that graphene has been termed a "wonder material" due to its exceptional physical and chemical properties hence its use in a plethora of applications in various fields. For example, in electronics, the high conductivity of graphene makes it a material of choice, where it exhibits remarkable optical transparency, chemical and mechanical stability. Since it is a single layer, foldable material with a theoretical surface area of 2630 $m^2 g^{-1}$, this makes it ideal for solar cell fabrication in place of ITO and energy storage devices. Compared to the surface area of SWCNTs and graphite (~1315m^2 g^{-1} and ~10m^2 g^{-1} respectively),[89, 94] graphene clearly stands out as an electrode material hence the immense interest. The use of graphene as an electrode material in storage devices is widely reported in fuel

cell, lithium-ion battery and supercapacitor technologies. Since large amounts of material are required for such purposes, chemical methods are more favored for the production of bulk chemically reduced graphene oxide (RGO) instead of single layers of graphene. In this work, we will only focus on its applications in energy storage devices particularly supercapacitors where an array of properties provided in table 2 play an important role.

Table 2.1: Important properties of graphene and its applications; where a tick indicates importance, a cross indicates relative unimportance and a square indicates that the property is sometimes important[87]

	Electrical conductivity	Strength	Elasticity	Surface area	Transparency	Thermal conductivity	Chemical inertness
Transistors	✓	✗	✗	✗	✗	✗	✓
Energy storage devices	✓	✗	✗	✓	✗	✗	✓
Electrodes	✓	□	□	□	□	✗	✓
Electrically conductive inks	✓	✗	✓	✗	□	✗	✓
Polymer composites	✓	✓	✓	✓	□	✓	✓
Sensors	✓	✗	□	✗	✗	✗	✓

Having considered the physical and chemical properties of graphene, perhaps the most important feature of this material is the possibility of introducing oxygenated groups on both the basal and edge planes through covalent and non-covalent functionalization. In covalent functionalization, functional groups (carboxylic acid groups, epoxy, and hydroxyl) on the basal plane act as convenient attaching sites thereby altering the functionality of the material. These play a major role in positively or negatively influencing the material's electrochemical properties in terms of heterogeneous electron transfer rate. More importantly, the surface

functionalization of graphene to produce GO and rGO opens up an assortment of possibilities in anchoring various groups on the surface, which in turn influences electrochemical behaviour. On the other hand, non-covalent functionalization exploits the presence of weak π-π, electrostatic and Van der Waals forces to attach with target molecules such as polymers[95, 96] and other conjugated π systems.[97, 98]

Graphene in Supercapacitors

The number of publications on graphene supercapacitors is a clear indication of how the material has become the material of choice in this field. The same properties that make graphene suitable for fuel cell and battery electrodes are also ideal for supercapacitors. Although graphene has received immense attention in electrochemistry, it is its versatility that opens up a numerous possibilities in fabricating supercapacitor electrodes. GO has been reported to possess a specific capacitance of 10-40 Fg^{-1} whilst rGO is more capacitive reaching as high as 205 Fg^{-1} due to the increased conductivity of the rGO.[99] In a separate work, Ruoff's group reported a chemically modified graphene produced with less functional groups from GO initially obtained from graphite. This was then modified using Hummer's method to obtain agglomerated chemically modified graphene which was then used to fabricate supercapacitor electrodes. Although the material was found to have a modest BET surface area of 705 m^2g^{-1}, it still exhibited high capacitance values of 130 and 100 Fg^{-1} in aqueous KOH and organic electrolytes respectively. These values were attributed to the large accessible surface area for electrical double layer charging.[100]

In another publication, the same group chemically modified GO with KOH activation of microwave exfoliated GO(MEGO) and thermally exfoliated GO (TEGO) to achieve higher specific surface area (up to 3100 m^2g^{-1}). The KOH activated material was reported to possess nanoscale pores generated by the KOH treatment and a remarkable specific capacitance of 200 Fg^{-1} in a two electrode set up and organic electrolyte was achieved.[29] In a bid to increase the specific capacitance even further, a new generation of nano materials and composites based on metal oxides (MO), graphene, [101]GO [27] and rGO[102] have been extensively studied. These materials, apart from being less bulky, offer an enhanced surface area and good cycling stability for supercapacitors. [103] Many authors have reported methods for engineering of GO/MO nanocomposites,[27, 104-106] such as co-precipitation and template methods [107] or hydrothermal based technology,[108] where the obtained materials generally consist of randomly mixed structures. In all these works, the authors exploit both the EDLC behaviour of graphene and the pseudocapacitive nature of metal oxides to produce robust supercapacitor electrodes. It is noteworthy to discuss the pseudocapacitor component in detail.

2.3.2 Pseudocapacitors

Conway described pseudocapacitance as arising from surface Faradaic processes.[3] In such instances, charge storage is achieved by electron transfer that causes redox activity between the electrode material and the electrolyte according to Faradaic laws. The potential, *V*, of the electrode is a continuous function of the quantity of charge, *q*, passed such that the resultant derivative *dq/dV* is defined as a measurable pseudocapacitance. In cases where chemisorption of ions takes place, a different situation arises which can be modelled by the following equation:

$$M + A \leftrightarrow M/A^{(1-\delta)} + \delta e \text{ (in M)} \qquad (7)$$

Such a reaction describes the partial charge transfer occurring on the surface of an electrode, M giving rise to a potential dependent pseudocapacitance where δe, an 'electrosorption valence' is generated.[3] Conway further went on to name three different sources of pseudocapacitance in an electrode:

i. under potential deposition, where the extent of adsorption of an ionic species onto the surface of the electrode (and involving a charge transfer to form a neutral species) is potential dependent;
ii. absorption of an ionic species from the electrolyte into the lattice of the electrode (and involving a charge transfer to form a neutral species) is potential dependent;
iii. redox processes taking place on the surface of the electrode material. [109]

In EDLCs, electrons involved in charge storage are the delocalized conduction band electrons of the metal or carbon material whilst in pseudocapacitors, these electrons originate from the orbitals of the redox material.[3] For this reason, metal oxide materials and conducting polymers have been categorized as pseudocapacitive materials. These will be discussed separately in the following sections.

Although carbonaceous materials are well known to be classical EDLCs, they also possess a certain degree of pseudocapacitance. In fact, EDLCs have been estimated by Conway to possess about 5-10 % of their total capacitance arising from pseudocapacitance.[3] On the other hand, about 2-5% of total capacitance of pseudocapacitors has been reported to arise from EDLCs. For example, functionalized CNTs are known to possess functional groups on the surface of the materials that contribute to the overall capacitance of the electrodes. The following

reactions arising from the above mentioned surface groups have been reported by Frackowiak et al.[6]

$$>C\text{-}OH \leftrightarrow >C=O + H^+ + e^- \quad (8)$$

$$>COOH \leftrightarrow >COO^- + H^+ + e^- \quad (9)$$

$$>C=O + e^- \leftrightarrow C\text{-}O^- \quad (10)$$

This phenomenon manifests itself in cyclic voltammograms obtained for pseudocapacitive materials where reversible peaks are observed instead of the characteristic EDLC "box-like" CVs. Although this behavior contributes significantly to the overall capacitance, pseudocapacitive electrodes are well known to possess poor stability due to the "fading away" of the redox processes with an increase in number of cycles.

2.3.2.1 Metal Oxide based Supercapacitors

For these metal oxides to provide maximum performance as supercapacitor electrodes, they should have certain requirements:

i. high conductivity,
ii. variable oxidation states in the chosen potential window to give rise to pseudocapacitance through faradaic reactions.
iii. the structure of the metal oxide lattice should allow for protons to intercalate freely on reduction allowing the interconversion of $O_2 \leftrightarrow OH^{-1}$ to occur.

Many attempts have therefore been made to synthesize metal oxides with variable structures through a host of techniques such as, combined sonochemical and solvothermal,[110] chemical precipitation,[111] sol–gel processes,[112] mechanical milling processes,[113] electrodeposition,[114] hydrothermal synthesis [115] and spray pyrolysis.[116] As a result, various morphologies ranging from nanowhiskers, urchin-like, nanorods,

crater-like microspheres and three-dimensional (3D) oval-shaped microparticles have been reported. [117,118,119, 120] In particular, depending on the morphology, the obtained specific surface area for metal oxides can range from 20 to 150 m^2 g^{-1}.[119] The reduction of the metal oxide particles to nanoparticle size has been widely favored as this increases the surface area of the electrode while decreasing the transport/diffusion path lengths of ions.

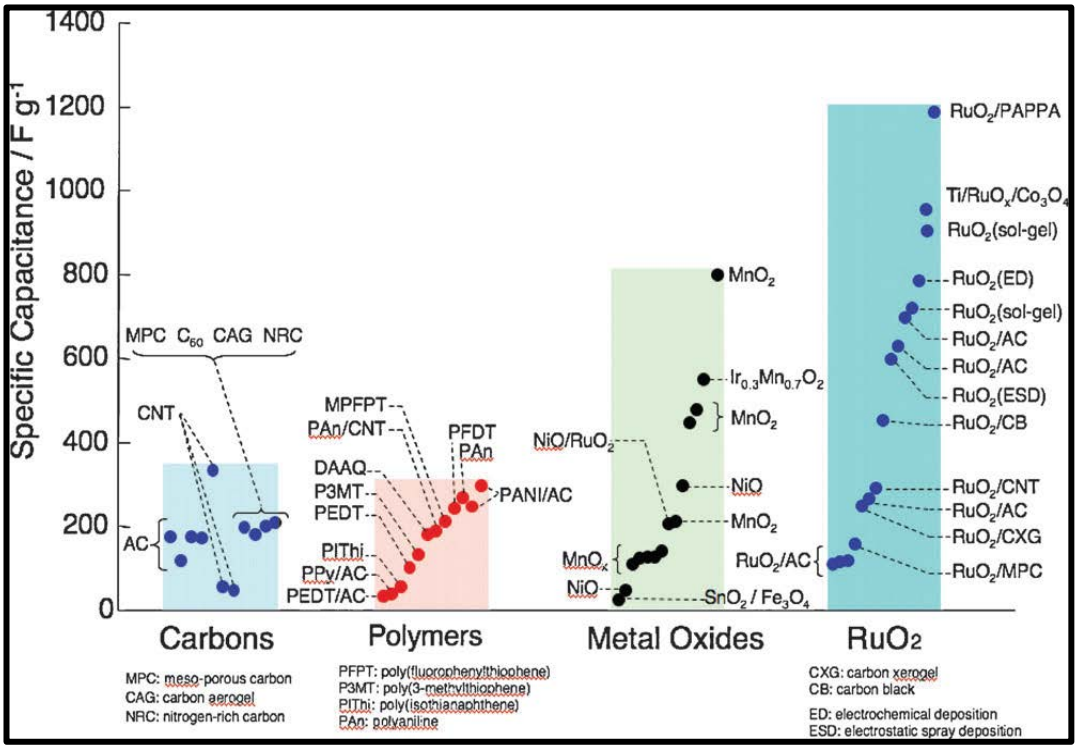

Figure 2.7: Comparison of the pseudocapacitance values reported in the literature for various materials under study as electrochemical capacitor electrodes. PFDT: poly[3-(4-difluorophenylthiophene)]; MPFPT: poly[3-(3,4-difluorophenylthiophene)]; DAAQ: diaminoanthraquinone; PEDT:3,4-poly(ethylenedioxythiophene); PPy: polypyrrole; AC: activated carbon; PAPPA: poly[3-(4-aminophenyl)propionic acid]; CB: carbon black; CNT: carbon nanotube. (Ref. 117; copyright 2008, Electrochemical Society.)[121]

One of the most broadly studied metal oxides for use in supercapacitors hydrous ruthenium oxide (RuO_xH_y or RuO_2-xH_2O) with a specific capacitance as high as 720 F g^{-1} stands out as the best performer.[122-124] This is due to a wide range of

advantageous characteristics it possesses such as, high operating potential window, variable oxidation states, highly reversible redox reactions, high proton conductivity, good thermal stability, long cycle life, metallic-type conductivity and high rate capability. However, due to its high cost and environmental concerns, other metal oxides like manganese oxide, nickel oxide,[125] cobalt oxide,[119] zinc oxide[126] and various other metal oxides[127, 128] have been preferred.

Co_3O_4 is known to be one of the most popular candidates for supercapacitor electrodes due to its good conductivity, large surface area, good corrosion stability, excellent reversible redox behavior and high theoretical capacitance (up to 3560 F g^{-1}).[129-132] This redox phenomenon originates from the reaction in equation:

$$Co_3O_4 + H_2O + OH^- \leftrightarrow 3CoOOH + e^- \quad (11)$$

In their work, Gao and co-workers synthesized a Co_3O_4 nanowire array on nickel foam using a template free method. They reported a maximum specific capacitance of 746 F g^{-1} at a current density of 5 mA cm^{-2}.[129] Contrary to this, using a template method, Wang et al. synthesized mesoporous Co_3O_4 microspheres with crater-like morphology which showed significantly lower specific surface area and capacitance of 60 m^2 g^{-1} and 102 Fg^{-1} respectively.[120] In another lab, a cobalt oxide aerogel was prepared from a Co-$(NO_3)_2 6H_2O$ precursor through an epoxide addition procedure, followed by supercritical carbon dioxide drying. The resulting material exhibited a specific capacitance >600 Fg^{-1} at a mass loading of 1 mg cm^{-2}, excellent reversibility and stability.[133] Other groups have also reported cobalt oxide films, and nanowire arrays as supercapacitor electrodes. [129,134] From these examples it is apparent that a variety of morphologies from Co_3O_4 can be obtained which directly affect the specific capacitance. Most of the recent work on this material has therefore been focused on producing such composites with high stability and even higher

specific capacitance notably with graphene.[132]

Another metal oxide that has been widely studied as a replacement for the expensive ruthenium oxide is manganese oxide (MnO_x). This is due to its natural abundance, low toxicity, environmental safety and high theoretical capacity of about 1300 Fg^{-1}.[135, 136] The pseudocapacitance of MnO_x emanates from the variable oxidation states of the manganese metal as the transitions between Mn(III)/Mn(II), Mn(IV)/Mn(III), and Mn(VI)/Mn(IV) within the electrode potential window of the electrolyte occur. The oxidation state of the manganese is therefore a very critical factor affecting the electrochemical performance of manganese oxides. A typical example of the effect of such transitions in oxidation state was clearly observed in the transformation of γ- MnO_2 to α- Mn_2O_3 and Mn_3O_4 by mechanical grinding. This was found to cause a linear decrease in the specific capacitance as the amount of γ-MnO_2 decreased.[113] Most reports on manganese oxides have therefore focussed on MnO_2 as an electrode material with amount of research on Mn_2O_3 and Mn_3O_4 for supercapacitor being adversely affected due to their poor electrochemical activity.

Like CO_3O_4, several morphologies resulting from the wide arrange of synthesis methods have been reported in literature. Perhaps, the most intriguing feature of MnO_x is its ability to form several morphologies such as nanowires,[137, 138] nanorods,[139] nanobelts,[140] flower-like microspheres,[141] and urchin-like nanowhiskers.[142] Depending on the morphology, the obtained material's specific surface area and electrochemical performance are considerably affected. Of these morphologies, one dimensional nanostructures of MnO_x have been reported to have the shortest diffusion path that automatically translates to large specific surface area, fast reaction kinetics and high specific capacitance.[14] Although MnO_x have a multitude of favorable characteristics, their major drawbacks are low specific surface

area and poor conductivity. To improve these, recent studies have been focused on MnO_x- graphene composites as recently reported by Wang and co-workers. [143] They presented a solution based approach to synthesize Mn_3O_4-graphene nanocomposites with a maximum capacitance of 236.7 Fg^{-1} in 2M NaOH.

Out of all the metal oxides discussed above, NiO seems to be the easiest to synthesize. Furthermore, NiO has an extremely high theoretical specific capacitance (ca. 3750 F g^{-1})[14] and a well-defined redox activity.[144] These qualities render the material suitable for supercapacitor studies as a substitute for other metal oxides. However, the performance of this material still falls short of the high theoretical specific capacitance due to the difficulty in controlling the porosity and particle size. This metal oxide is ideal for aqueous electrolytes where its pseudocapacitive behavior originates from the following reaction:

$$NiO + OH^- \leftrightarrow NiOOH^- + e^- \quad (12)$$

In determining the electrochemical behavior of NiO in alkaline solution, the electrolyte limits the potential window to ca. 0.5 V as it starts to degenerate.

Different methods of preparation have been shown to affect the performance of NiO supercapacitor electrodes due to the different morphologies. A typical example is the difference in performance reported for self-assembled NiO spherical nano/microstructures by Zhang and co-workers and porous NiO obtained via the sol-gel method.[145] While the porous spherical nanostructures were easy to synthesize, their performance was adversely affected by the irregularity in morphology. In a separate experiment, the sol-gel method produced a porous morphology with a specific capacitance of 696 F g^{-1} after annealing at 250 ˚C. However, the method used in this work was deemed tedious and difficult to control by Prasad and Miura. In a bid to make their synthesis of NiO simpler while preserving the high specific

capacitance, they employed electrochemical deposition to fabricate NiO nanowhiskers with high power capability and stability.[117]

Other key issues that adversely affect the use of NiO are the low conductivity and poor cycle performance. To overcome this problem, mixed oxides have been investigated.[136] This option exploits the strengths of the individual components to produce high performing composites. Prasad and Miura this time produced mixed oxide based on MnO_2 using the potentiodynamic method at a scan rate of 200 mV s^{-1}. Nickel–manganese oxide (NMO) and cobalt–manganese oxide (CMO) were deposited on stainless steel by potentiodynamic deposition. This technique allowed them to control the morphology of the resulting composite which exhibited good porosity and high specific capacity (Maximum values of 621 and 498 F g^{-1} were obtained at a CV scan rate of 10 mV s^{-1} with NMO and CMO respectively).

Perhaps the most popular approach to overcome the poor conductivity of NiO is the synthesis of composites with CNTs or graphene which act as conductive supports for the metal oxide.[62] Lin and co-workers reported a remarkable 1329 F g^{-1} for hydrothermally produced NiO/CNT composites with improved conductivity.[65] A significant increase from the lower values mentioned earlier for NiO alone. The CNT network due to its large surface area and additional redox active capacitance increases the electrochemical performance of the composite. In a more recent development, NiO nanoparticles were deposited on graphene nanosheets and used to fabricate a practical supercapacitor device. In the reported sandwich structures, NiO nanoparticles act as spacers while the GNS prevent the agglomeration of NiO nanoparticles during charging and discharging.[146] Within the same framework, the fabrication of controllable porous NiO nanostructures proves to be the most challenging aspect in this area. This will be discussed more in the following section.

2.3.3 Hybrid supercapacitors

In most articles being published nowadays, there seems to be a disagreement on the meaning of the terms “hybrid” and “composite”. In an attempt to clear out any misunderstandings between the meaning of the two terms, Thrower defines a composite material as one with a matrix and filler, and is conventionally designated filler/matrix. He goes on to describe how a filler improves the property of the matrix. This is different from a hybrid material where the constituent materials exhibit some kind of synergy by exploiting their individual favourable characteristics.[147]

Following these definitions, hybrid supercapacitors exploit the advantages of both pseudocapacitors and electrical double layer capacitors resulting in better performing supercapacitors that outperform both EDLCs and pseudocapacitors. This means that a battery-type electrode is used in the same set up with an EDLC electrode. While the carbon material provides a conductive backbone with high surface area and favorable pore distribution, the pseudocapacitive material enhances the capacitance through faradaic reactions on the surface of the electrode.[148] Research in hybrid capacitors promises to overtake research in EDLCs and pseudocapacitors.

2.3.3.1 Composite material supercapacitors

A host of composite materials have been reported in literature with the aim of developing supercapacitors with high power density, energy density, long cycle life and good rate capability. The idea behind this development is to mitigate the shortcomings of the highly pseudocapacitive metal oxides by introducing carbon nanostructures with excellent stability and conductivity.[19] Of the most capacitive carbonaceous materials, CNTs and graphene seem to be at the forefront of this

research where they provide a conductive support for metal oxide nanoparticles. Their low dimensional structure shortens ion-diffusion length enabling effective electron transport.[19] This is further improved by reducing the metal oxide particle size to nano-scale where they can be uniformly deposited on the carbon material reducing agglomeration. There are therefore four different approaches that have been well documented to achieve this, namely:

1. physical mixing of carbon nanostructures and pseudocapacitive materials,[30, 149]
2. coating CNTs or other conductive wires with active oxide layers,
3. intertwining growth of nanowires within CNT networks, and
4. self-assembly of graphene layers by stacking oxide particles that act as spacers to form sandwich structures.

To date, a wide variety of composites exist in literature and these will be discussed separately in this section.

2.3.3.2 CNT/Metal oxide composites

One of the most attractive features of CNT electrodes is their mesoporous nature. As CNTs entangle themselves on the electrode surface, they form mesopores which are ideal for charge storage. It is a well-known fact that CNTs exhibit remarkable specific surface area and conductivity that makes them attractive candidates for supercapacitor electrodes. However, their specific capacitance is mediocre (between 10-135 Fg^{-1}). Metal oxides on the other hand, exhibit high specific capacitance as discussed earlier, although they have a low specific surface area as well as poor conductivity. By mixing the two, a synergy between the two materials is achieved that results in high performance.

In such composites, CNTs have three distinct roles: (1) a percolating network that avoids the high weight loading associated with conventional conducting additives such as carbon black; (2) free standing CNT electrodes can be fabricated, eliminating the need for metal current collectors, without compromising electrochemical performance; and (3) CNTs can provide a 3-D framework where redox active pseudo-capacitive nanomaterials can be dispersed without any agglomeration.[19]

Lee and co-workers exploited the above mentioned characteristics of CNTs by coating them with MnO_2 nanoparticles using a redox deposition to obtain thin films for supercapacitor electrodes.[63] A very high volumetric specific capacitance of 246 Fcm^{-3} was obtained although this can be argued due to the small amount of active material used for electrode fabrication. Further work on these same materials was carried out using a similar redox reaction approach by Zhang's group.[66] In contrast to Lee's work, they synthesized MnO_x/CNTs composites by reacting functionalized CNTs with $KMnO_4$ in aqueous solution to make thicker (15 mg pellets) electrodes. A closer look at the electrode material showed a 3D network that was beneficial for electron transport and ions through the pores promoting Faradaic processes which in turn improved electrode performance. Only a 9% loss in capacitance was experienced with the composite electrode after 9000 cycles. Of particular interest is the increase in charge transfer resistance with increase in MnO_2 content as is reflected by a high R_{ct} value for the 60% MnO_x/CNT. This was attributed to the smaller pore volume of the composite. The contribution of the electrically conductive CNT framework can therefore not be ignored.

Another example showing the effect of CNTs on the electrochemical performance of a metal oxide was reported by Lee.[62] Although NiO has poor

conductivity which adversely affects its specific capacity, an introduction of as little as 10% CNTs was reported to show a remarkable increase in specific capacitance from 122 Fg^{-1} to 160 Fg^{-1}. Upon increasing the amount of CNTs the specific capacitance was observed to decrease implying that the overall capacitance of the composite not only came from the electric double layer but also from the pseudocapacitive NiO. A similar trend was also observed for V_2O_5 nanowires which were interwoven with CNTs to yield a specific capacitance >300 Fg^{-1} which was ca. three times higher than that recorded for V_2O_5 nanowires alone.[150] Although a lot of work has been done on MO/CNT nanocomposites including the bendable CuO nanobelt–SWCNT,[151] and Co_3O_4/MWCNT,[152] the interest has waned since the discovery of graphene.

2.3.3.3 Graphene/Metal oxide composites

Since the discovery of graphene, most research efforts have been directed towards enhancing its interactions with metal oxide nanoparticles to improve the Faradaic processes across the electrode interface so as to achieve outstanding electrochemical performance. Most of the composites in this area focus on graphene as a conductive support where the poor conducting metal oxides can be anchored and homogeneously distributed. In some instances, the metal oxide nanoparticles act as spacers, separating graphene sheets and drastically increasing the electroactive surface area of the composite and consequently the specific capacitance.

The overall performance of these electrode materials hinges mainly on the method of preparation that result in different morphologies. Various graphene/metal oxide composites ranging from metal oxide nanoparticles, nanowires, nanoneedles and nanosheets have therefore been reported with NiO,[146] MnO_2,[27, 153, 154] Co_3O_4[155]

and TiO.[127, 156] As a result, a difference in specific capacitance was noted as is the case with MO/CNT composites mentioned earlier. The synergy between the two materials results in enhanced capacitive behavior, making these composites good candidates for supercapacitor electrodes.

A few examples from recent work by different groups will be discussed here starting with the anchoring of metal oxide nanoparticles on graphene support by Lv and co-workers.[146] Their work on NiO/GO certainly gives a clearer understanding of how metal oxide nanoparticles can be used as spacers while GO acts as a conductive support to enhance performance in a sandwich structure. Graphene nanosheets were dispersed in hexadecyltrimethyl ammonium bromide (CTAB) and ultrasonicated. This was followed by addition of $Ni(NO)_3$ and ammonia solution followed by calcination at 500 ˚C to obtain a sandwich structure. NiO nanoparticles were trapped between the GNS as evidenced by a change in d-spacing from the x-ray diffraction data. The material was then used to fabricate supercapacitor electrodes and tested in a two electrode configuration to yield specific capacitances of 150~220 F g^{-1}, which is almost ten times more than the performance of graphene nanosheets (GNS) and rGO membranes. The authors concluded that the immobilization of oxide NPs between adjacent GNSs helps construct ordered channels for ion transport and therefore GNS/NiO sandwich membranes have a much better capacitive performance. From the cyclic voltammograms obtained, the pseudocapacitive effect from the NiO could be clearly seen in the resulting non-rectangular shape. According to the authors, the most outstanding feature of these composites was the improved power density and long cycle life, which was a result of their architecture. They extended the same procedure for the anchoring of Co_3O_4 and Fe_3O_4 nanoparticles on the graphene skeleton.

Elsewhere, Co_3O_4–GNS sheet-on-sheet nanostructures were reported to exhibit good electrochemical performance as lithium ion battery electrodes.[157] The Co_3O_4 sheets reportedly act as spacers thereby separating the GNS leading to faster kinetics of lithium insertion and extraction in the composite. Elsewhere, instead of using metal oxide sheets or spherical nanoparticles, a different approach to incorporate MnO_2 nanowires was used.[27] A hetero-structure nanocomposite composed of multilayered graphene sheets decorated with needle shaped MnO_2 was reported to exhibit a specific capacitance of 197.2 Fg^{-1} which was considerably higher than that of GO and bulk MnO_2 (10.9, and 6.8 Fg^{-1} respectively).

Many authors have reported methods for engineering of GO/MO nanocomposites,[27, 158] such as co-precipitation and template methods or hydrothermal based technology where the materials obtained generally consist of randomly mixed structures.[107, 159] To address this problem, some groups have recently investigated surfactant directed self-assembly,[160] layer-by-layer deposition[161] to prepare layered materials but these methods are either time-consuming and/or difficult for bulk-materials synthesis. Moreover, there are still obstacles involved in the large-scale fabrication of these composites which renders them impractical for real applications. Therefore, the research on engineering and development of ordered particles on a large-scale is still a growing field.

Since the work by Chen's group, [157] a lot more work has been dedicated to this area of supercapacitor research. Other research groups have gone further to investigate graphene/CNT composites with the same aim of improving electrochemical performance which will be discussed in the following section.

2.3.3.4 Graphene/CNT composites

Graphene sheets are well known to irreversibly agglomerate during preparation thereby reducing the effective electrochemical surface area and consequently the charge storage capacity. A recent trend has emerged in energy storage research to overcome this problem where graphene and carbon nanotubes are used to produce composite materials with enhanced performance. While metal oxide nanowires discussed in the previous section are widely reported as spacers, they are poor conductors when compared to CNTs which can be employed to perform the same function. Additionally, the CNTs act as conductive links between graphene sheets to form a three-dimensional (3D) conductive network with excellent electron conduction and hopping in composites.[162]

Previously, we reported the dispersion of pristine MWCNTs in diluted GO dispersion in water with a mass ratio of 1:3 (CNT/GO).[26] The dispersion was sonicated for 30 minutes to obtain a homogeneously mixed CNT/GO composite. The success of achieving such dispersions hinged on the ability of the CNTs to strongly interact with aromatic domains through π–π attractions. The resulting composites after drying were mixed with carbon black and Polyvinylidene fluoride (PVDF) to fabricate supercapacitor electrodes with a specific capacitance of 251 Fg^{-1}. From this result, the existing synergy between the constituent materials was clearly shown by the difference in specific capacitance where GO and the CNTs exhibited 60 and 185 F g^{-1} respectively.

In a separate experiment, Fan and co-workers synthesized a three dimensional sandwich structure comprised of CNTs and graphene using a similar approach, only this time employing the thermal reduction technique. Furthermore, they used a mass ratio of CNT/GO of 1:10 which resulted in a specific capacitance of 385 Fg^{-1} using a

more concentrated electrolyte (6M KOH). It is interesting to note that in the two experiments and others,[32, 163] an increase in specific capacitance was observed with increase in cycle number. This has been attributed to the electrochemical reduction of GO and also a possible catalytic effect by MWCNT on the reduction of GO.[26] More work on the same composites has also been reported by other groups elsewhere[164, 165]using different synthesis routes resulting in various architectures and electrochemical performance.[159, 160] Although an increase in capacitance has been observed with such composites, their overall supercapacitance falls short compared to graphene/MO composites. It is against this background that ternary structures containing, graphene, CNTs and metal oxide nanoparticles have received a lot of attention recently with the aim of improving performance.

2.3.3.5 Graphene/CNT/Metal oxide composites

Ternary architectures comprising of graphene, CNTs and metal oxides or polymers have also been reported as supercapacitors.[83, 166, 167] These compositions have been inspired by synergistic effects observed in hybrid architectures between CNTs and graphene. The addition of a third pseudocapacitive component in metal oxides or polymers into the composite brings a new dimension to composite synthesis and enhances the performance. Although high capacitance values have been reported, these hybrid architectures have not lived up to their promise of delivering the ultimate capacitance. So far, their charge storage capacity lags far behind the hybrid architectures of reduced graphene oxide and metal oxides (as high as 687 Fg^{-1}).[28] This mainly arises from the very random and much agglomerated structure of these materials which cannot be avoided through the use of normal preparation methods such as the hydrothermal route.

Therefore, further breakthroughs in design of new ternary systems, not incremental changes, hold the key to achieve the ultimate performance. Thus, architectural engineering of these materials both at nano and macro-scales, if achieved, not only can result in unrivalled capacitance performance but also opens the door to the next generation of energy storage systems. Of the few practical strategies to make self-assembly at different length-scales (nano to macro-scale) possible, taking advantage of nematic liquid crystallinity (LC) of graphene oxide (GO) in organic and aqueous media to make self-ordered and self-assembled ternary architectures seems to be the most plausible route.[168-170]

2.3.3.6 Asymmetric supercapacitors

Fabrication of composite supercapacitor electrodes undoubtedly results in better performance. However, the control of the morphology becomes more complicated when more and more different constituent materials are added. Another way to achieve high power and energy density and overall cell voltage therefore is the assembly of asymmetric supercapacitors by coupling a pseudocapacitor and an EDLC electrode. Where aqueous electrolytes have been used, a narrow electrochemical window has been reported to severely limit the energy and power densities. However, in an asymmetric set up, the electrochemical window can be almost doubled significantly enhancing the energy density. [171] In this set up, as the name suggests, two different electrodes are used to assemble a supercapacitor device with the aim of exploiting the best characteristics of pseudocapacitors and EDLCs to achieve excellent performance. In such cases, the redox reaction takes place on one of the electrodes while the non-Faradaic charge–discharge process occurs on another electrode in a single supercapacitor.

Of the many electrode materials reported in literature, activated carbon has been employed extensively as a negative electrode for asymmetric supercapacitors and a variety of polymer and metal oxides as positive pseudocapacitive electrodes.[153, 172] This is because activated carbon has a low cost, large surface area, high conductivity and excellent electrochemical activity. In this set up however, it would be misleading to assume that both electrodes have the same contribution to the overall performance. Instead, one of the electrodes tends to overshadow the other depending on the nature of the electrode materials. By optimizing the mass ratio (*R*) between the positive and negative electrodes, the best performance for asymmetric device can be achieved.[173] For this reason, some groups have gone on to fabricate asymmetric supercapacitors using composite electrodes as anodes and cathodes.[174]

With the recent emergence of graphene in the supercapacitor field, more asymmetric devices have been fabricated, this time with graphene as a negative electrode instead of activated carbon. This is due to the versatility that graphene brings in fabricating composites with high performance. Of particular interest is the recent work by Xiao and co-workers on asymmetric supercapacitors constructed with Mn_3O_4 nanoparticles and graphene sheets.[175] Instead of completely replacing the activated electrode with graphene, they incorporated both materials in the anode and the cathode while varying the amount of Mn_3O_4 nanoparticles dispersed on the graphene. This approach allowed them to achieve an energy density of 34.6 W h kg^{-1} with the scarcely reported Mn_3O_4.

A new class of hybrid capacitors called the Lithium- ion capacitor (LiC) which utilizes a battery electrode and a supercapacitor electrode has been of major interest to researchers in this field recently. In this setup, a lithium ion secondary battery electrode is made up of lithium insertion material while the other is made up of

typical EDLC carbonaceous material such as activated carbon.[176] During charge/discharge, lithium-ion intercalation/de-intercalation occurs within the bulk of the negative graphite electrode, whereas, anion adsorption/desorption occurs on the surface of the AC positive electrode. Since the EDLC activated carbon electrode relies on a non-Faradaic charge storage mechanism, fast reaction kinetics on this end determine the power capability of the LiC. On the negative graphite battery-type electrode, lithium-ion exchange process is more dominant providing attractive energy density by the utilization of the bulk material. The challenge for these devices is to increase the efficiency of the lithium-ion intercalation/de-intercalation rate capability of graphite electrodes.[177] Hu et. al. reported the use of $Li_4Ti_5O_{12}$ as a negative electrode material and activated carbon as a positive electrode to achieve a device with high rate capability.[178] Developments on the Li-ion supercapacitor continue to grow and this has been forecasted as an ideal device for high power delivery for hybrid vehicles.

2.4 Scope of thesis

Based on the literature review in section 2.2, a variety of factors contribute to the ultimate performance of an electrode material in supercapacitors. A lot of attention has therefore been directed towards nanoscale engineering of electrode materials and fabrication methods to reduce the cost and improve performance of electrodes.

As supercapacitor research has grown over the years, metal oxides have been lauded for their high specific capacitance and energy density ascribed to their morphologies which allow for the use of the bulk material to store charge. In spite of this extensive work, their stability, conductivity and surface area have been

questionable. This is due to the fact that supercapacitor electrodes are expected to possess qualities listed in section 2.2 in order to be applicable to practical systems. On the other hand, 1D, 2D and 3D carbon nanostructures with high conductivity and large surface areas have been employed as EDLC electrode materials with high power density. However, their specific capacitance is low and this presents a drawback in their use. With the emergence of graphene, the fabrication of graphene-metal oxide composites presents an effective way to exploit the pseudocapacitive nature of metal oxides together with the stability of graphene in a single electrode.

As was discussed in section 2.3.1.2 the production of high quality graphene /graphene oxide presents a challenge in achieving the best electrochemical activity. It is against this background that we desired to investigate a fast, industry scalable and cost effective way to produce graphene oxide-metal oxide composites for the fabrication of high performance supercapacitor electrodes. In this work, we discovered that we could simultaneously produce metal oxide nanoparticles and reduce graphene oxide to obtain reduced graphene oxide with higher conductivity and specific capacitance. The morphologies of these materials and their electrochemical behavior are systematically analyzed in chapters 4 and 5. In these results, different metal oxides namely NiO, Mn_2O_3, Mn_3O_4 and Co_3O_4 were mixed with graphene oxide to form composites and investigated in both single electrode and asymmetric set ups.

Although double systems with graphene oxide and metal oxides have been shown to produce high capacitive electrodes by utilizing the individual strengths of the components, the push to achieve even better performance has not be dispelled. This is demonstrated by the amount of research mentioned in sections 2.3.3 and 2.3.4. We have not been spared in this quest to enhance the performance of

composite electrodes. Thus, we set out to improve on the double systems by incorporating a third component, MWCNTs into a GO-NiO system to obtain a ternary structure produced by spray pyrolysis. This work is discussed in detail in chapter 6. The main challenge presented by these complex multi component systems is the understanding of the interactions between the graphene based support, the MWCNTs and the metal oxide nanoparticles. An attempt to provide solutions to this problem is therefore presented in chapter 6.

Although an extensive study has been carried out in a bid to highlight new pathways to produce high performance electrodes, the chance to increase the performance of supercapacitor electrodes is still present. Concluding remarks and recommendations of future work are presented in chapter 7 of this thesis, leaving the field of supercapacitor studies wide open, with a myriad of possibilities and discoveries.

3 EXPERIMENTAL

3.1 Synthesis of materials

3.1.1 Synthesis of graphene oxide

In order to synthesize the final composites, the initial stages involved the production of graphene oxide before the dispersion of metal nitrate or MWCNTs to make mixtures that could then be sprayed to produce the desired products. A general method for the production of GO was used in all experiments although further steps were employed for the production of LC-GO. This will be explained under the relevant section.

The general procedure for the production of GO was reported in our first work on GO-MWCNT composites.[26] In this work, 1 gram of natural graphite flakes (Asbury Graphite Mills, US) was thermally expanded at 1050 °C for 15 seconds. The Final expanded graphite (EG) was then used for the production of GO. 1 gram of expanded graphite and 200 ml of sulphuric acid (H_2SO_4, 98%, Merck) were mixed and stirred in a three neck flask. Next, 5 grams of $KMnO_4$ was added to the mixture while stirring. The mixture was then stirred at 30°C for 24 hours. Next, 200 mL of de-ionized water and 50ml of H_2O_2 were poured slowly into the mixture changing the color of the suspension to light brown. Having stirred for another 30 minutes, the GO particles were then washed and centrifuged with HCl solution (9:1 vol water: HCl) three times, then centrifuged again and washed with de-ionized water until the pH of the solution was about 5 to 6. The obtained GO particles were then diluted using DI water (~1.8 mg/ml) and delaminated just by gentle shaking.

3.1.2 Synthesis of rGO-Mn_2O_3/Mn_3O_4 hybrid materials

Two rGO-Mn_2O_3/Mn_3O_4 hybrid materials with different abbreviations are reported in this work as rGOMO1 and rGOMO2. These are a result of the spray pyrolysis of the following mixtures, 1:12 and 1:7 (GO: Mn $(NO_3)_2 \cdot xH_2O$), respectively. These ratios were chosen to study the effect of GO loading in the composites. The experimental setup and procedure for the synthesis of GO are already described above. However, the preparation of the composites is outlined in the schematic diagram in figure 3.1.

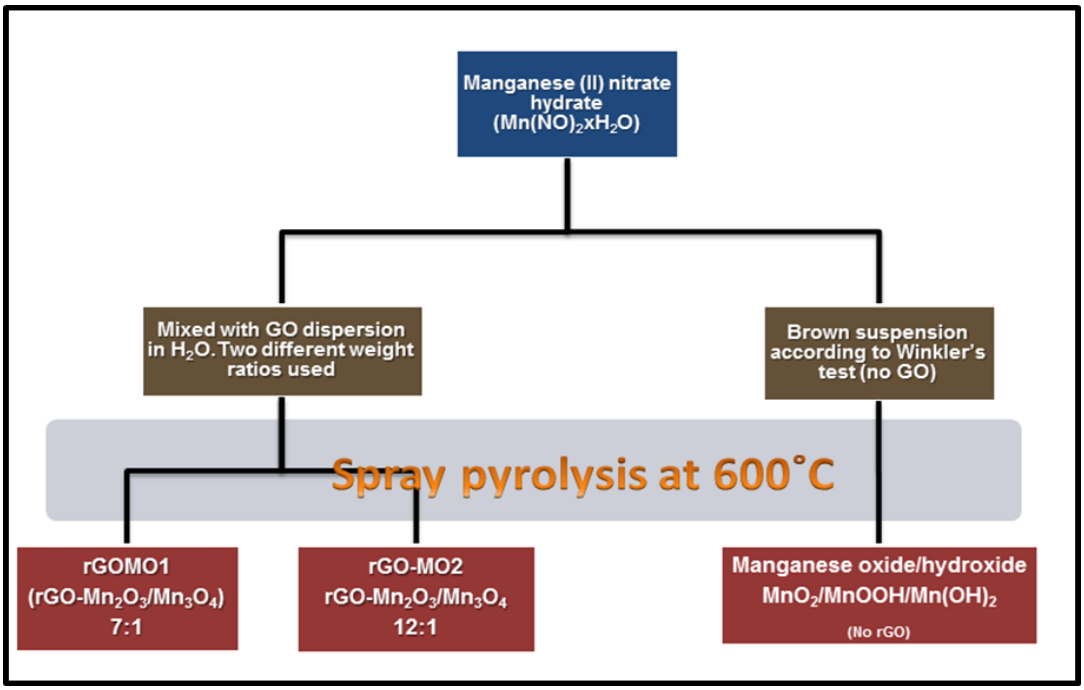

Figure 3.1: Schematic showing the experimental procedure for the formation of the Mn_2O_3/Mn_3O_4-rGO composites from manganese nitrate hydrate.[179]

To investigate the effect of adding GO to the manganese oxide we prepared the first material without any GO present. This material was prepared by adding 27.39g of manganese (II) nitrate hydrate ($Mn(NO_3)_2 \cdot xH_2O$, 98%, Sigma) powder into water resulting in a brown suspension, the same as Winkler test. [180]

$$2Mn\,(NO_3)_{2(s)} + 3/2O_{2\,(g)} + H_2O_{\,(l)} \rightarrow 2MnO\,(OH)_{\,2(s)} + 2N_2O_{5\,(g)} \qquad (13)$$

The red-brownish suspension was stirred for 30 minutes using a conventional magnetic stirrer and then sprayed at 600˚C in air into a vertical-type spray-pyrolysis reactor (Note that this material was not mixed with graphene oxide). Following this, we prepared GO containing mixtures with varying amounts of GO with weight ratios of 1:12 and 1:7 (GO:$Mn(NO_3)_2{\cdot}xH_2O$). Manganese (II) nitrate hydrate ($Mn(NO_3)_2{\cdot}xH_2O$, 98%, Sigma) was diluted in a GO dispersion in water and stirred for 30 minutes using a conventional magnetic stirrer followed by spray-pyrolysis at 600˚C into a vertical-type spray-pyrolysis reactor to obtain rGOMO1 and rGOMO2.

3.1.3 Preparation of rGO/ NiO and rGO/Co_3O_4 composites

In another experiment where rGO-NiO and rGO-Co_3O_4 composites were studied, cobalt hydroxide ($Co(OH)_2$, 95%, Aldrich) powder was dissolved in 1 M nitric acid solution. In a typical synthesis, 9.784 g cobalt hydroxide ($Co(OH)_2$, 95%, Sigma) powder was solved in 100 ml of 1M nitric acid solution. The resulting solution was added into a diluted GO dispersion in water followed by 30 minutes of stirring using a conventional magnetic stirrer. The hybrid material was then obtained *in situ* by spray pyrolyzing the suspensions into a vertical type spray pyrolysis reactor to obtain 20% rGO/Co_3O_4 composites. A typical range of reaction temperatures is about 500 °C to about 1000 °C, with about 600 °C being preferable for a fluid flow rate of between about 4 ml min^{-1} and about 20 ml min^{-1}. Additionally, when a noble carrier gas is used, a positive partial pressure for the noble carrier gas can be introduced within the reaction chamber which influences the produced graphene oxide based composite. An example positive partial pressure that

can be used is between about 3 kPa and about 10 kPa. The same procedure was performed for the preparation of the rGO-NiO composite. This time 29.079 g crystalline Nickel (II) nitrate hexahydrate (Ni(NO3)2· 6H2O, Sigma) powder was dissolved in water and then added into a diluted GO dispersion in water with different mass ratios to obtain 20 % rGO/NiO after spray pyrolysis.

3.1.4 Formation of liquid crystalline dispersions of MWCNT/rGO/NiO

In this thesis, a two-stage preparation route to fabricate self-assembled ternary architectures comprising of graphene, CNTs and metal oxides was employed. The architectural design and engineering of these ternary systems helped us create unique hierarchical assemblies with high performance. In the first step, for the first time, we tailor-made liquid crystals (LCs) of GO based ternary hybrid materials by exploiting the nematic liquid crystalline behaviour of GO and its specificity and directionality (as a result of its orientational ordering). In the second step, via a facile in-situ spray pyrolysis method (Figure 3.2) which essentially produces isotropic architectures in the form of spherical particles. The experimental set-up and procedure for the synthesis of graphene oxide (GO) liquid crystals were based on synthesis method mentioned earlier in section 3.1.1.

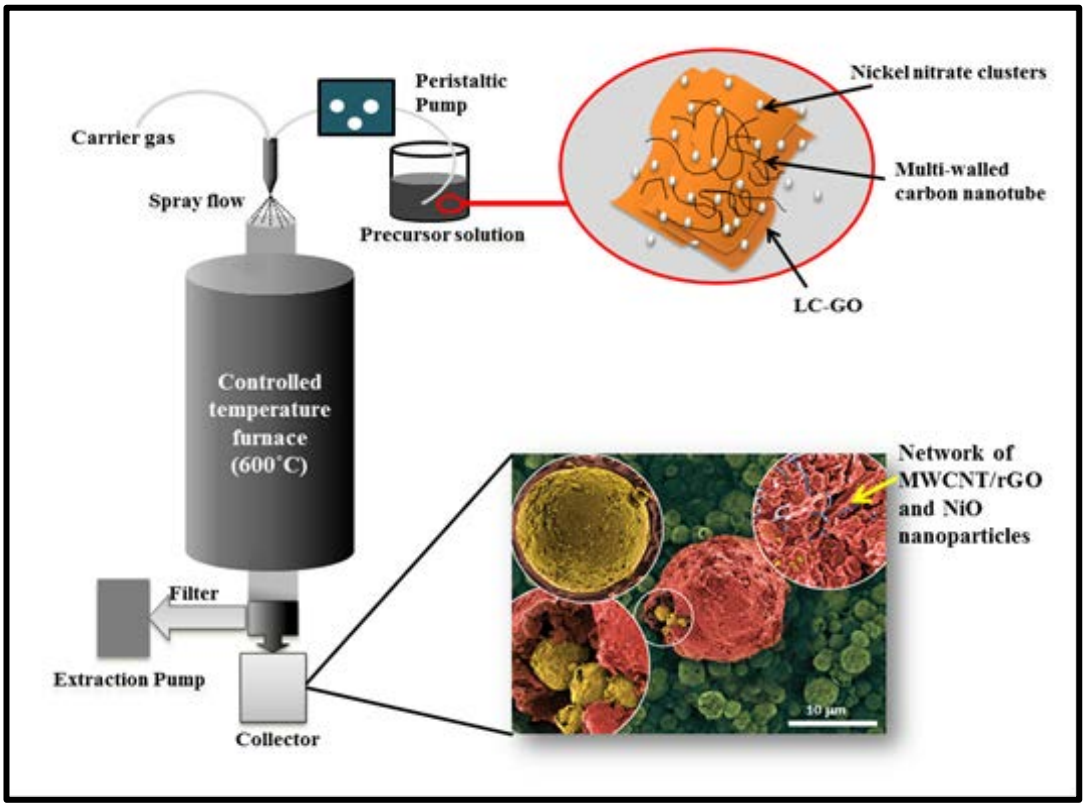

Figure 3.2: Schematic illustration of the production process of the ternary MWCNT/rGO/NiO composite through spray pyrolysis. Nickel nitrate particles mixed with carbon nanotubes and LG-GO in solution and introduced into a furnace through a nozzle via a spray flow and collected as a powder containing globular structures of MWCNT/rGO/NiO shown in the SEM image. Some smaller spheres uniformly coated by NiO nanoparticles are seen to be contained within the larger particles.[181]

For the characterization of the birefringence of this GO, the dispersion was examined by polarized optical microscopy (Leica DM EP) operated in transmission mode as reported by Jalili and co-workers.[182] We followed the same procedure where, 75 µL of a series of GO dispersion concentration (0.1 to 5.0 mg mL^{-1}) was placed in a capillary tube (1.5 mm ID), sealed (using glue) and then left stationary for one week. The volume fraction of the stable birefringent (nematic) phase was then measured by polarized optical microscopy on the seventh day. The rheological properties of aqueous GO dispersions were investigated using a rheometer (AR-G2

TA Instruments) with a conical shaped spindle (angle: 2°, diameter: 40 mm). Approximately 600 μL of GO dispersions was loaded into the rheometer with great care taken not to shear or stretch the sample. Shear stress and viscosity were measured at shear rates between 0.01 to 10 using logarithmic steps (total 200 points) for two complete (ascending and descending) cycles. Shear rate was kept constant at each point for 2 min and data recorded during the last 15 s are reported. Yield value and viscosity (at the lowest shear rate) were obtained and plotted as a function of concentration for the first and second ascending cycles

In a typical run, nickel (II) nitrate hexahydrate (Ni $(NO_3)_2$. $6H_2O$, sigma) powder was dissolved in water and then added into LC GO dispersion in water with different mass ratios to obtain a nominal dispersion of 2:7 (GO: nickel (II) nitrate hexahydrate) as reported earlier for the rGO-NiO composite. However, in this case the dispersion was then stirred for 30 min using a conventional magnetic stirrer followed by addition of MWCNTs. These functionalized carbon nanotube dispersions in water were produced based on our previous report, [28] were then added to obtain a nominal dispersion of 2:2:7 and 1:3:7 (stirring for a few hours. The hybrid material was then obtained as MWCNTs: GO:nickel (II) nitrate hexahydrate) followed by spray pyrolyzing the dispersions into a vertical type spray pyrolysis reactor.

3.2 Physico-chemical characterization

It is essential that all materials for supercapacitor fabrication be characterized in order to fully understand their electrochemical performance. It is against this background that a series of physico-chemical characterization techniques were employed to elucidate the morphology, composition and characteristics of the

materials. In these experiments, X-ray diffraction was used as the primary analysis tool for both qualitative and quantitative purposes and clarification of properties and structure of the composites.[183] The technique has the advantages of being able to use a small amount of sample for testing and being non-destructive at the same time. However, the result does not give comprehensive information regarding the morphology of the composites making it essential to use XRD in conjunction with other techniques to give a full understanding of the characteristics of the materials. In all the experiments carried out in this work, XRD was performed at room temperature using high resolution X-ray diffraction system (GBC MMA X-Ray diffraction (XRD)) with Cu-Kα radiation (X-ray wavelength λ = 1.5406 Å operating at 40 keV, cathode current of 20 mA) under normal laboratory conditions in thin film configuration.

To complement the results obtained by XRD, X-ray photoelectron spectroscopy (XPS), a surface technique that has been used mainly for analyzing thin films was employed. Recently, most of the XPS analysis has been on metal oxide nanoparticles as well as graphitic material to analyze their atomic concentrations and elemental composition. While the technique has its advantages in giving elemental composition for GO and rGO where the intensities of all oxygenated groups are expected to be reduced significantly, it falls short where metal oxide nanoparticles are involved. Nanoparticles tend to aggregate and respond to different environments making it extremely difficult to obtain useful data. The elemental composition of all the samples in this work were characterised using the X-ray photoelectron spectroscopy (XPS, PHOIBOS 100 hemispherical analyser produced by SPECS GmbH) with pass energy of 26.00 eV, 45° take-off angle and a beam size of 100 µm.

Where these surface techniques fall short, SEM makes up for by providing 3D topological information presented as images of the samples. The working principle of the electron microscope will not be discussed in detail here but only a brief outline shall be presented. The functioning of a scanning microscope is analogous to that of a key copying machine used by a key cutter. To create a copy of a key, the curves and indentations are scanned and copied onto another surface. In the same way, an electron beam is raster scanned over the sample's surface from one end to the other and according to the dents on the sample. When the electron beam hits the sample, secondary electrons are emitted in a specific fashion revealing the topology of the sample and creating an exact 3D copy which is presented on a monitor as an image. In this thesis, the morphologies of the composites were examined by field emission scanning electron microscope (FE-SEM) using the JSM 7500F, JEOL instrument.

Another technique, TEM (Transmission Electron Microscopy) was used to image the samples prepared in this work. Unlike SEM, the incident beam in the TEM is allowed to pass through the material revealing its microstructure. The technique is therefore generally used to characterize nano size materials to the atomic scale resolution where a transmitted electron beam passes through the ultra-thin sample and reaches to the imaging lenses and detector. Since, graphene is only an atom layer thick, this is probably the best technique to resolve atomic features of such a material and the arrangement of metal oxide nanoparticles on its surface.[184] For this reason, High-resolution transmission electron microscopy (HRTEM) was performed on the JEOL F3000 machine.

Apart from understanding the morphology of a material, its specific surface area is an equally important factor as this has a bearing on the specific capacitance as mentioned in section 2.1. To measure the specific area of a sample, it should be first ground into a powder. The specific surface area is determined by physical adsorption of a gas on the surface of the solid and by calculating the amount of adsorbate gas corresponding to a monomolecular layer on the surface. Physical adsorption results from relatively weak forces (van der Waals forces) between the adsorbate gas molecules and the adsorbent surface area of the test powder. The determination is usually carried out at the temperature of liquid nitrogen. The amount of gas adsorbed can be measured by a volumetric or continuous flow procedure.The specific surface area was determined by the BET method using the Nova 1000 gas sorption instrument.

3.3 Electrode Preparation and Electrochemical Characterization

3.3.1 Single Electrode Preparation

For the three electrode set up (sometimes referred to as the single electrode set up), the working electrode was prepared by coating the rGO-NiO and rGO-Co_3O_4 materials on to stainless steel sheets (1cm × 1cm) previously polished with sand paper and ultrasonicated in ethanol for an hour. These experiments were carried out in 1M NaOH at the same scan rates and current densities for the two composites for comparison purposes. The electroactive material (rGO-MO) were firstly mixed with carbon black and PVDF binder at a mass ratio of 70:20:10 in an Agate mortar with (N-methyl pyrrolidinone) NMP solvent and ground to form a slurry. This was then spread on to the polished stainless steel surface to achieve mass loadings between 1 and 2 mg and allowed to dry in a vacuum oven for 24 hours. The same procedure

was followed for the preparation of rGO-Mn_2O_3/Mn_3O_4 electrodes and the MWCNT/rGO/NiO ternary hybrid. However, different approaches, equipment and set ups were used for the asymmetric supercapacitors as will be explained in the following section.

3.3.2 **Asymmetric Set up**

To fabricate the positive electrode for the coin cell asymmetric supercapacitor, a slurry of the active material (in this case rGO-Mn_2O_3/Mn_3O_4) was prepared as described above but this time coated onto the nickel foam substrate, with an average mass loading of ~ 1.4 $mgcm^{-2}$. The same procedure was followed for the negative electrode made up of graphene. The electrodes were then dried at 80 °C for 8 hours in a vacuum oven and pressed to a thickness of ~ 0.5 mm. The electrodes were assembled in a coin cell (LIR 2032) separated by whatman© filter paper with 1M NaOH as electrolyte. The cell was then tested using Galvanostatic charge-discharge measurements and EIS on an Autolab potentiostat PGSTAT 302N (Eco Chemie, Utrecht, The Netherlands) driven by the General Purpose Electrochemical Systems data processing software (GPES and FRA software version 4.9). The same preparation procedure was used for all the other experiments.

For the study of the ternary hybrid composites, a similar approach was followed although this time an ECC-STD Electrochemical Cell (El-Cell) was used with the cell consisting of two gold current collectors (15 mm in diameter) and a glass fibre separator (see figure 3.3). The ternary active composite material, MWCNT/rGO/NiO was spread as a slurry on circular stainless steel substrate with a diameter of 15mm and dried in a vacuum oven to achieve mass loadings ~ 2 mg for each electrode. The same procedure was repeated for the activated carbon electrode.

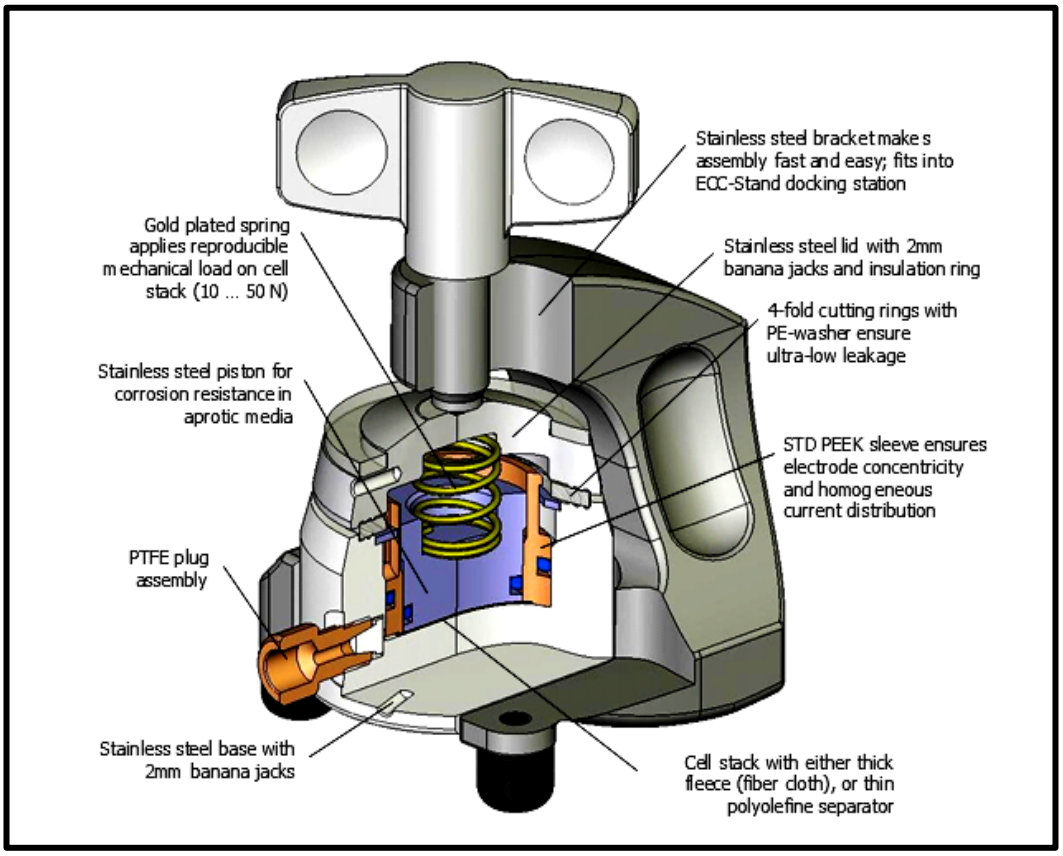

Figure 3.3: Electrochemical set up for asymmetric supercapacitor tests ((El-Cell, Hamburg Germany)

3.4 Electrochemical techniques

In supercapacitor studies, cyclic voltammetry is usually the first diagnostic tool utilised to quickly assess the behaviour and performance of electrode materials. This technique due to its simplicity and ease of measurement finds a lot of uses in biochemistry, inorganic and organic chemistry.[185] The technique involves the potential scanning of a preselected potential window while measuring the resultant current to obtain a cyclic voltammogram (CV).[3] The potential of the working electrode is controlled versus a reference electrode, in this case Ag|AgCl.

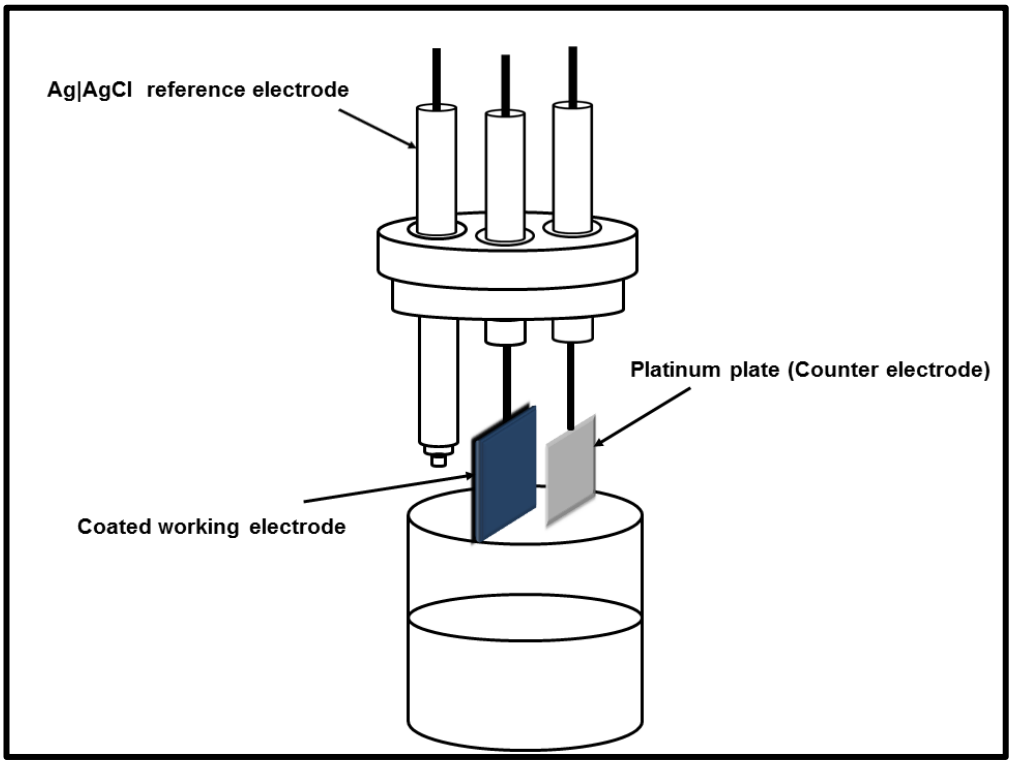

Figure 3.4: Electrochemical beaker-type cell for cyclic voltammetry.

For typical EDLC materials a nearly rectangular CV is expected due to the absence of redox activity. However, this is not usually the case as most of the EDLC materials contain oxygenated groups that contribute to the pseudocapacitance. For, typically pseudocapacitive materials such a metal oxides and conducting polymers, a deviation from the ideal rectangular CV's and the presence of reversible peaks is clearly evident as shown in figure 3.5.

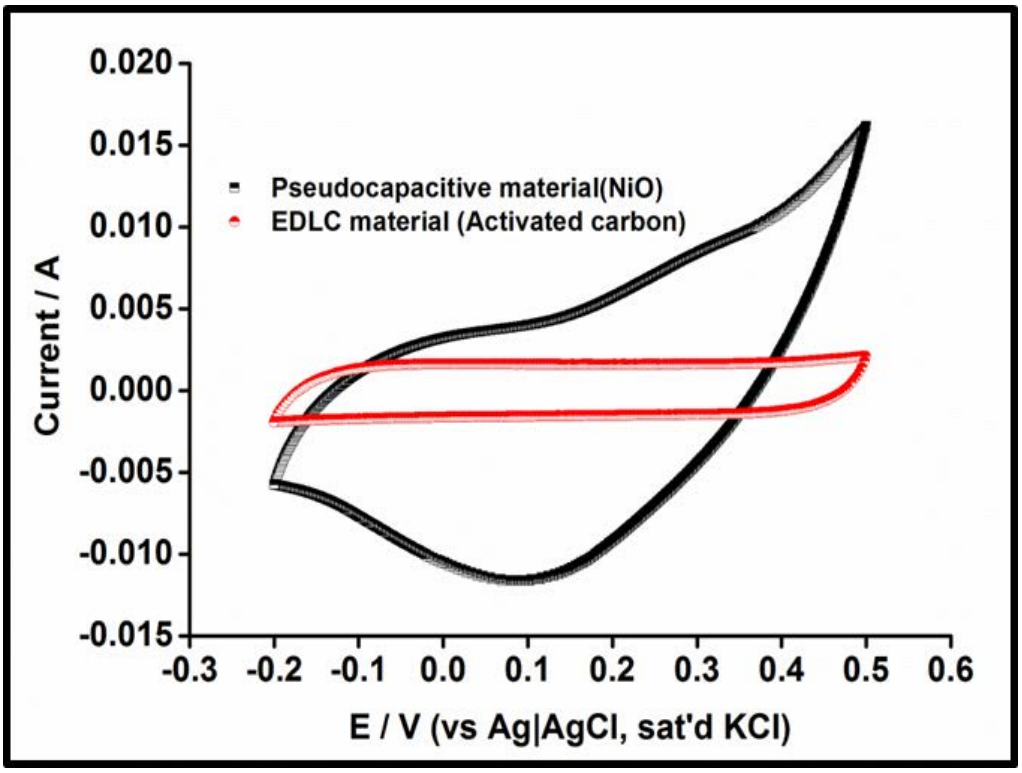

Figure 3.5: Typical cyclic voltammograms showing the difference between those obtained for carbonaceous material and highly pseudocapacitive metal oxide.[28]

Another technique similar to CV is the Constant current charge /discharge technique which gives more accurate picture of the performance of a supercapacitor device. From this experiment, power density and energy density of the device can be calculated. In this technique, charging and discharging of the device is performed at a constant current at different rates to determine a plot of E (V) vs time(s). For ideal EDLC electrodes, a typical linear charging and discharging slopes are observed while these are usually distorted for pseudocapacitive electrodes.

Out of all the electrochemical techniques used for evaluation of supercapacitor electrodes, perhaps Electrochemical impedamce spectroscopy (EIS) gives the most information regarding the morphological changes and charging mechanisms taking place on the electrode surface. A small amplitude AC current is applied to the supercapacitor device so that the AC voltage and current response of the electrodes is

measured and analysed. The data obtained is then plotted on a Nyquist plot to give information regarding the capacitance, resistance and inductive behaviour of the electrode under study. A typical Nyquist plot for a supercapacitor is comprised of an almost vertical slope at low frequencies and a small or non-existent semicircle in the high frequency region as shown in the diagram below.

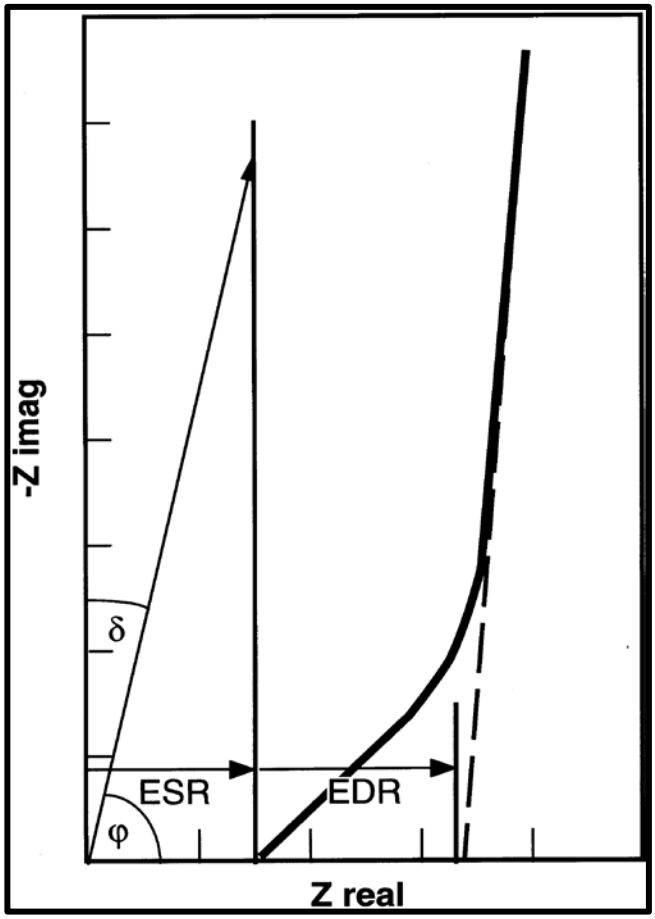

Figure 3.6: Schematic representation of the Nyquist impedance plot of an ideal capacitor (vertical thin line) and an electrochemical capacitor with porous electrodes (thick line).[7]

To fully characterize the supercapacitor materials reported in this thesis, all the characterization techniques and experimental procedures were implemented. The results obtained from these techniques are discussed in the chapters that follow.

4 SUPERCAPACITORS FROM URCHIN-LIKE REDUCED GRAPHENE OXIDE-MN_2O_3/MN_3O_4 NANOSTRUCTURES

4.1 Graphical abstract

Reduced graphene oxide-manganese oxide composite with urchin like morphologies obtained by spray pyrolysis shows outstanding electrochemical performance. In this case *in-situ* means "in the reaction mixture" meaning that the engineering/synthesis of the composites was done in one place where the final product was controlled in the reaction mixture.

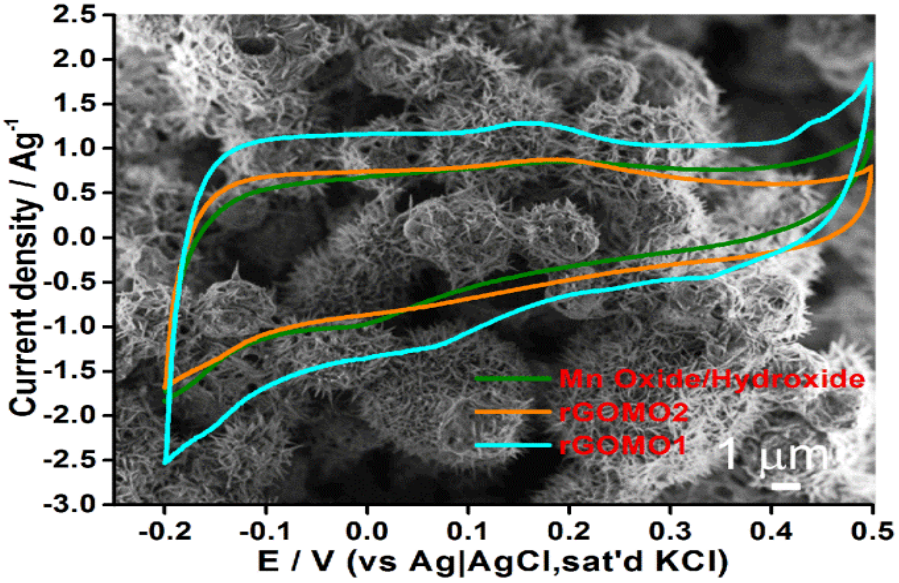

Figure 4.1: Graphical abstract showing the morphology of the electrode materials and their performance.[179]

4.2 Introduction

Due to high cost and environmental concerns, manganese oxide, which has a high theoretical capacitance of 1370 Fg^{-1}, has been preferred as an electrode material.[128] Many attempts have therefore been made to synthesize manganese oxides through a host of techniques such as combined sonochemical and solvothermal,[110] chemical precipitation,[111] sol–gel processes,[112] mechanical milling processes,[113] electrodeposition[114] and hydrothermal synthesis.[115] However, the

preparation methods are less effective in controlling the crystal structure, microstructure and chemical state of manganese oxides.[14] In all these studies, the oxidation state of manganese has been reported to critically affect the electrochemical performance of the electrodes. MnO_2 has therefore been reported more than any other oxide of manganese due to the various morphologies it can attain as well as a reduction in diffusion path in the electrode material.[14]

The amount of research on Mn_2O_3 and Mn_3O_4 for supercapacitor studies has been adversely affected due to their poor electrochemical activity. A transformation of γ- MnO_2 to α- Mn_2O_3 and Mn_3O_4 by mechanical grinding was found to cause a linear decrease in the specific capacitance as the amount of γ- MnO_2 decreased.[113] Also, a strict ratio of MnOx:rGO has not been established yet although a high amount of MnOx is desirable due to the pseudocapacitance contribution of the metal oxide even with as little as 10% rGO.[186]

In a bid to improve the performance, researchers have synthesized Mn_2O_3-carbon aerogel and Mn_3O_4-graphene[187, 188] composites although only a handful of such reports are available in literature. Recently, Wang and co-workers reported a solution based approach to synthesize Mn_3O_4-graphene nanocomposites with a maximum capacitance of 236.7 Fg^{-1} in 2M NaOH.[143] Elsewhere, a maximum capacitance of 256 Fg^{-1} was reported in 6M NaOH after the nanocomposites were synthesized by first mixing a graphene suspension in ethylene glycol with a MnO_2 organosol, followed by ultrasonication processing and heat treatment of the mixture.[189] Lee and co-workers also reported Mn_3O_4 nanorods mixed with graphene with a maximum capacitance of 121 Fg^{-1}.[190] All these studies however, were carried out in the three electrode set up without testing the practicality of device fabrication.

Depending on the method of preparation and conditions, a variety of nanostructures has also been reported. We are aware of the many reports on MnOx urchin-like structures in literature. These have been shown to possess high surface area and good electrochemical activity although their preparation time takes a considerably long time when compared to the spray pyrolysis method.[118, 191]

In this work we use the in-situ spray pyrolysis method to produce for the first time, hybrid 3D urchin-like architectures of Mn_2O_3 and Mn_3O_4 anchored on a highly conductive reduced graphene oxide support with improved electrochemical performance. A total specific capacitance of 425 Fg^{-1} and 133 Fg^{-1} in three-electrode and two-electrode asymmetric set ups were recorded in 1M NaOH as an electrolyte respectively. In spite of the very limited time of heat treatment, the spray pyrolysis method proved to be effective in the reduction of graphene oxide(GO) to reduced graphene oxide (rGO), which offers a simple yet effective approach to design advanced graphene based hybrid materials with extraordinary capacitance. Due to the presence of rGO, high capacitance retention of 83% was observed over 1000 cycles.
The spray pyrolysis technique: while providing perfect homogeneity of the final products and productivity with industry up-scaling capabilities offers great flexibility regarding the type and use of initial solutions and/or suspensions. By controlling the fabrication process, it is possible to manufacture a wide range of materials with numerous shapes and structures. We therefore suggest that this method can be further exploited to fabricate a wide range of graphene-metal oxide/hydroxide materials for different applications in energy storage devices.

4.3 Results and Discussion

4.3.1 Structural characterization

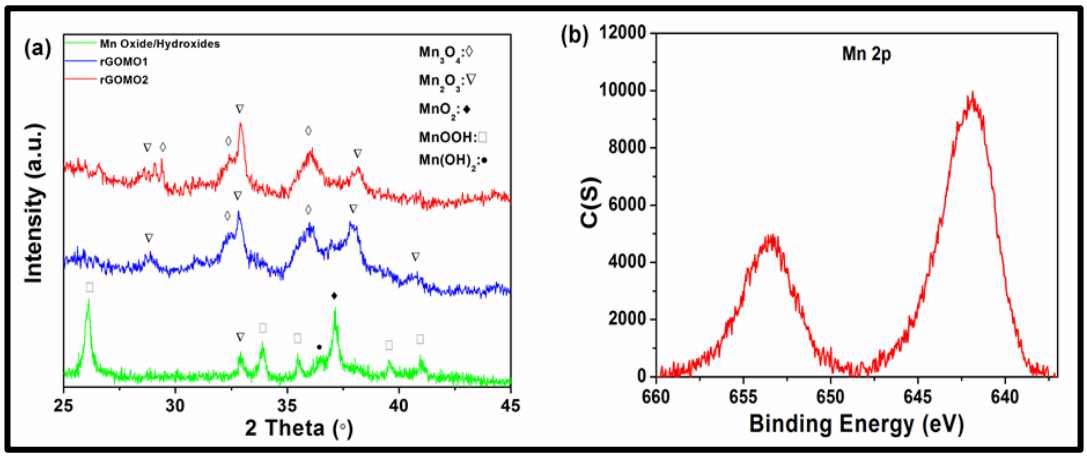

Figure 4.2: (a) XRD patterns of the manganese based composite showing the different phases present in the Mn Oxides/Hydroxides and the rGOMO materials spray pyrolyzed at 600˚C.**(b)** XPS spectrum of rGOMO1 sample in the Mn region.

From the onset, it is interesting to note that a mixture of phases exists in the composites after spray pyrolysis. A solution of Mn $(NO_3)_2 \cdot xH_2O$ without any GO, when sprayed, resulted in a mixture of oxides and hydroxides with different phases as shown in figure 4.2.The limited time (less than 1s) at which the suspension was exposed to a maximum heat of 600˚C resulted in incomplete conversion to the more thermodynamically stable Mn_2O_3 and Mn_3O_4. We therefore refer to this mixture as Manganese oxide-hydroxide. On the other hand, the XRD patterns of the hybrids made from nominal 1:12 and 1:7 (GO-Mn $(NO_3)_2 \cdot xH_2O$) ratios giving rise to rGOMO1 and rGOMO2 show mixtures of Mn_2O_3 and Mn_3O_4 with no traces of hydroxide after spray pyrolysis. The XPS spectrum of Mn region is also given in figure 4.2b. However it should be noted that due to the presence of a mixed valence state of 3 and 4, it is impossible to differentiate between hydroxide and oxide

samples. These composites clearly demonstrate that the spray pyrolysis of $MnO(OH)_2$ promotes the phase conversion according to the following pathway:

$$MnO(OH)_2 \rightarrow Mn(OH)_2 \rightarrow MnO(OH) \rightarrow MnO_2 \rightarrow Mn_2O_3 \rightarrow Mn_3O_4 \qquad (14)$$

Nonetheless, the addition of graphene oxide (GO) to the suspension and spray pyrolysis results in the conversion of $MnO(OH)_2$ to Mn_2O_3 and Mn_3O_4. XRD patterns suggest that at higher concentration of GO, characteristic peaks of Mn_3O_4 emerge more sharply. Therefore, higher concentration of GO seems to increase the kinetics of phase transformation of Mn_2O_3 to Mn_3O_4 that usually needs heat-treatment at temperatures in excess of 800 ˚C.[110, 192] We therefore propose that the amount of GO coupled with the temperature control can be used to control the phases required.

In the case of spray pyrolysis, due to the very short reaction time, the co-existence of Mn^{2+} and Mn^{3+} favours the formation of hausmannite (Mn_3O_4). [193, 194] The addition of GO sheets, which exhibit oxygen functional groups in the form of carboxyl, hydroxyl or epoxy groups on their basal planes and edges and water molecules in between the GO sheets, can therefore promote faster kinetics of conversion to hausmannite (Mn_3O_4). These functional groups, which also contain hydrogen, might alleviate the decomposition of manganese hydroxide compounds and the reduction of Mn_2O_3 to Mn_3O_4. Therefore, the existence of the higher percentage of Mn_3O_4 in rGOMO2 hybrid material compared to rGOMO1 can be attributed to the higher percentage of GO and consequently higher percentage of hydrogen containing functional groups. Field emission scanning electron microscopy (FE-SEM) was employed to investigate the morphology of the obtained samples. Figure 4.3 shows FE-SEM micrographs of all three samples where unique urchin like microstructures with manganese oxide needles are observed to grow radially from

the rGO core of the hollow spheres. Manganese oxides have the tendency to form nano rods or needle like structures.[27, 190, 195] Though the formation mechanism of the nanorods requires further investigation, the particles originating from the sprayed suspension are believed to orient themselves to form one-dimensional nanorods on the rGO sheets. Through oriented attachment along the side surfaces, 1D nanorods enlarge their diameter to become bulky nanorods in order to minimize the surface energy according to Li et al. [196]

In figure 4.3a and 4.3b, the nanorods between adjacent microspheres are observed to be entangled, creating a network on the electrode surface. However, higher amounts of GO sheets decrease the solubility of the Mn species, which is in agreement with the decrease in the length of nanorods upon increasing the percentage of GO in the solution. Moreover, the addition of GO dispersion (with pH of around 3-4) to manganese suspension increases the acidity of the suspension which results in proton chemisorption

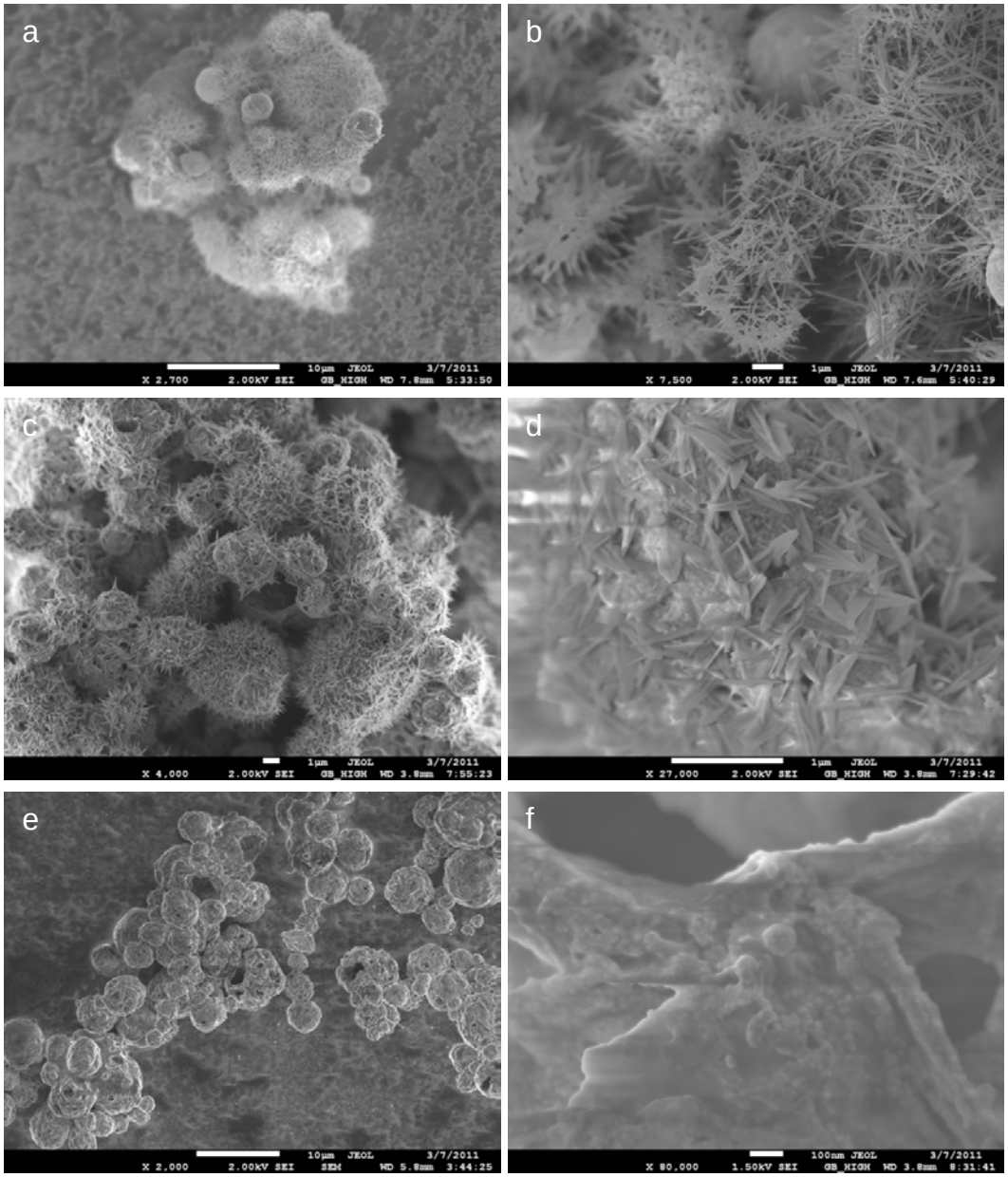

Figure 4.3: (a) Low magnification and **(b)** high magnification FE-SEM micrographs of manganese oxide/hydroxide with no rGO present showing an interconnected network of urchin like microsturctures of the manganese oxide/hydroxide. Low magnification **(c)** and **(d)** high magnification FE-SEM micrographs of rGOMO1 composite showing a decreased length in nanorods. **(e)** A further increase in the amount of rGO resulted in the complete absence of metal oxide nanorods but a homogeneous distribution of nanoparticles **(f)** on the rGO surface for rGOMO2.

which in turn stabilizes the surface of small particles and limits the growth stage as observed in figure 4.3c and 4.3d.[197] A combination of the nano particles and

spherically shaped graphene oxide sheets provide a porous network on the electrode surface ideal for charge storage. FE-SEM micrographs (In figures 4.3d and 4.3e) clearly suggest that an increase in the concentration of GO in rGOMO2, hinders further growth of manganese oxide needles upon keeping manganese oxide particles apart from each other. This is in agreement particularly with the BET results for the best performing rGOMO1 observed to be 139 m^2g^{-1} while that of the manganese oxide-hydroxide was only 29 m^2g^{-1}.

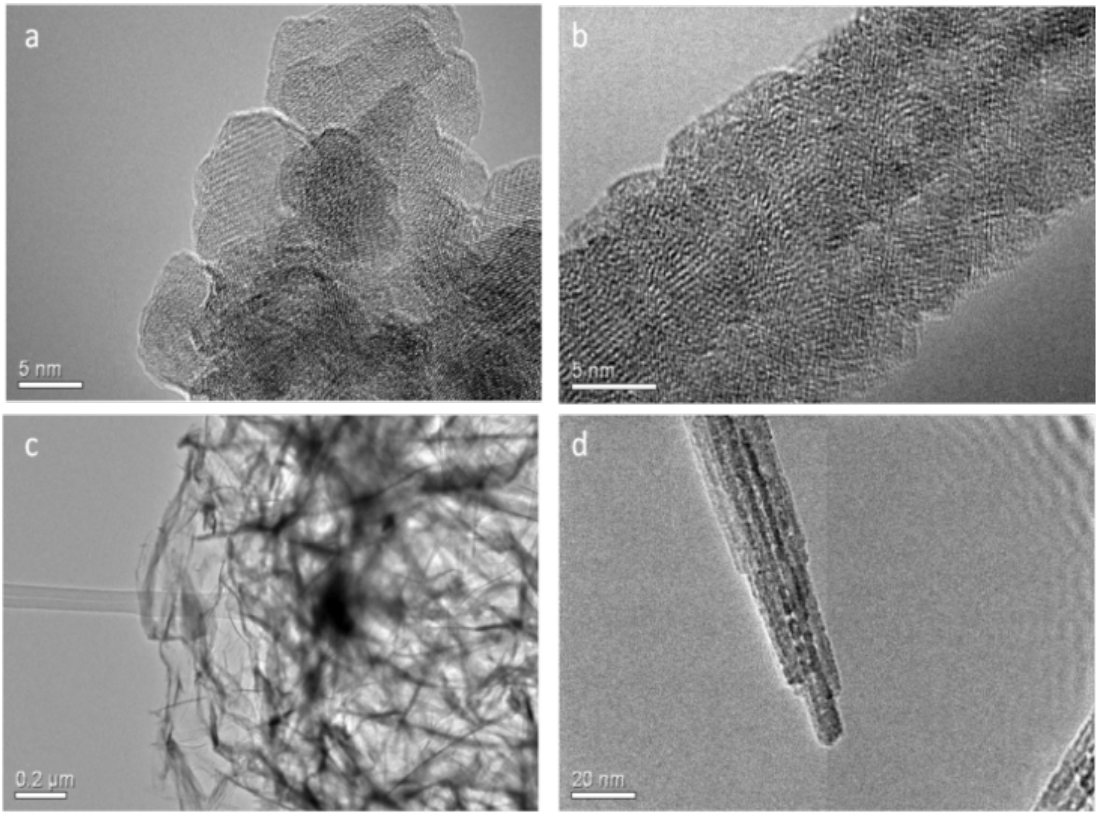

Figure 4.4 HRTEM micrographs of Manganese oxide-hydroxide showing **(a)** an agglomeration of nanoparticles which results in nanorods as shown in **(b)**. The combination of **(c)** rGO, Mn_2O_3/Mn_3O_4 and **(d)** a high magnification rGOMO1.

To further investigate the formation process, HRTEM was performed on the samples to reveal an aggregation of different primary nanoparticles in figure 4.4a. This suggests that the manganese oxide-hydroxide sample contains single crystal

nanoparticles which are in good agreement with the formation mechanism suggested above. The attachment of these single crystal nanoparticles to form nanorods and further orientation of these 1D nanorods to form bulky nanorods is also illustrated in figure 4.4b. The combination of manganese oxide nanorods with graphene oxide sheets is shown in figure 4.4c suggesting the hollow nature of the spheres. Upon closer inspection it can be clearly seen in figure 4.4d, that the nanorods are actually composed of a few primary nanorods aggregated along the lateral faces. [198]

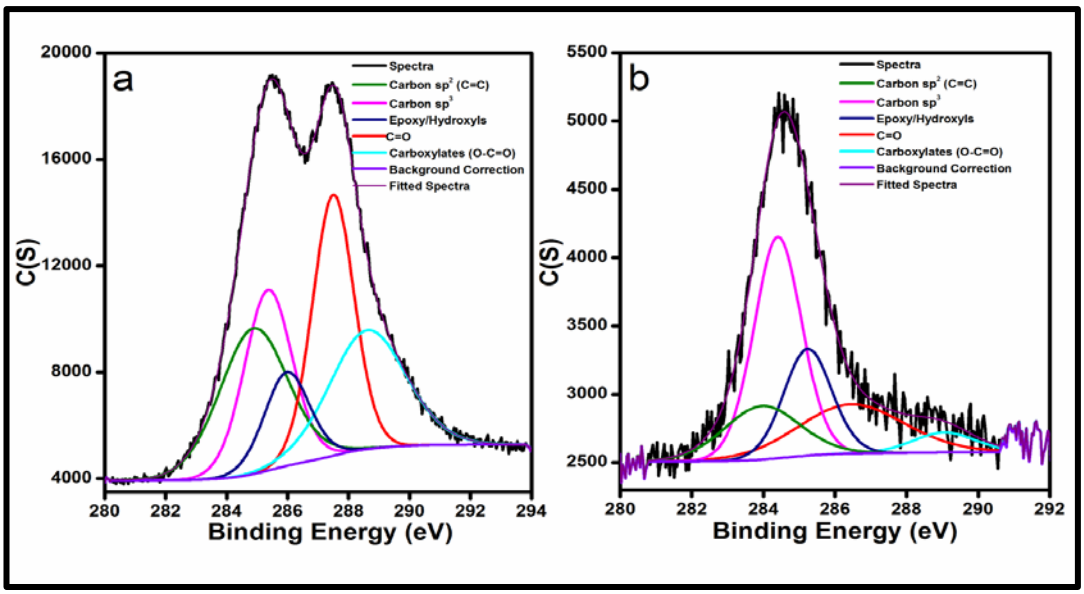

Figure 4.5 Fitted XPS C1s spectra of **(a)** as-prepared GO sample and **(b)** spray pyrolyzed sample at 600 °C.

Typical C1s spectra of both as-prepared graphene oxide and spray pyrolyzed sample at 600 ˚C obtained by XPS are shown in figure 4.5. Deconvolution and curve fitting of C1s spectra were performed using CASAXPS software employing a Gaussian-Lorentzian peak shape after performing a Shirley background correction. The C1s spectra mainly consist of 5 individual peaks namely: Carbon sp2, Carbon sp3, Epoxy/Hydroxyls, C=O groups and carboxylates. The significant increase in the ratio of carbon–carbon bonds to functional oxide groups (from 0.76 to 1.25) clearly suggests that spray pyrolysis can induce the graphene oxide to reduced graphene

oxide transition in spite of the very limited time of heat treatment (less than 1 second).

Cyclic voltammetry was used as the first diagnostic tool to electrochemically characterize the Manganese oxide-hydroxide and rGOMO composites as shown in figure 4.6a. A large current separation was observed for the rGOMO1 electrode suggesting higher capacitance compared to rGOMO2 and Manganese oxide-hydroxide electrodes.

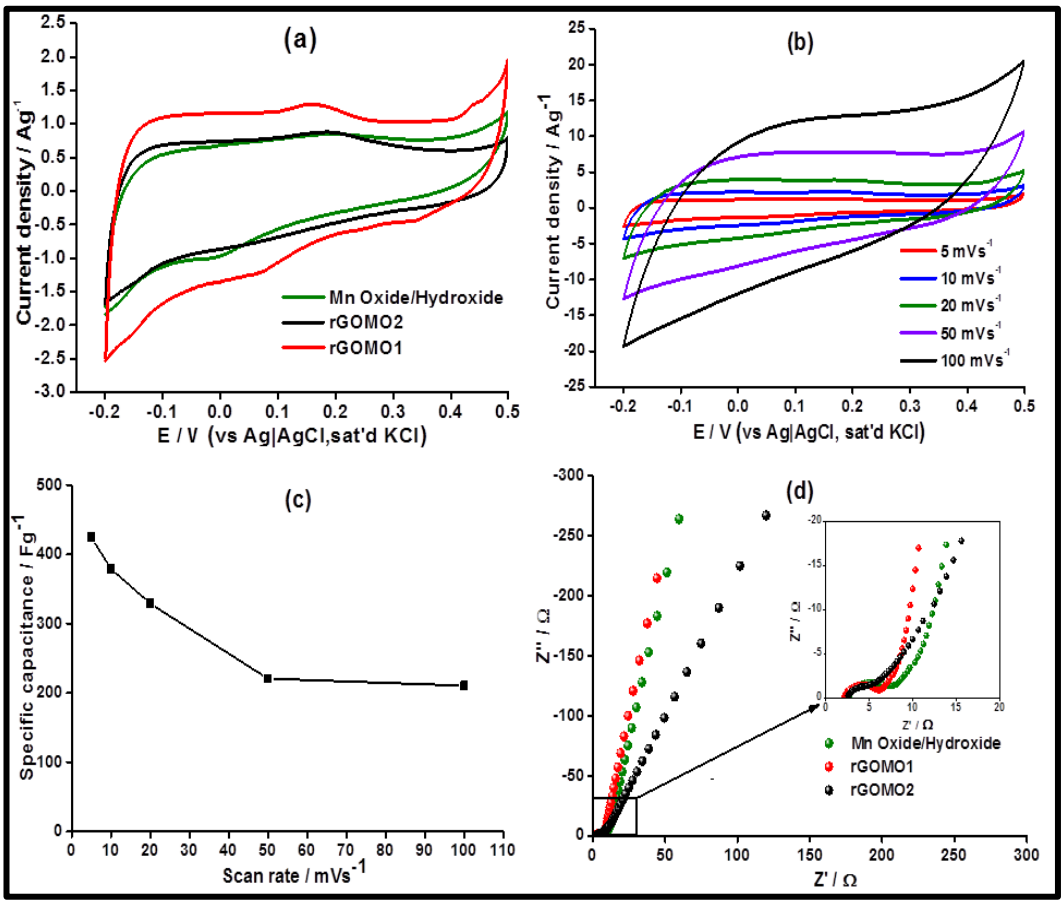

Figure 4.6 **(a)** Cyclic voltammograms of the composites at $5mVs^{-1}$. **(b)** Effect of scan rate on the shape of CV's of the best performing rGOMO1 electrode. **(c)** Variation of specific capacitance of the rGOMO1 composite electrode with scan rate. **(d)** Nyquist plots of the different composites showing the difference in charge transfer resistance in the high frequency region (inset). All experiments performed in 1 M NaOH.

The CV's deviate from the rectangular shape expected for an electrical double layer capacitor (EDLC) due to the pseudocapacitance contribution by the manganese oxides which is known to add to the overall capacitance due to the variable oxidation states exhibited by manganese. Individually, Mn_2O_3 and Mn_3O_4 have been meagerly reported in literature as supercapacitor electrodes with low capacitance due to poor conductivity. [61, 110] However, a mixture of Mn_2O_3 and Mn_3O_4 mixed with multiwalled carbon nanotubes (MWCNT) has been reported by Lin et al. to give better performance due to the pseudocapacitance arising from electron transfer at Mn sites and EDCL contribution by the MWCNTs. [199] Similarly, we observed the same phenomenon this time using rGO. The Mn^{3+} in Mn_2O_3 has been described as going through an oxidation reaction giving rise to one electron being transferred and attaining a valence state of Mn^{4+}.[110] Accordingly, the electrochemical reaction in equation 15 is expected to take place during the charge-discharge process involving OH^- chemisorption/intercalation into Mn_2O_3 structure.[110]

$$Mn\,[Mn]O_3 + OH^- \leftrightarrow 4Mn^{4+}[Mn^{3+}]OH^-O_3 + \bar{e} \qquad (15)$$

While the energy storage mechanism of Mn_3O_4 supercapacitor electrode materials has been recorded previously as a proton–electron mechanism, the CV peaks in figure 4.6a cannot be assigned specifically to a particular phase since rGO also possesses some oxide groups on its surface that are capable of participating in redox reactions. However, the overall effect is an enhanced capacitance due to the pseudocapacitance effect arising from all the constituent materials in the composite. The following formula was therefore used to calculate the specific capacitance of the electrode materials at different scan rates[158].

$$C = \frac{1}{mv(0.5-(-0.2))}\int_{-0.2}^{0.5} I(V)dV \qquad (16)$$

where m is the mass (g), υ the scan rate (mV/s), i the current (A) and V the voltage. The highest capacitance at 425 Fg^{-1} was recorded for the rGOMO1, followed by 388 Fg^{-1} for the rGOMO2 and 336 Fg^{-1} for the Manganese oxide-hydroxide at 5 mVs^{-1}. The highest specific capacitance for the RGOMO1 composite is much higher than that reported by Wang and co-workers for Mn_3O_4/graphene (256 Fg^{-1}) in alkaline solution. [189] Figures 4.6b and 4.6c show the variation in specific capacitance with increase in scan rate. As scan rate is increased, a drop in specific capacitance can be noted. This is due to the less effective interaction between electrolyte ions and the electrode at high scan rates. However, the 3D structure of the rGOMO1 material is essentially an ensemble of concealed interfaces which become accessible at low scan rates thereby increasing the electroactive surface area available for charge storage.[200]We therefore established that at 5 mVs^{-1}, the chemisorption and/or intercalation of OH^- into the microstructure is facilitated by the low scan rate hence the more pronounced peaks and higher capacitance. At high scan rates, the peaks become less pronounced (see figure 4.6b) due to the limited time for ions to reach some of the buried interfaces mentioned earlier.

Further tests to investigate mechanistic effects on the electroactive material such as ion transfer, conduction and capacitive behaviour were carried out using EIS. Figure 4.6d shows comparative Nyquist plots for the three electrodes in the three electrode set-up. The Nyquist plot is made up of two regions: the high frequency and low frequency regions with each point on the Nyquist plot representing a particular measurement taken at a specific frequency. From the inset in figure 4.6d, the small semi-circle observed in the high frequency region is due to charge transfer resistance

(R_{ct}) on the electrode/electrolyte interface. The intercept between the plots and the Z′ axis represents the ohmic resistance (R_s). From the plot, the manganese oxide/hydroxide material is observed to have a small R_{ct} (5.80 Ω) possibly due to the large number of nanorods that enhance the electrode surface area.[138] An addition of rGO clearly enhances the conductivity of the composite as can be observed from the reduction in the R_{ct} with increase in graphene oxide content in rGOMO2. The rGOMO1 hybrid material shows an R_{ct} value of 4.53 Ω while that of rGOMO2 is only 3.7 Ω. rGO therefore acts both as a conductive support as well as an agent for the uniform dispersion of manganese oxide nanoparticles in the composite thereby enhancing charge transfer within both electrode materials.

The specific capacitance values calculated from the charge-discharge method using equation 17 are in agreement with those from CV with the rGOMO1 achieving a specific capacitance of 356 Fg^{-1} followed by rGOMO2 with a specific capacitance of 249 Fg^{-1} and 178 Fg^{-1} for the Manganese oxide-hydroxide at 0.35 Ag^{-1}.

$$C = i(A) \times \Delta t(s)/m(g) \times \Delta E(V) \qquad (17)$$

where *i*, is the discharge current in amperes, *t*, the discharge time in seconds, *m*, the mass of the active material in grams and ΔE, the potential window in volts. From the values achieved, we can attribute the outstanding performance to the distinctive 3D network (combination of nanotubular whiskers and nanoparticles homogenously distributed on the surface of mircospheres), synergy between metal oxide and the transition from GO to rGO after the spray pyrolysis. The rGO has been reported to be more conducting and also more capacitive than GO also showing good power capabilities. [201]

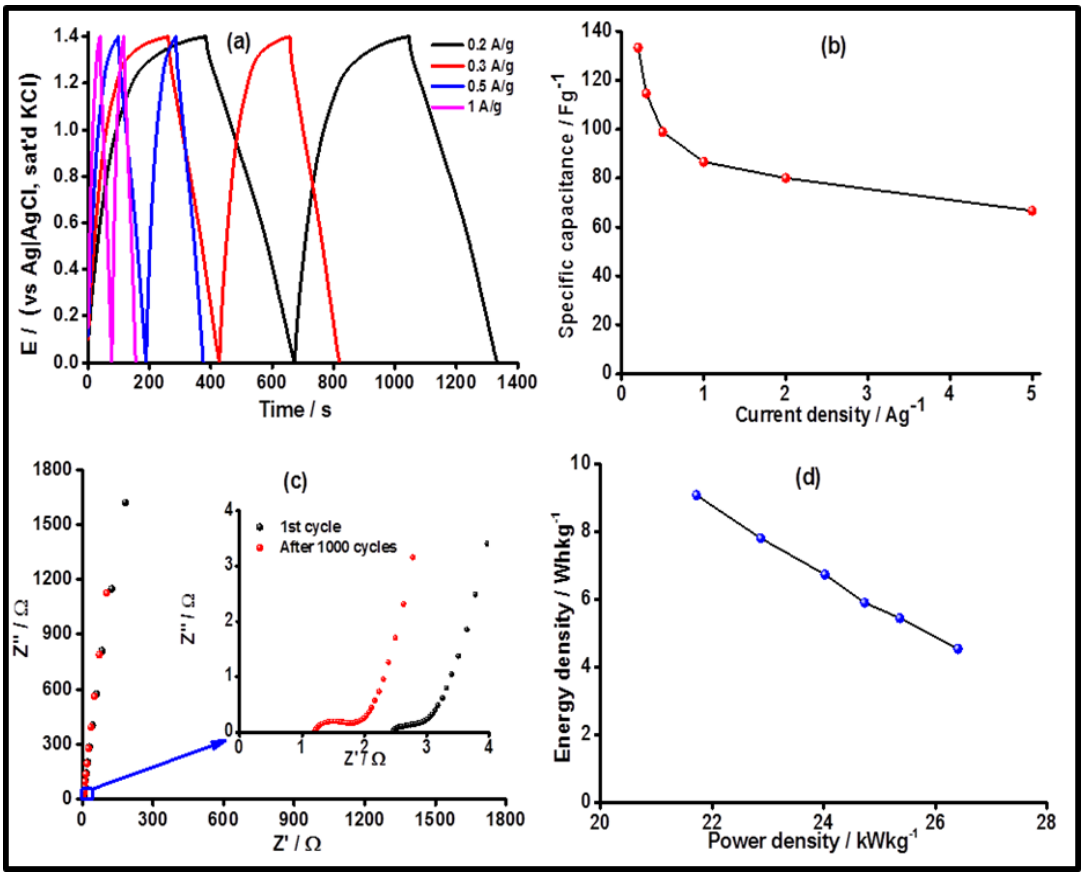

Figure 4.7(a) Charge discharge profiles of the asymmetric supercapacitor device at different current densities.**(b)** Effect of current density on the specific capacitance. **(c)** Nyquist plots of before and after 1000 cycles showing differences in the high frequency region (Inset). **(d)** Ragone plot showing the relationship between energy density and power density.

4.3.2 Asymmetric supercapacitor

An asymmetric supercapacitor was fabricated using the rGOMO1 as the cathode and graphene as the anode in 1M NaOH electrolyte. A maximum value of 133 Fg^{-1} was recorded at 0.2 Ag^{-1} using the charge discharge results in figure 4.7a and calculated using the formula:[202]

$$Cs = 4 \times \frac{i \times t}{V \times m_{\pm}} \qquad (18)$$

Where *i*, is the current in Amperes, *t*, the discharge time in seconds, *V* the voltage

and $m_{\pm}$ the total active mass of the positive and negative electrodes in grams.

The specific capacitance was also calculated for higher current densities yielding 115, 99, 87, 80, and 67 Fg^{-1} at 0.3,0.5,1, 2 and 5 Ag^{-1} respectively as shown in figure 4.7b. This is higher than the specific capacitance of 70 Fg^{-1} at 10 mVs^{-1} recorded for a graphene/MnO_2/CNT device fabricated by Cheng et al.[167] These high values are due to the pseudocapacitance and EDLC contributions of the materials in the hybrid material as mentioned earlier. The shape of the charge-discharge curves in figure 4.7a slightly deviate from the linear profiles expected for EDLC due to the strong pseudocapacitance contribution by the combination of manganese oxide phases within the composite. This is in agreement with the CV's in figure 4.6a which also show a distorted rectangular shape.

So far we have shown that the composite electrode material between manganese oxides and rGO results in enhanced capacitance. Following this, high energy and power densities of the asymmetric supercapacitor assembly should be expected due to the high surface area of rGO implying high power density while the manganese oxide has a high energy density. This synergy between the constituent materials results in a robust asymmetric device with an energy density of 9.07 $Whkg^{-1}$ and a power density of 26.4 $kWkg^{-1}$. These values were calculated using equations 19 and 20 from the galvanostatic data.

$$SE(Wh/kg) = i(A) \times \Delta t(s) \times \Delta E(V)/m(kg) \qquad (19)$$

$$SP(W/kg) = SE/t \qquad (20)$$

where i is the current in amperes, Δt, the discharge time in seconds, ΔE, the voltage window and m, the mass in kg. A Ragone plot (see Figure 4.7d) was generated which shows a clear relationship between the energy density and the power density as an efficient way to evaluate the electrochemical performance of supercapacitor device.

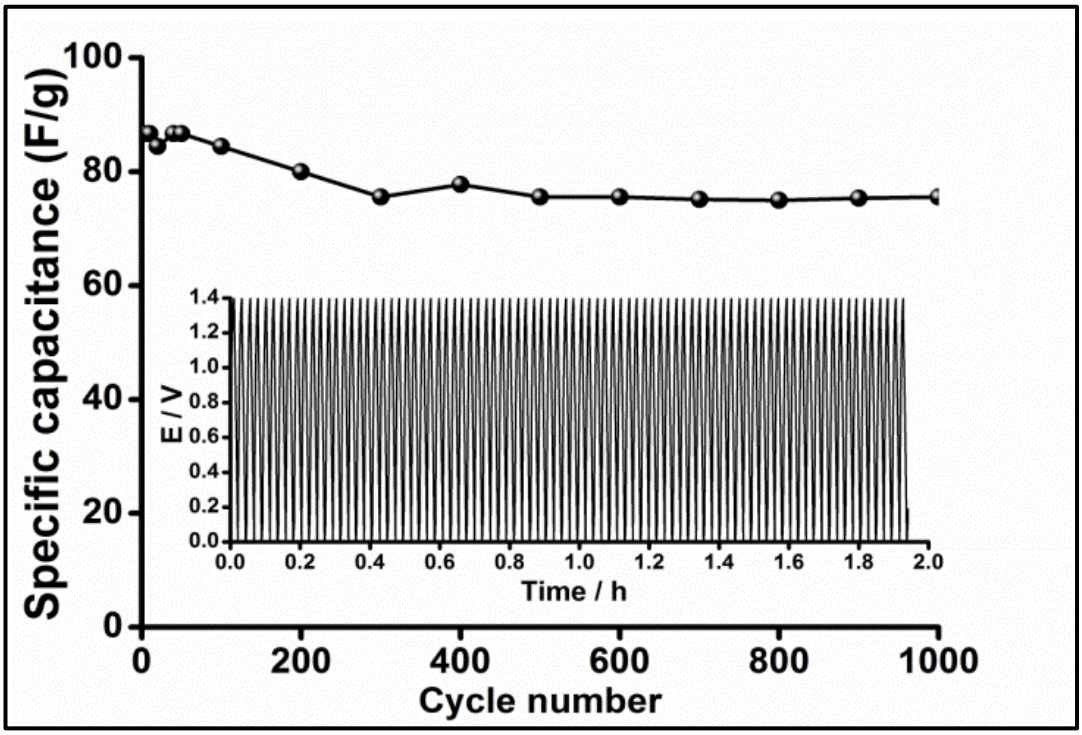

Figure 4.8: Cycle life of the assembled asymmetric supercapacitor device tested over 1000 cycles at a current density of 0.2 Ag^{-1} within a potential window of 1.4 V.

One of the characteristics that make supercapacitors more attractive energy storage devices when compared to batteries is the long cycle life of these devices. In light of this, a cycle life test was performed over 1000 cycles with the capacitance retention recorded at 2 Ag^{-1} using charge-discharge. A capacitance retention of 83% shown in figure 4.8 can be attributed to the presence of the more stable rGO support and graphene anode in the device. Carbonaceous materials are well known to possess remarkable cycling stability which renders the supercapacitor device appropriate for practical applications. Accordingly, the excellent interfacial contact between the Mn_2O_3 and Mn_3O_4 and formation of nanorods effectively prevent the agglomeration and restacking of graphene sheets thereby enhancing the electrochemical activity of the composites. Additionally, the presence of rGO in the final electrode materials assists in improving the conductivity of the poorly conducting Mn_2O_3 and Mn_3O_4

resulting in an enhanced electrical double layer capacitance to the overall specific capacitance, resulting in rapid charge/discharge process.

4.4 Summary

In this chapter hybrid structures of nanoneedle-shaped manganese oxide and spherical graphene oxide have been synthesized for the first time using an in-situ spray pyrolysis strategy. The resulting urchin-like morphologies with high surface area (139 m^2g^{-1}) form a network on the electrode surface. The combination of reduced graphene oxide with manganese oxide clearly results in very good electrochemical performance (425 Fg^{-1} and 9.07 $Whkg^{-1}$) of the hybrid material. This is due to the electrical double layer capacitance from graphene oxide and pseudocapacitance from manganese oxide, which is in agreement with a recent report on GO/MnO_2 asymmetric capacitor.[154] The overall capacitance retention (83%) over 1000 cycles is high enough for the material to be considered as a potential candidate for supercapacitor electrodes and other energy devices. The method and approach can be used for synthesis of other graphene-metal oxide electrodes for energy storage.

5 GRAPHENE OXIDE-COBALT OXIDE AND NICKEL OXIDE NANOCOMPOSITES

5.1 Graphical Abstract

We engineer lettuce like structures of rGO-MO composites that exploit both electrical double layer and pseudocapacitor qualities of the constituent materials to produce high performance supercapacitor electrodes.

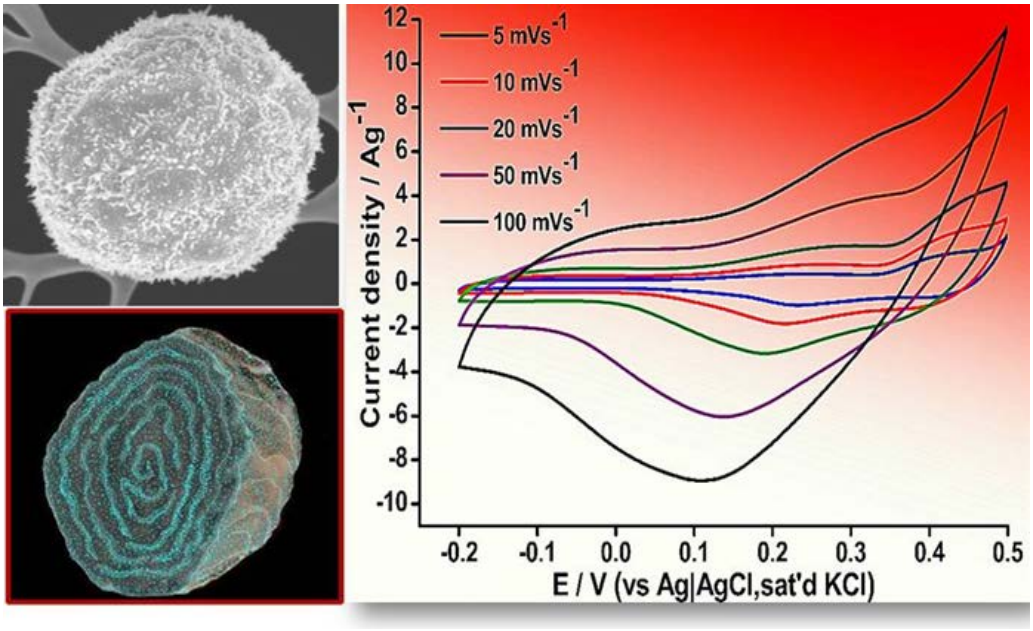

Figure 5.1: Graphical outlinet showing a brief overview of the performance and structure of the materials tested in this chapter.[28]

5.2 Introduction

In the present chapter we report the large scale engineering of globularly shaped rGO-MO nanocomposites (MO = Co_3O_4 or NiO) using an efficient and versatile in-situ spray pyrolysis approach. These structures demonstrate superior energy storage performance and good structural stability after cycling. We show that this approach can be applied to a range of metal oxide materials and demonstrate that the electrochemical properties can be much improved. Previously,[203] we

demonstrated the advantages of the spray pyrolysis engineering to obtain other type of Si/Carbon composites with superior performance as anode material in Li-ion batteries.

5.3 Results and Discussion

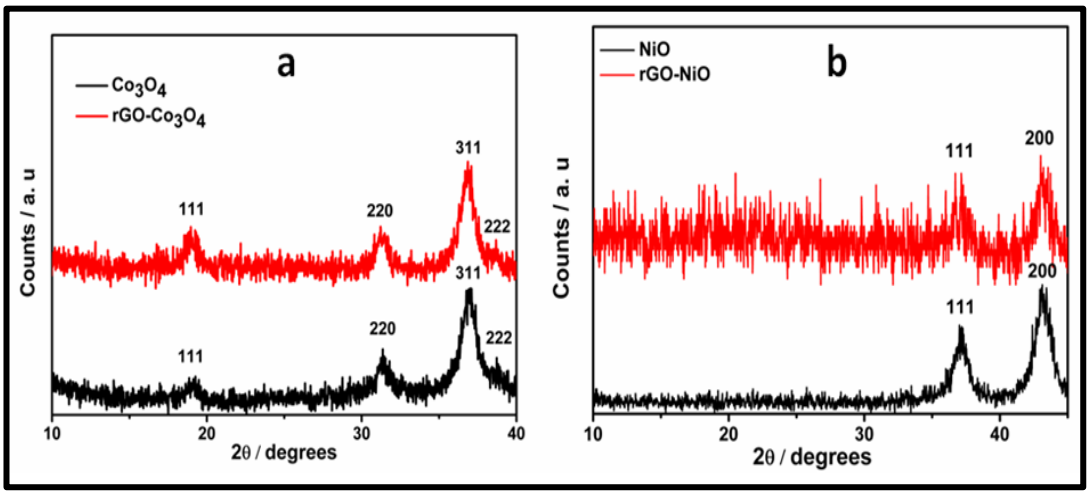

Figure 5.2: XRD profiles for **(a)** Co_3O_4 and rGO-Co_3O_4 and **(b)** NiO and rGO-NiO composites after spray pyrolysis.

The structure of the obtained hybrid composite was evaluated employing X-ray diffraction and Scanning electron microscopy techniques. All the diffraction peaks of both rGO–Co_3O_4 and rGO-NiO were perfectly indexed to cubic Co_3O_4 and NiO structures as shown in figure 5.1a and b respectively. Additionally, no peak of graphene was detected thus suggesting that graphene sheets were homogeneously dispersed in the composite.[204] This was also supported by the EDS mapping for the rGO-Co_3O_4 composite in figure 5.2.

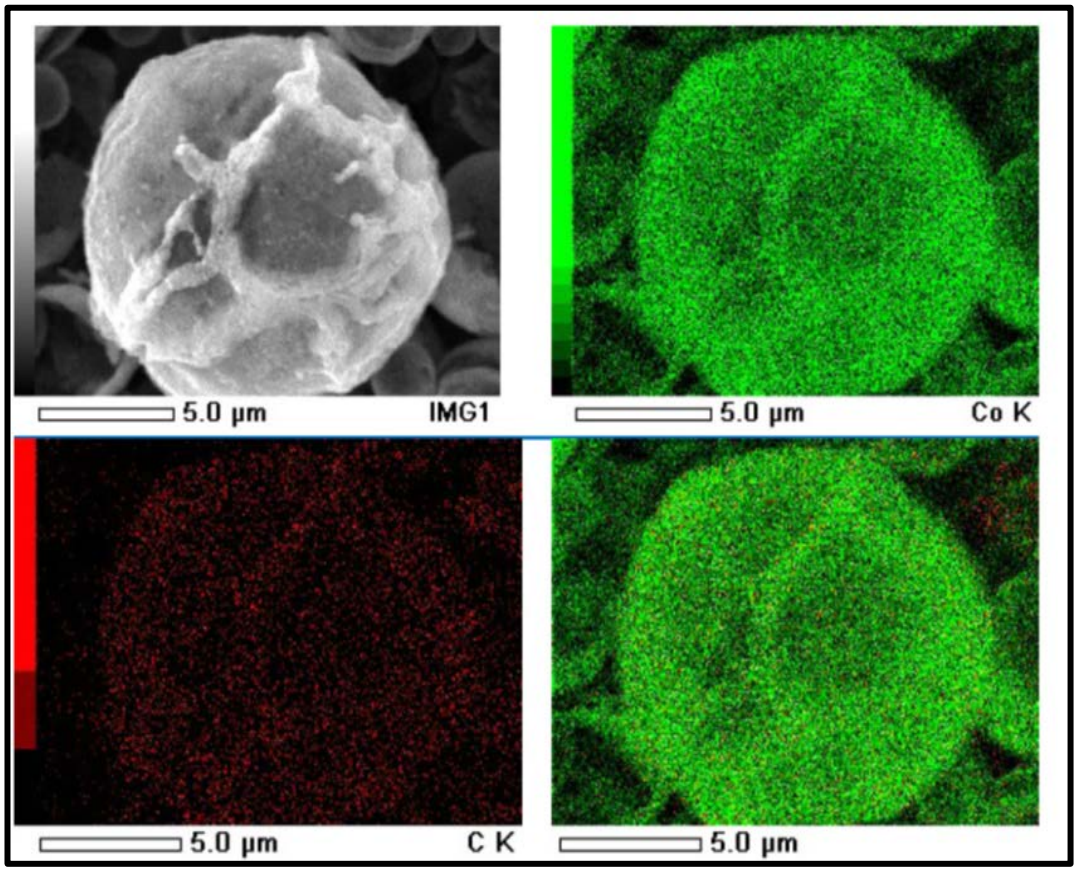

Figure 5.3: The EDS mapping showing good homogeneity of the obtained nanocomposite particles, demonstrated by the substantially even distribution of Co and carbon across the sample.

Being amphiphilic in nature [26, 168], the hydrophilic parts of GO sheets can quite easily interact with hydrophilic metal nitrates resulting in strong bonding between GO sheets and the starting precursor. Therefore, the nucleation and growth of MO nanocrystals during the spray pyrolysis take place predominantly on the surface of GO sheets. The solid matrix of graphene then prevents these particles from excessive coagulation and coalescence into larger aggregates. Furthermore, the reduction of GO to rGO occurs during the process and this is confirmed by XPS spectra (see figure 5.3).

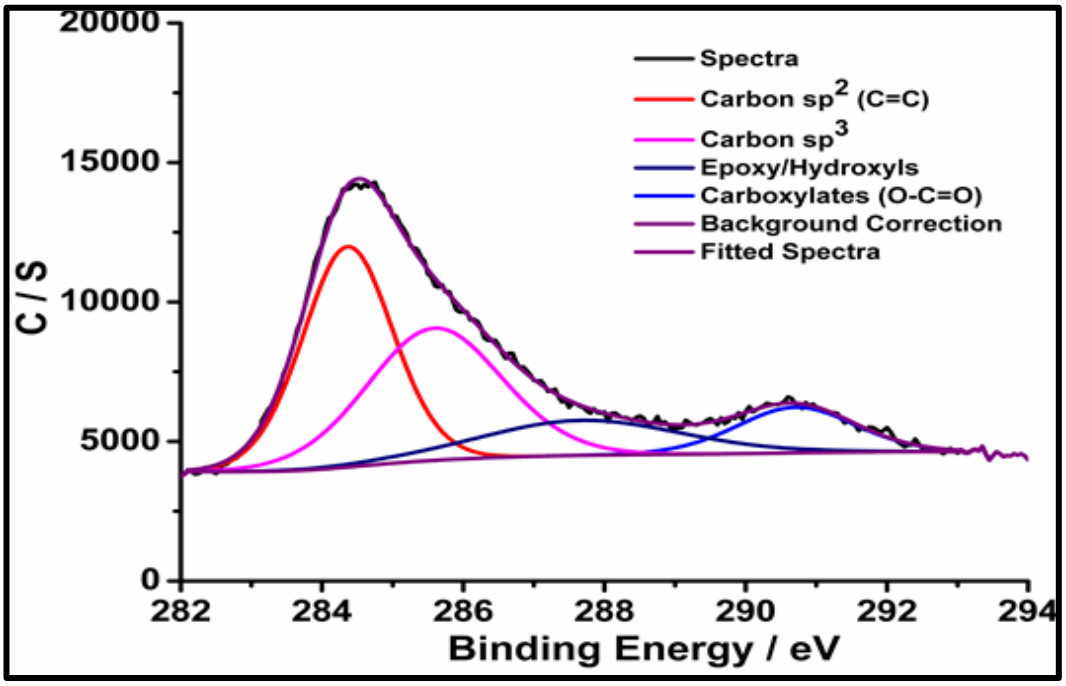

Figure 5.4: XPS spectra of rGO-Co_3O_4 composite after spray pyrolysis.

The introduction of large GO sheets which are typically in the size of 30 µm [168], resulted in the formation of composite globules. (Figure 5.4a, b). HRSEM was used to investigate the morphology of the composites. In figure 5.4 a and 5.4b, the rough globular surface due to the presence of nanoparticles and porous nature of the MO contribute significantly to the overall electrochemical performance of the materials. This structure allows the penetration by the electrolyte and consequently facilitating Faradaic reactions. The incorporation of larger rGO sheets (Figure 5.4a) in the composite structure which are observed to form a lettuce-like structure is also advantageous in terms of enhanced electrical conductivity. Additionally, their presence leads to an increase in both double layer capacitance and electrochemical stability of the composites.

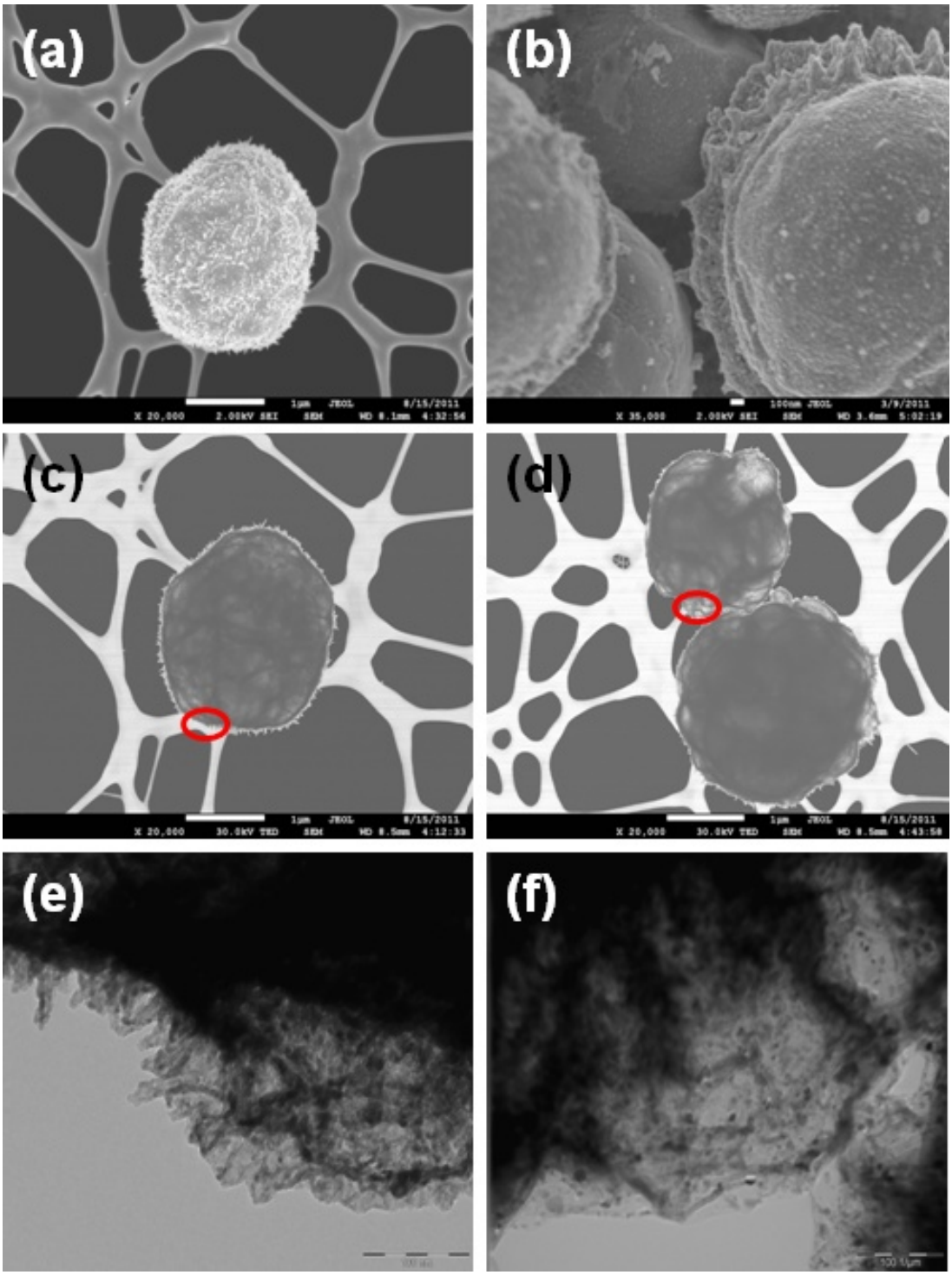

Figure 5.5: SEM images of **(a)** Co_3O_4 and **(b)** NiO after spraying. **(c)** TEM images of rGO-Co_3O_4 and **(d)** rGO-NiO composites with highlighted areas expanded in figures **(e)** and **(f)**.

The typical TEM images, shown in figures 5.4c and d reveal the globular lettuce-like structure of the composite particles. The images in low magnification

(Figures 5.4c and 5.4d) elucidate the envelopment of MO particles within bended rGO sheets resulting in the formation of an interconnected three dimensional network structure. This interconnected structure offers the unique advantages of both introducing conductive pathways through the whole structure and simultaneously improving the mechanical strength of the final composite. It can also be observed from the highlighted areas in figures 5.4c and 5.4d in high magnification (Figures 5.4e and 5.4f) that metal oxide nanoparticles grown on rGO sheets are quite homogeneously and densely distributed.

The graphene encapsulated spheres showed crinkled and rough textures that were associated with the presence of flexible and ultrathin graphene sheets. Although, it is almost impossible to rule out the possibility of some degree of restacking of reduced graphene oxide sheets into graphene stacks during the spray pyrolysis process, TEM observation of the edge of one individual globular structure demonstrated the monolayer nature of rGO obtained by this method. Nevertheless, an ordered, layered nanostructure with metal oxide and the graphene materials is formed. This particular arrangement is responsible for the high capacitive behaviour as the contribution of pseudocapacitance of the MO and double layer contribution of the carbonaceous material is exploited. Furthermore, rGO provides good conductivity which is supported by the small charge transfer resistance shown in the Nyquist plots.

Cyclic voltammetry was used as the first diagnostic test to study the electrochemical properties of the composites. Figure 5.5 shows CV results with figure 5.5(a) and (b) showing the individual CV curves for the two rGO-MO nanocomposites. From figure 5.5(a) the cyclic voltammograms for both NiO and rGO-NiO nanocomposite show redox peaks at 0.45 V and 0.22 V due to the

$Ni(OH)_2$/NiOOH redox reaction[145 205]. These peaks are accompanied by a broad shoulder peak between 0.1 and 0.35 V probably due to oxygenated groups on the rGO. In figure 5.5(b), redox peaks observed for rGO-CO_3O_4 are believed to be from reactions reported earlier [105]. The effect of the rGO is clearly visible from the increase in background current in the CVs.

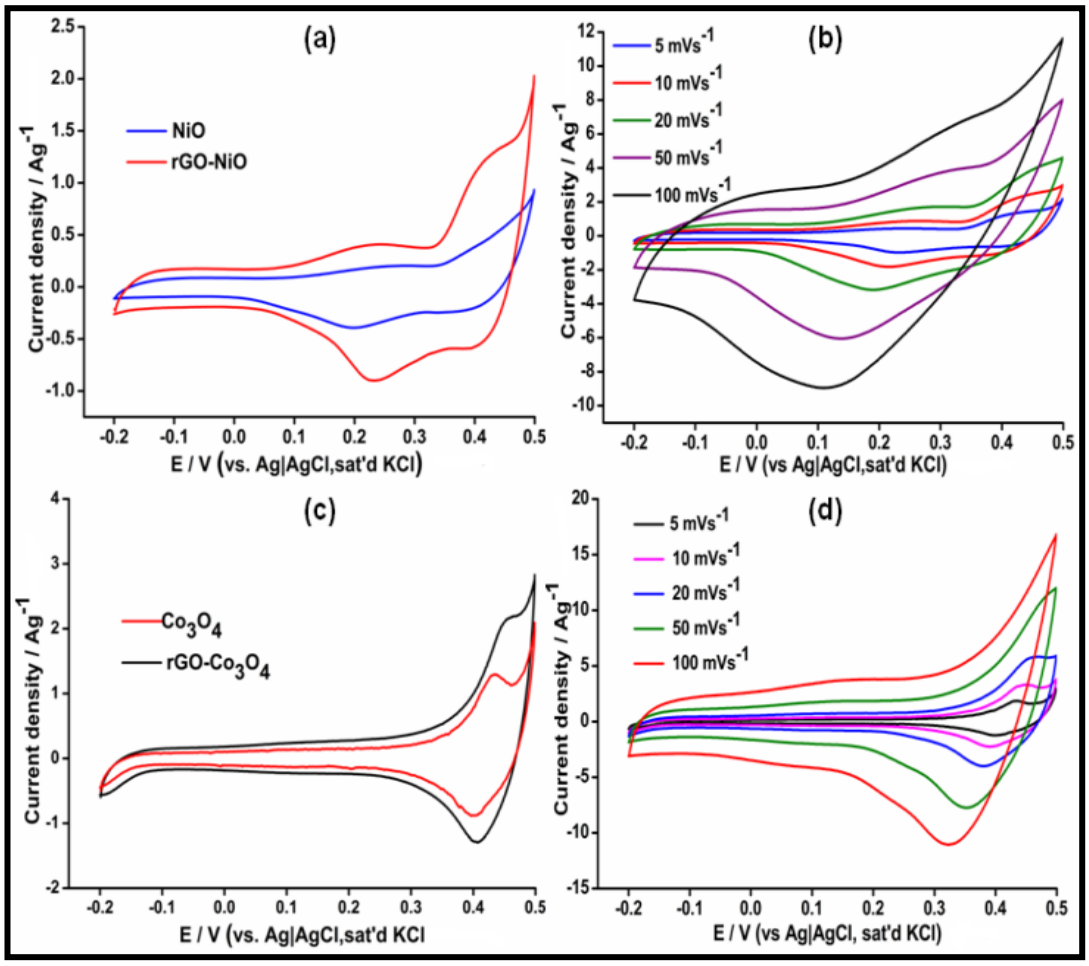

Figure 5.6: Comparative CVs at 5mVs^{-1} **(a)**, **(c)** variation of specific capacitance with scan rate **(b)**, **(d)** for the rGO-MO composites.

Both the rGO-MO CVs deviate from the rectangular shape expected for typical EDLCs. This is due to the pseudocapacitance contribution from the metal oxides as reduced graphene oxide has a capacity of about 205 Fg^{-1} [206]. The large current separation therefore indicates increased capacitive behaviour which was calculated

by integrating the area covered by the CV [26]. A total capacitance of 687 Fg^{-1} was obtained for the rGO-Co_3O_4 composite while that of rGO-NiO was 656 Fg^{-1} composite at 5 mVs^{-1} which is much higher compared to other graphene based supercapacitors reported in literature (Table 5.1).

Table 5.1: Graphene based composites used for supercapacitors.

Composite	**Electrolyte**	**Method of preparation**	**Specific capacitance(Fg^{-1})**	**Ref.**
rGO- Co_3O_4	1 M KOH	Spray Pyrolysis	687	Current study
rGO- Co_3O_4	6 M KOH	Surfactant and post annealing	163.8	[102]
GNS- Co_3O_4	6 M KOH	Microwave assisted method	243.2	[155]
Graphene–Co_3O_4	2 M KOH	In-situ solution based method	478	[207]
Graphene-MnO_2	1 M Na_2SO_4	Microwave Irradiation	310	[104]
rGO- NiO	1 M KOH	Spray Pyrolysis	656	Current study
GO-NiO	1 M KOH	Electrophoretic deposition and chemical-bath deposition	400	[208]
Graphene Sheet-RuO_2	1 M H_2SO_4	Sol-gel + low temperature annealing	570	[106]
GO-SnO_2	1 M KCl	ultrasonic spray pyrolysis	42.7	[126]
GO-ZnO	1 M KCl	ultrasonic spray pyrolysis	61.7	[126]

The charge storage mechanism of the two metal oxides has been described in previous reports as being analogous [134]. The spray pyrolysis route enables excellent encapsulation of these metal-oxide particles within graphene sheets thus leading to remarkable performance and cyclability. Graphene clearly enhances the electrochemical properties of the nanocomposites by first acting as a conductive support ideal for electron and ion transportation. Secondly, the graphene capsule stabilizes the electrode structure with a good electric contact between the metal oxide particles and conductive graphene during the charge−discharge process.

Additional tests showed a reduction in capacitance with increase in scan rate being more pronounced for the NiO composite while the rGO-CO_3O_4 shows better capacitance retention in figure 5.6 a and 5.6b. A specific capacitance of 580 Fg^{-1} for rGO-CO_3O_4 at 100 mVs^{-1} reflects good rate capacity and power density. We therefore concluded that the three-dimensional conducting network formed by the interaction between CO_3O_4 particles and graphene oxide, coupled with the high porosity of the composite facilitated OH^- soaking into the bulk material. This resulted in a decrease in the ionic and electronic transportation distances thus improving the electrode kinetics consequently enhancing the rate capability [152].

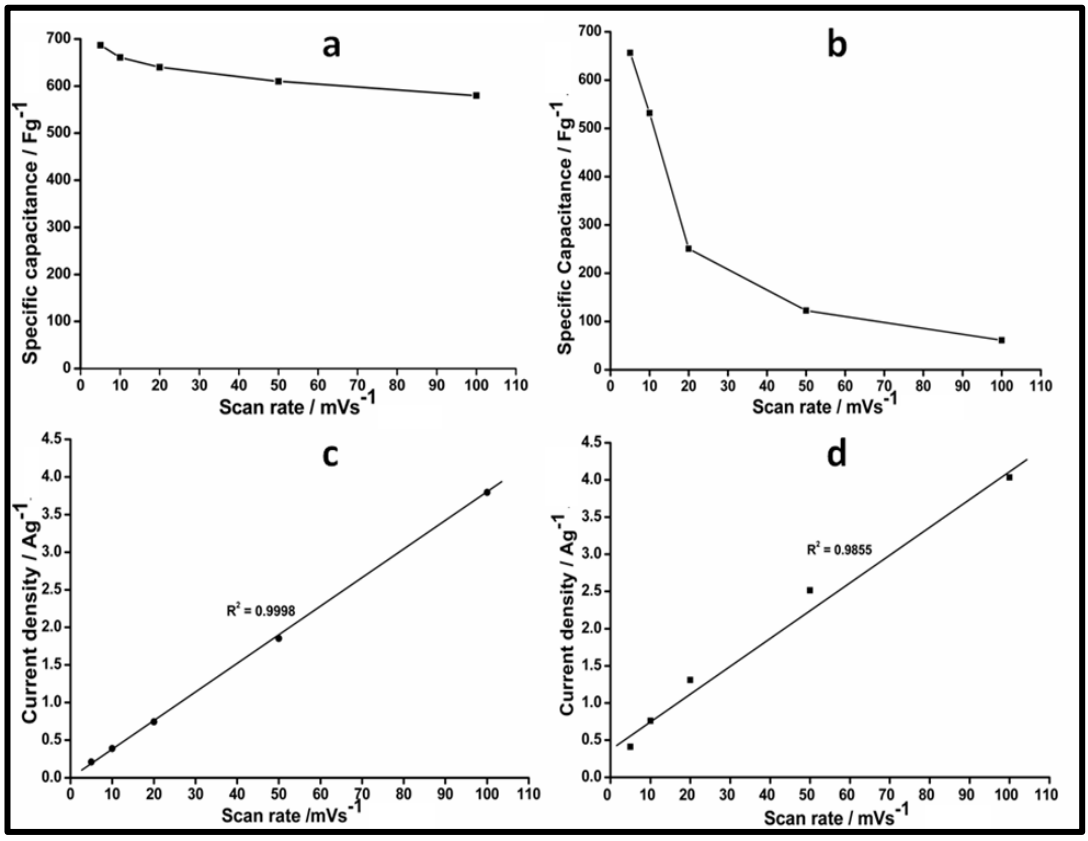

Figure 5.7: Variation of specific capacitance with scan rate for **(a)** rGO-Co_3O_4 and **(b)** rGO-NiO and current density with scan rate for **(c)** rGO-Co_3O_4 and **(d)** rGO-NiO.

rGO-NiO electrodes showed poor rate capability due to the insertion of OH^- ions being limited to the electrode surface as a consequence of lower conductivity when compared to Co_3O_4. The inner active sites within the electrode therefore do not get accessed at high scan rates by the electrolyte and cannot precede the redox transitions completely. Both electrodes however, show ideal capacitive behaviour as shown in the plots for current density vs. scan rate (see figure 5.6c and 5.6d).

Electrochemical impedance spectroscopy tests were performed for both rGO-MO electrodes to understand the capacitive behaviour and resistance associated with the electrodes. Supercapacitors generally behave as pure resistors at high frequencies and typical capacitors at low frequencies.

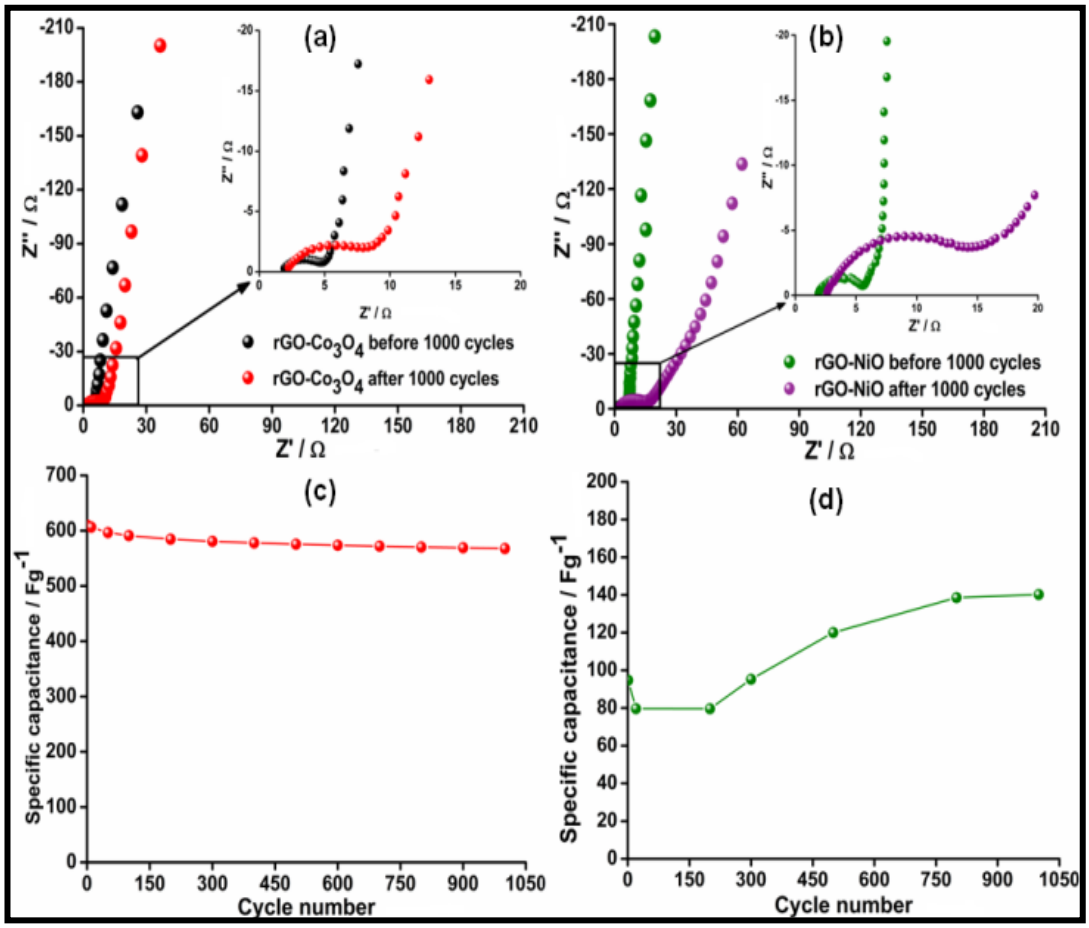

Figure 5.8: **(a)** Nyquist plots for GO-Co_3O_4 composite before and after 1000 cycles. **(b)** Nyquist plots for GO-NiO composite before and after 1000 cycles. (Inset: expanded high frequency region). Variation of specific capacitance with cycle number for GO-Co_3O_4 **(c)** and GO-NiO **(d)** obtained at 50 mVs^{-1}.

In the high frequency region, a semicircle due to charge transfer resistance on the electrode/electrolyte interface is observed. The region between the high frequency and low frequency regions is called the Warburg region and this is a combination of both resistive and capacitive behaviour characterized by diffusive resistance. The low frequency region is mainly characterized by purely capacitive behaviour. The Nyquist plots generated from the impedance data for the composites are shown in figure 5.8a and 5.8b. Both impedance spectra are similar, exhibiting the characteristic high frequency region semicircle and low frequency vertical line. The

insets show the expanded high frequency region where in both figures, an increase in the semicircle radius implying an increase in the R_{ct} with increase in scan number is highlighted. The rGO-Co_3O_4 shows a slightly lower R_{ct} value as compared to the rGO-NiO composite due to a more conductive nature of Co_3O_4 as compared to NiO. In some instances, Co_3O_4 has been added to NiO to improve stability of the oxide electrode.[209] NiO is also reported to be sensitive to temperature conditions during synthesis which affect its porosity and consequently electrochemical behaviour. Due to it's lower conductivity, an NiO electrode thus requires more activation time to perform at its maximum ability as shown in figure 5.8d.[14] This behaviour is consistent with the Nyquist plots as well as figure 5.7 a and b. At low frequencies, the Nyquist plots become more vertical, implying purely capacitive behaviour. However, after 1000 cycles the slopes decrease towards an angle of 45° implying a decrease in the phase angle and a deviation from ideal capacitive behaviour and a domination of Warburg diffusion.

Cyclic voltammetry was employed to determine the stability of the rGO-MO composites at 50 mVs^{-1}. As shown in figure 5.7b the specific capacitance for the rGO-Co_3O_4 electrode decreased by 6.9% demonstrating ideal stability for supercapacitors. Interestingly, the specific capacitance of the rGO-NiO electrode increased gradually by 48% of the initial value during the first 600 cycles. This is a due to the activation of the rGO-NiO active material. This phenomenon has also been observed by Yuan et al. [145]. The stability profiles of the two electrode materials entail the suitability of the materials for practical supercapacitor electrodes.

5.4 Summary

In this chapter, we have synthesized for the first time globularly shaped rGO-MO composites with high performance for supercapacitor electrodes using spray pyrolysis method. Additionally, the spray pyrolysis method proved to be an efficient method to effectively encapsulate MO particles with rGO simultaneously. The resulting composites exploit the benefits of pseudocapacitive nature of the metal oxide and conductive EDLC nature of the rGO. The technique also presents an opportunity to produce industry scalable ordered rGO-MO composites using a variety of metal oxides for both batteries and supercapacitors.

6 LIQUID CRYSTALLINE DISPERSIONS OF GRAPHENE OXIDE BASED COMPOSITES

6.1 Introduction

The synergy and self-assembly of individual components in carbon based composite electrodes plays a pivotal role in determining the overall performance of a supercapacitor. We report an in-situ method for fabricating ternary composites made up of liquid crystalline graphene oxide, MWCNTs and Nickel oxide nanoparticles. The resulting porous materials exhibit high capacitance and remarkable stability.

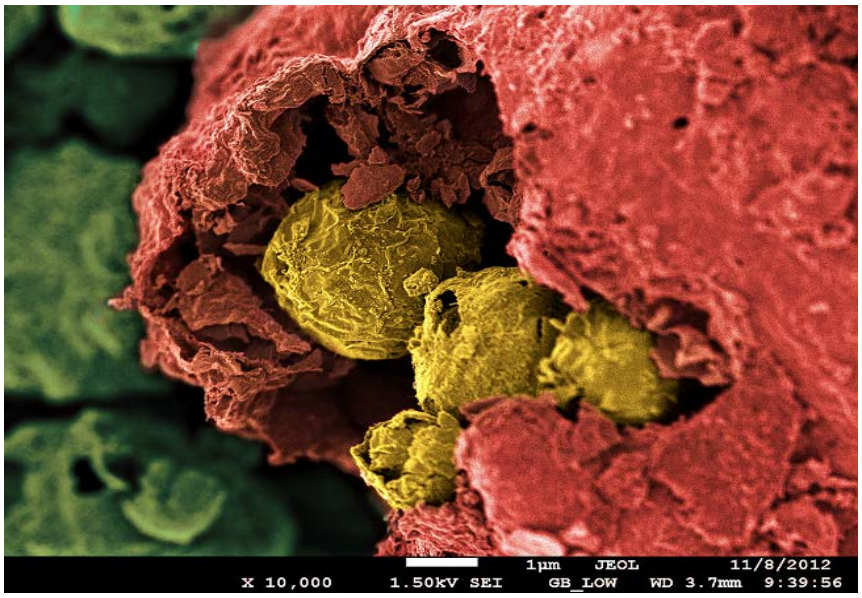

Figure 6.1: A glimpse into the morphology of the ternary structures synthesized and reported in chapter 6 highlighting the hierachichal nature of the composites.[210]

Inspired by the synergistic effect in hybrid architectures of CNTs and graphene while also relying on the combination of pseudocapacitive nature of metal oxides or polymers to increase capacitance, ternary architectures comprising of graphene, CNTs and metal oxides or polymers have also been reported. [83, 166, 167] Although high capacitance values have been reported, these hybrid architectures have not lived up to their promises of delivering the ultimate capacitance. So far, their charge

storage capacity lags far behind the hybrid architectures of reduced graphene oxide and metal oxides (as high as 687 Fg^{-1}).[28] This mainly arises from the very random and much agglomerated structure of these materials which cannot be avoided through the use of normal preparation methods such as hydrothermal route.

Therefore, further breakthroughs in design of new ternary systems, not incremental changes, hold the key to achieve the ultimate performance. Thus, architectural engineering of these materials both at nano and macro-scales, if achieved, not only can result in unrivalled capacitance performance but also opens the door to the next generation of energy storage systems. Of those few practical strategies to make self-assembly at different length-scales (nano to macro-scale) possible, taking advantage of nematic liquid crystallinity (LC) of graphene oxide (GO) in organic and aqueous media to make self-ordered and self-assembled ternary architectures seems to be the most plausible route.[168-170] Relying on a whole range of super molecular interactions, liquid crystals of GO have been used as prototype materials of choice to promote self-ordering and self-assembly at both nano and macro-scale levels while preserving the inherent properties of constituent materials.[211] This property has been used so far to fabricate multifunctional architectures such as fibers and papers.[168, 212-214] Moreover, the directionality of nematic LCs also provides us with the opportunity to design and assemble complex three dimensional anisotropic architectures made of the combination of different colloidal particles with LC GO which is rare in colloidal domain.[169, 215]

However, the anisotropic nature of the three dimensional complex architectures to some extent negatively impact on the ultimate performance for practical supercapacitor devices. This characteristic, although not really detrimental in

microsupercapacitor devices where thin films are used, essentially means that the final properties of these materials are directionally dependant. Therefore, this inherent feature limits identical electrical and electrochemical properties in all directions. Thus the key to engineer architectures with superior performance lies in the combination of the LC route, as an effective way to impart self-assembly and order, with another method to deliberately design isotropic architectures to boost the final performance and attain the ultimate capacitance.

The architectural design and engineering of these ternary systems helped us create unique hierarchical assemblies with ultra-high capacitance of 2074 Fg^{-1}. As-prepared LCs together with multi-walled carbon nanotubes (MWCNTs) and nickel nitrate hexahydrate, upon spray pyrolysis resulted in the simultaneous reduction of graphene oxide while preserving the order and obtaining large-scale, self-assembled isotropic, globular ternary architectures. Therefore, we suggest spray pyrolysis of liquid crystalline based dispersions hold the key to engineer advanced architectures which can be used to charter a new way forward in this field.

6.2 Results and discussion

6.2.1 Formation of liquid crystalline dispersions

The amphiphilicity of GO and the self-assembly properties, [26, 216-218] more pronounced in the case of ultra-large GO sheets, [168, 169, 217, 219, 220] have been utilized to prepare liquid crystalline dispersions of GO in both water, [168, 170, 212, 221] and organic solvents. [169] Ultra large GO sheets exhibit more hydrophobicity compared to their smaller cousins resulting in easier hydrophobic interactions between GO sheets and hydrophobic carbon based materials such as CNTs. [26, 168, 216] Therefore, the use of LC GO dispersions for ordering enables the formation of novel self-assembled complex 3D architectures based on amphiphilic interactions.[170, 212, 217, 220] However, the key element in employing this technological breakthrough is to achieve stable colloidal systems while maintaining the desired level of liquid crystallinity in the system. Nevertheless, achieving stable colloidal systems is not possible in the case of metal oxide or pristine CNTs unless excessive amount of surfactants are used which, in turn deteriorates the final electrochemical performance.

To this end, we added hydrated metal nitrates and functionalized CNTs as the precursors of choice to ultra large GO dispersions as a facile route to achieve GO-based ternary LC dispersions. The capability of metal nitrates to readily dissolve in aqueous medium presents us with the possibility of easily mixing them with aqueous LC dispersions of GO without compromising the liquid crystalline properties as evidenced from the birefrigance behavior of the dispersions presented in the polarized optical micrographs (Figure 6.2) before and after adding CNTs and metal nitrates to the system. From polarized optical micrographs (POM) in figures 6.2a and

6.2c, it is apparent that the addition of CNTs and metal nitrates does not disturb the liquid crystallinity of the GO dispersion.

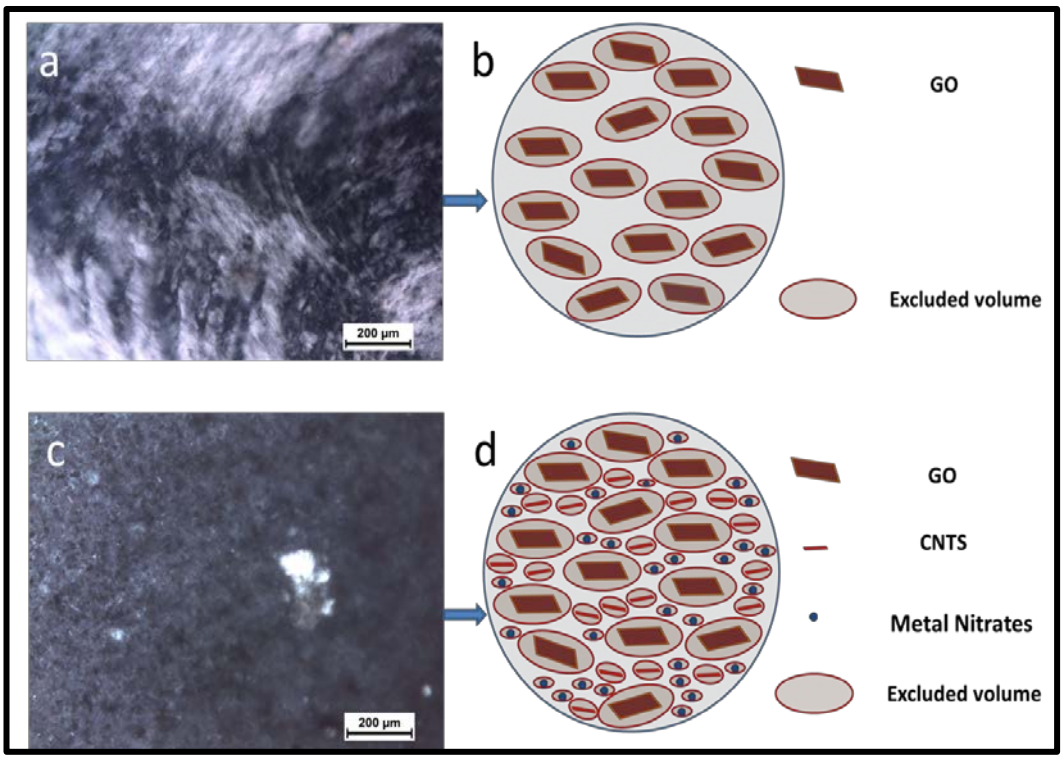

Figure 6.2: POM micrographs and proposed model for the evolution of LC phase in GO dispersions containing CNTs and metal nitrates. **(a)** POM micrograph of as prepared LC GO showing birefringence typical of liquid crystals. **(b)** Schematic showing the formation of LC in GO dispersions, **(c)** POM micrograph of as prepared dispersions containing GO, CNTs, and metal nitrates GO showing birefringence typical of liquid crystals. **(d)** Schematic showing the spontaneous formation of nematic liquid crystalline phase at ternary systems, the parallel arrangement of anisotropic sheets competitively limits the large excluded volume of small components such as CNTs and metal nitrate clusters and promotes nematic phase formation.

In a colloidal suspension containing different components with significantly different sizes, the bigger components (ultra large GO sheets in our case) generate excluded volume for smaller components. This, in turn, gives rise to entropic rearrangement of sheets to form long range ordering resembling liquid crystals. The presence of ultra-large sheets, therefore, competitively limits the large excluded

volume of small components such as CNTs and metal nitrate clusters and promotes nematic phase formation (Figure 6.2d). Based on the fundamental insight provided by Onsager's theoretical speculations, nematic LC formation is entropy-driven.[222] The isotropic-nematic transition originates from a petition between orientational entropy and positional entropy. Above the critical concentration limit predicted in our previous reports,[168, 214] the sheets will be oriented parallel to each other minimizing the volume excluded from the center-of-mass of the approaching sheet and maximizing the packing entropy favoring nematic ordering (Figures 6.2b and 6.2c). Therefore, although parallel arrangement of anisotropic sheets leads to a decrease in orientational entropy, it is the increase in positional entropy that governs the whole process of nematic LC formation.

The above mentioned arrangement gives us the directionality and orientational ordering which can aid in the organization of other components in the system at both molecular and macroscopic level (Figure 6.2d). This offers us a dynamic functional soft material which possesses high surface area 150 m^2g^{-1}, hierarchical level ordering (from molecular to super molecular and macroscopic level) and mobility. By maximizing the interaction energy and minimizing the excluded volume, all levels of organization (microscopic to macroscopic) are therefore attainable. The sudden exposure of this complex structure to heat in a fraction of a second typical in spray pyrolysis method, results in the spontaneous and simultaneous reduction of GO to rGO, and formation and growth of metal oxides trapped on the surface of GO.[28] Furthermore, as the precursor solution exhibits LC behaviour, the preservation of molecular level ordering is guaranteed in the spray-pyrolyzed dispersion.

6.2.2 Proposed model for the evolution of nickel oxide particles on the surface of GO sheets from nickel nitrate clusters.

As the metal nitrate particles are essentially clusters of molecules attached together in the size of less than 3 nm, in order to make them visible, selected areas on the surface were irradiated with electron beams and locally heated to simulate the growth conditions experienced during spray pyrolysis and accelerate nucleation and growth of particles into metal oxide particles. The transmission electron microscopy micrograph (TEM) presented in figure 6.3a show the complete coverage of the whole surface of graphene oxide sheets with metal nitrate clusters. Electron beam irradiation promoted the attachment and growth of these pre-nucleation clusters (Figure 6.3b). Upon even very mild irradiation conditions, typical of HRTEM, the formation of amorphous primary particles from the unstable initial precursor occurs with a monodispersed size distribution of around 2-3 nm (Figure 6.3a and b).

The formation of these primary particles can be explained by Ostwald step rule which states that in the very first step of nucleation and growth the formation of phases that are structurally more similar to the initial phase precedes the formation of thermodynamically more stable phases. Continuing the irradiation, these primary particles become denser and grow more to achieve a pre-nucleation cluster size in the range of 5-6 nm as shown in figure 6.3c. In the classical view, the nucleation occurs by stochastic process of dynamic growth and disintegration.[223] Here the crystallization occurs from a transient amorphous phase. Such behaviour has also been reported for the nucleation and growth of other transition metal oxide particles starting from hydrated ions of the transition metals; iron, chromium, uranium, molybdenum, and tungsten.[223, 224]Lattice fringes with d-spacing corresponding to (2 0 0) of NiO were observed in figure 6.3d after further irradiation. Therefore, as we had

predicted before,[28] the nucleation and growth of particles predominantly occurs on the surface of GO sheets and the matrix of graphene sheets and the very short amount of exposure to heat (less than 0.2-0.3 s during the spray pyrolysis) prevents further excessive coagulation and coalescence of particles into larger particles after the initial growth stage.

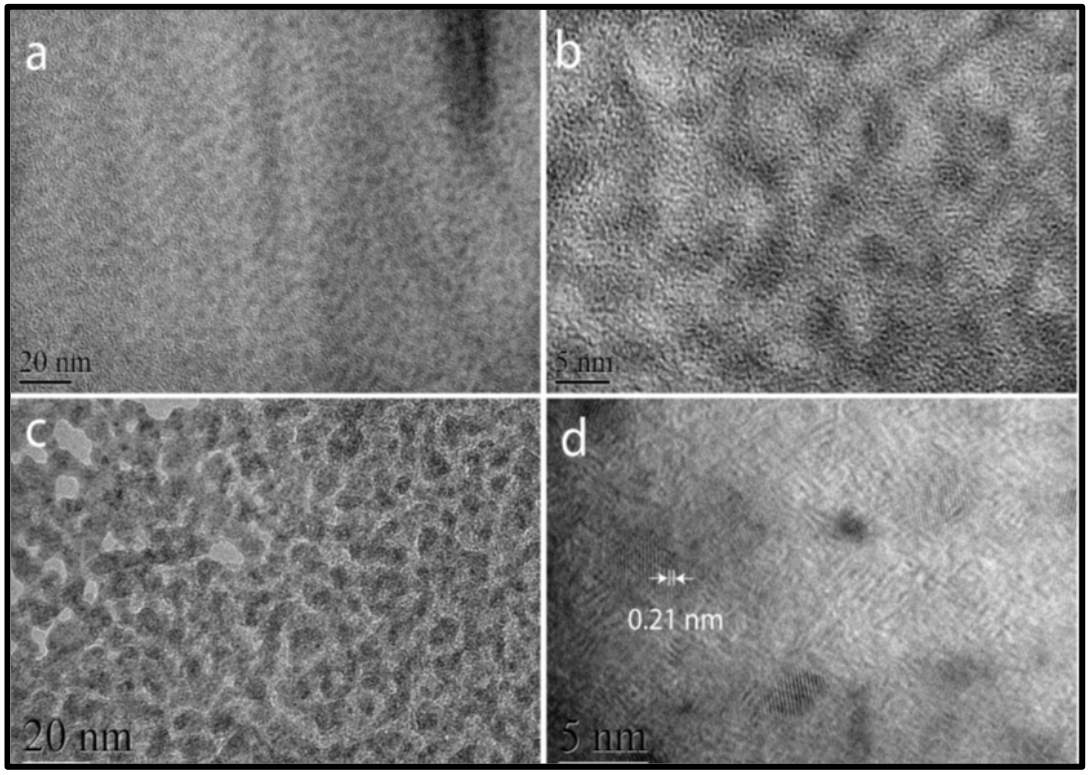

Figure 6.3: Proposed model for the evolution of nickel oxide particles on the surface of GO sheets from nickel nitrate clusters. **(a)** In the very initial stage and extremely short irradiation time, nickel nitrate clusters are in the range of 3 nm. **(b, c)** upon irradiation the clusters grow into amorphous particles in the range of 5 nm. **(d)** Increasing the irradiation time, nickel nitrate particles convert to nickel oxide particles. The crystallization into nickel oxide particles is evidenced by lattice fringes and d spacing in the order of 0.21 nm corresponding to (2 0 0) of nickel oxide.

The suggested evolution model from figure 6.3 is confirmed by the Dark field and Bright field TEM images representative of rGO-Nickel oxide particles, obtained after spray pyrolysis (Figures 6.4a and b**,** respectively), which clearly show that the

whole surface of globular ensembles is covered entirely by nickel oxide particles (see also figure 6.4d). Individual ternary spheres are shown in figure 6.4 a and c. On closer examination, the surface is observed to be a very porous with MWCNTs embedded (figure 6.4 b) in the structure while the surface of GO is covered with metal oxide nanoparticles (figure 6.4 d).

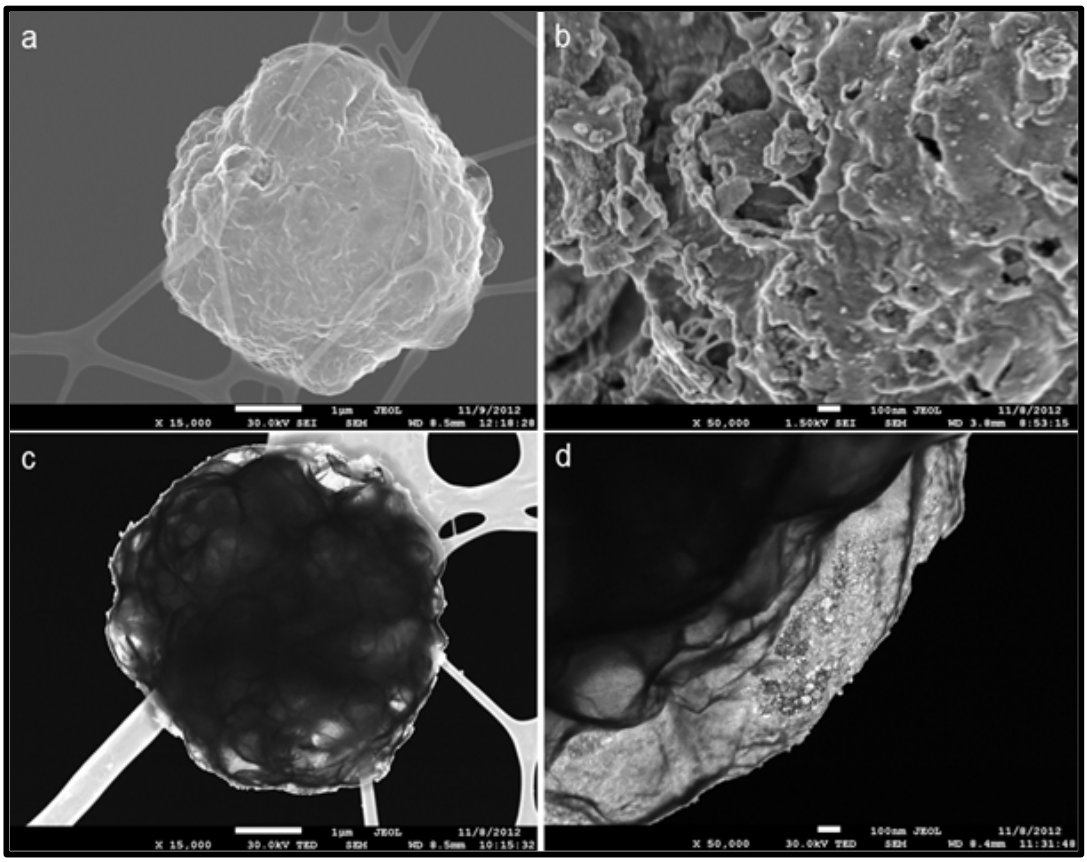

Figure 6.4: **(a)** and **(c)** Individual particle of the ternary spheres. **(b)** SEM image showing the surface of a single sphere of the ternary composite after spray pyrolysis. Note the irregular and rough surface due to the presence of MWCNTs. **(d)** NiO nanoparticles uniformly coated on the surface of rGO sheets encompassing the MWCNT's.

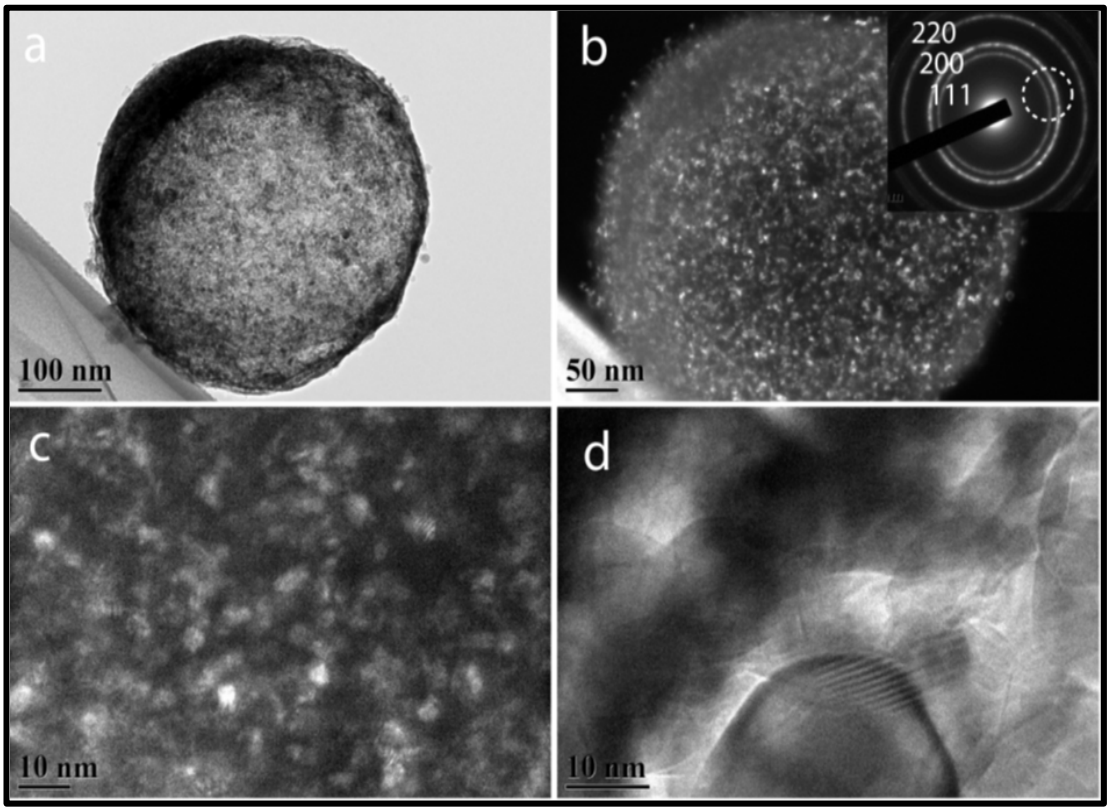

Figure 6.5: TEM micrographs of hollow spherical architectures illustrating the distribution of nickel oxide particles on the surface of graphene spheres. **(a)** Bright field TEM micrograph of the same sphere, **(b)** Dark field TEM micrograph of an individual hollow sphere using (111) and (200) diffraction sets. In contrast to **(a)**, dark field imaging enables us to verify the presence of nickel oxide particles on the surface with a better contrast. **(c, d)** High resolution TEM micrographs of nickel oxide particles imposed on top of each other through graphene sheets further verifying the coverage of the whole surface of graphene sheets by nickel oxide particles.

The fact that these architectures resemble hollow spherical architectures is beneficial in two regards. Firstly, the hollow architecture ensures the easy access of ions to the entire surface of nickel oxide covered graphene sheets. And secondly, the spherical shape guarantees the isotropic properties of the final architecture while the nanometre size of the metal oxide particles, as apparent from figure 6.5c and 6.5d allows effective distribution over the surface of the reduced graphene oxide sheets.

The arrangement of the constituent elements of the ternary composite prior to spray pyrolysis is shown in figures 6.6a and 6.6b. The hierarchical architecture of our as-prepared particles from micro-scale down to nano-scale shown in figures 6.6c and 6.5d enables the inter-and intra-connection of all functional components present in our system. The image in figure 6.6d clearly shows the distribution of monodispersed nanoparticles on the surface of one globular structure together with the protrusion of MWCNT's from the structure. These types of architectures which are free from excessive agglomeration play a key role to achieve extraordinary performance in energy storage systems, where the maximum utilization of the surface is of utmost importance. This also ensures that the whole surface in the system is accessible to electrolyte ions resulting in an extraordinary boost of performance in our system due to pseudocapacitance. However, CNTs are hardly visible on the surface of the particles, as they are mostly wrapped with graphene sheets as presented in TEM micrographs.

To visualize the CNTs entrapped between GO sheets in the final architecture, we smashed the particles and investigated their structure as shown in figure 6.6e. Individual CNTs protruding from within the structure walls are seen in figure 6.6f confirming the idea that CNTs are individually positioned within the walls. The presence of individual CNTs in this regard not only provides us with the possibility of utilizing the whole surface of CNTs for charge storage but also acts as bridging component which connects the individual graphene sheets uniformly covered by NiO nanoparticles. This results in a synergy among all components in our system and helps us achieve extraordinary electrochemical performance.

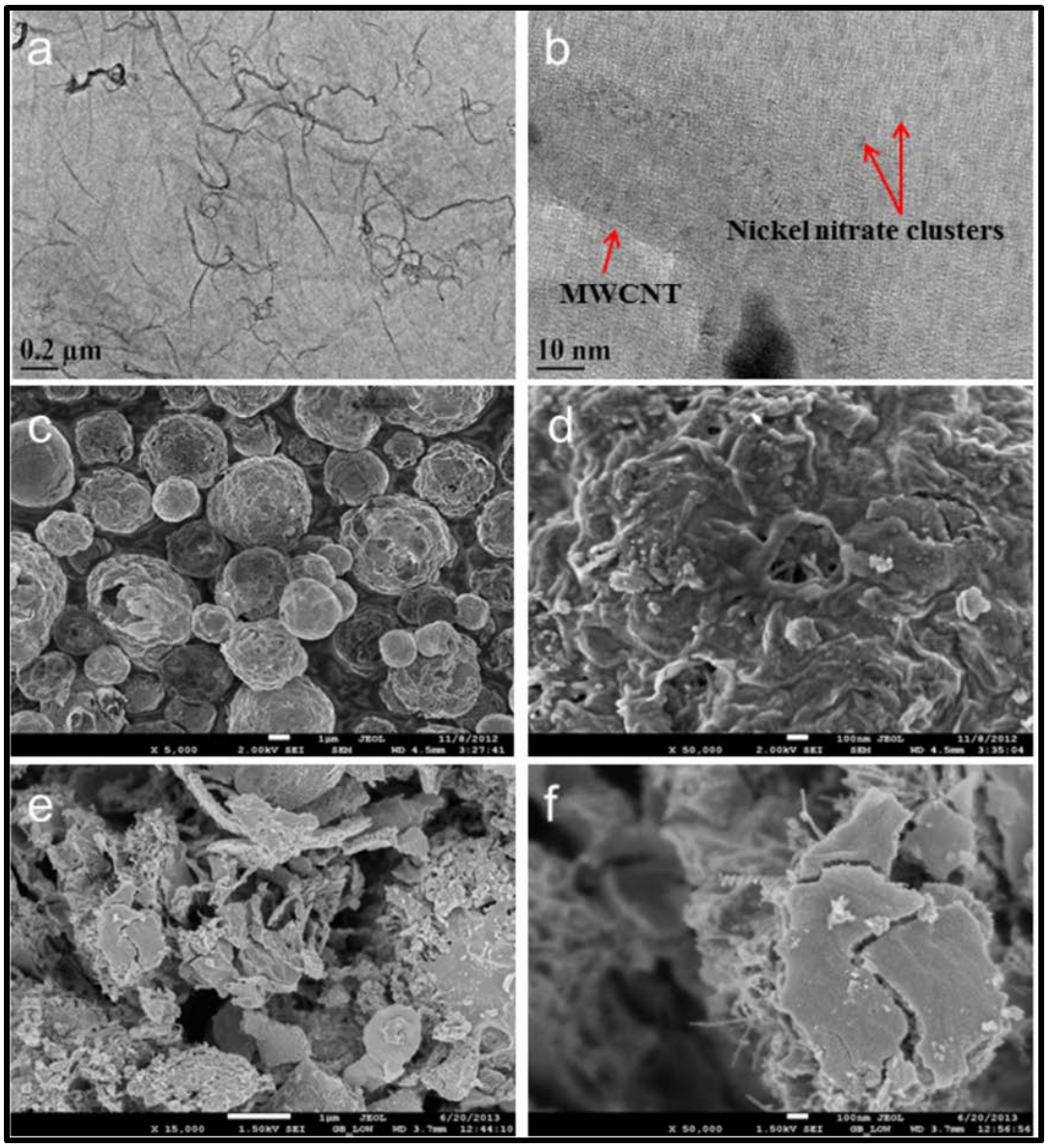

Figure 6.6: Electron microscopy micrographs of ternary architectures. **(a)** Low resolution TEM micrograph of the composite mixture showing arrangement of CNTs on graphene oxide sheets and **(b)** high resolution TEM micrograph showing the presence of nickel nitrate particles and individual CNTs on the surface of an individual graphene sheet prior to spray pyrolysis. **(c)** Distribution of ternary composite spheres obtained by spray pyrolysis and showing at **(d)** high magnification, presence of pores which allow for easy access of the MWCNT network within the structure **(e)** smashed particles showing distribution of constituent composite materials and (f) individual CNTs protruding from within the structure walls uniformly coated by NiO nanoparticles.

Electrochemical characterization

Figure 6.7a shows cyclic voltammograms for the constituent materials and the ternary composite illustrating the synergistic effects of the three materials when combined. Nickel oxide is already well known to offer high capacitance due to its pseudocapacitive properties. It is therefore not surprising to see that a larger current separation exists for the ternary architecture and binary MWCNT/NiO composite compared to MWCNT. Supplementary to that, the synergy that exists between MWCNTs and GO also contributes significantly to the overall capacitance of the ternary composite where GO acts as a surfactant for dispersing the CNTs. [26, 225]

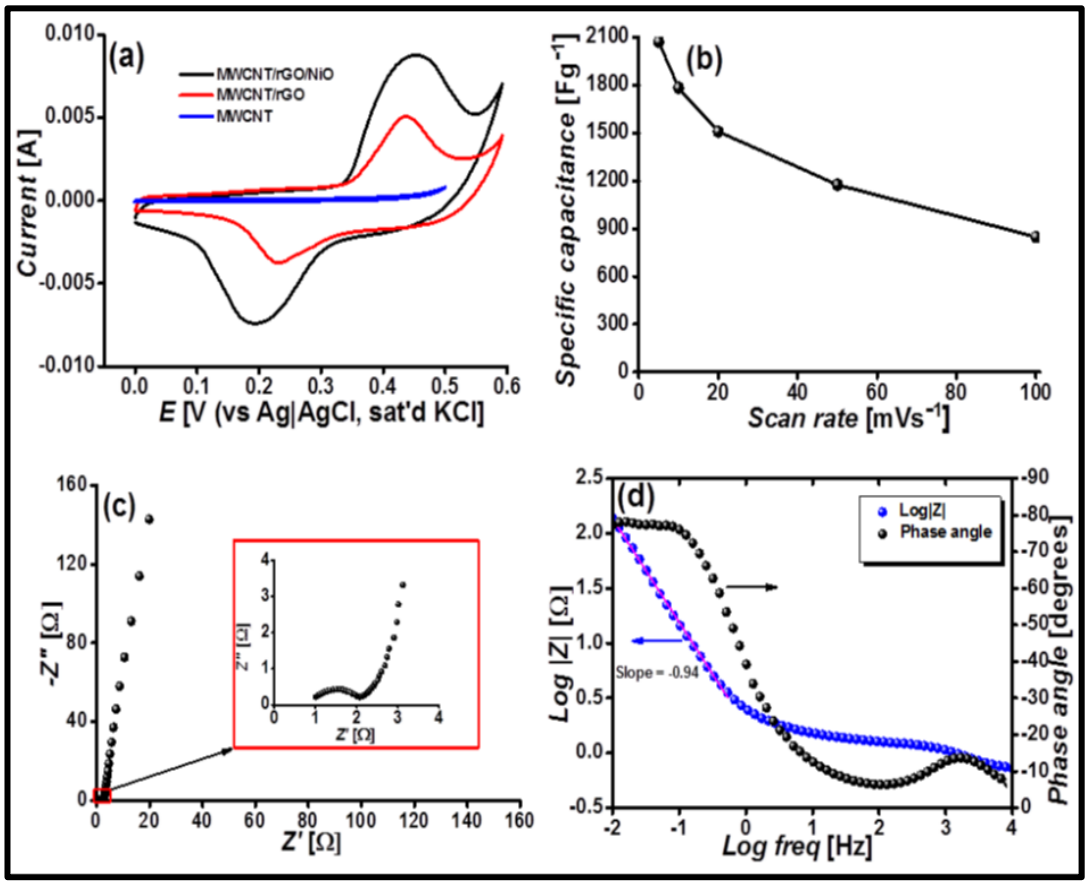

Figure 6.7: **(a)** Cyclic voltammograms showing synergistic effects of MWCNT's, rGO and NiO at 5 mV/s. **(b)** Effect of scan rate on cyclic voltammograms of the composite ternary electrode **(c,d)** Nyquist plot of the electrode **(e)** Bode plot of the electrode.

The large GO sheets in the precursor solution also enhance the electroactive surface area available for charge storage in the electric double layer (EDL) while the CNTs provide a conductive link between particles in the final composites. Furthermore, the combination of rGO and CNTs provides a good EDL support for the well-dispersed pseudocapacitive NiO nanoparticles. It is therefore obvious from the size and shape of the cyclic voltammograms obtained at low scan rate that the electrode materials exhibit typical pseudocapacitive behaviour combined with EDL characteristics. Distinct oxidation/reduction peaks between 0.45 V and 0.2 V in figure 6.7a, characteristic of NiO electrodes cycled in alkaline solution are attributed to the reaction described by equation 21. [28, 125, 208, 226]

$$NiO + OH^- \leftrightarrow NiOOH + e^- \quad (21)$$

As cycling was continued at different scan rates (in figure 6.8b**)** , these redox peaks shifted to more positive and negative potential with increase in scan rate due to the abundant surface area provided by the porous electrode structure and fast ionic/electronic diffusion rate during the Faradaic redox reaction.[125, 144]

From the same graph a relationship between specific capacitance and scan rate was plotted in figure 6.7b. We reported a maximum capacitance of 2074 Fg^{-1} for the ternary MWCNT/rGO/NiO active material which is higher than those reported elsewhere due to the unique organization of the constituent materials in the composite (See Table 6.1).

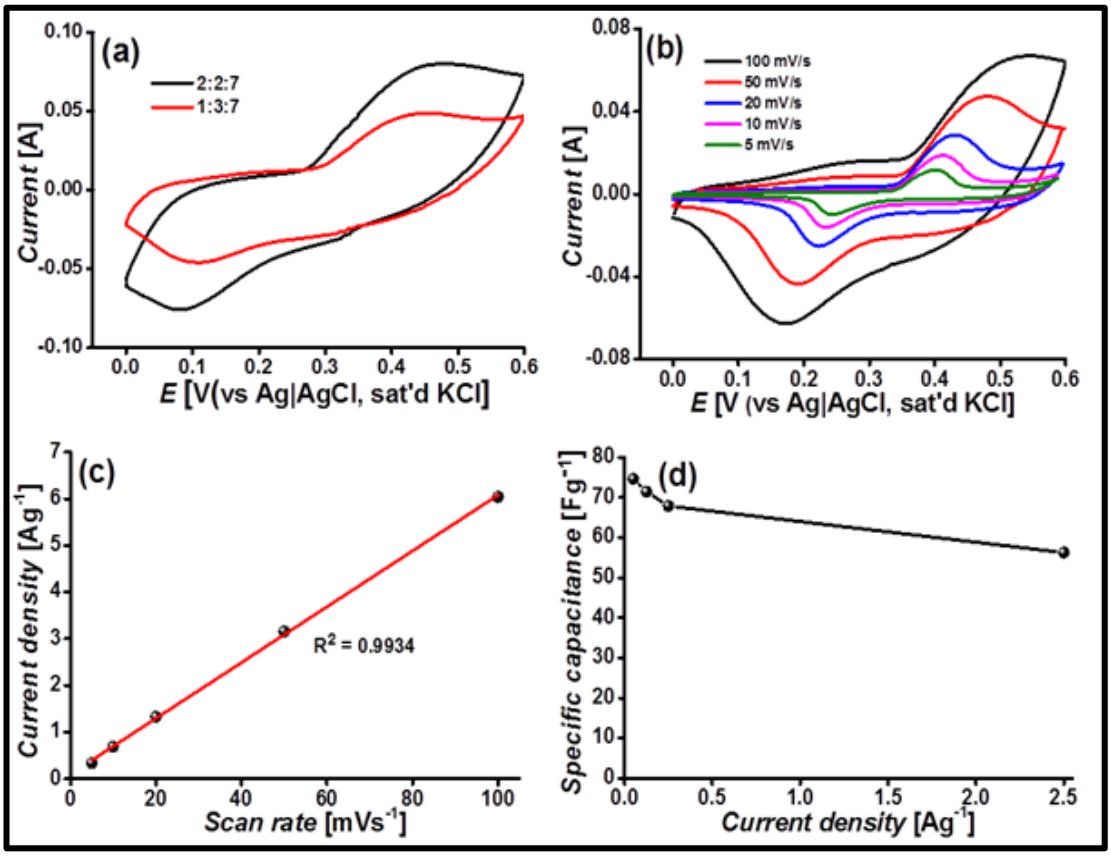

Figure 6.8: (a) Cyclic voltammograms of the MWCNT/rGO/NiO composite electrodes fabricated using different ratios of CNT, rGO, NiO in 1M NaOH at 100 mV/s **(b)** Effect of scan rate on cyclic voltammograms of the composite. **(c)** Relationship between current density and scan rate. **(d)** Effect of current density on specific capacitance calculated from CD.

Even at high scan rates, where a significant drop in specific capacitance is usually observed, our as prepared electrodes still boasts an exteremly high specific capacitance of 900 Fg^{-1}. This is a result of electrolyte ions only reaching the outer surface of the electrode at high scan rates, and a fraction of the total active area being accessible to actively contribute to the overall pseudocapacitance.[227] In our case, these outer surfaces are uniformly coated by NiO nanoparticles thereby facilitating Faradaic reactions to occur and consequently high specific capacitance. Nevertheless, at low scan rates, the bulk of the electrode material is utilised for charge storage. The inside walls which encompass MWCNTs act as inner active sites of the hollow

spheres are also coated with NiO nanoparticles and become accessible, contributing to the overall capacitance. Similarly, the surface of the smaller spheres contained in some of the large spheres creating a hierarchical structure are decorated with NiO nanoparticles and these surfaces are made available for charge storage through Faradaic reactions.

Table 6.1: Comparison of the MWCNT/rGO/NiO based composite electrodes with other ternary systems reported in literature. All values are measured using the three-electrode system.

Ternary composite	**Electrolyte**	**Specific capacitance [Fg^{-1}]**	**Reference**
MWCNT/rGO/NiO	1 M NaOH	2074 (5 mVs^{-1})	This work
graphene–CNT/$Ni(OH)_2$	6 M KOH	1352 (5 mVs^{-1})	[34]
Graphene/MnO_2/CNT	1 M Na2SO4	372 (10 mVs^{-1})	[7]
rGO/MO/PANI	1M H_2SO_4	553 (1 mVs^{-1})	[35]
GN/PANI/CNT	1M HCl	569 (1 Ag^{-1})	[36]
CF-ACNT/MnO_2/PEDOT	1M H_2SO_4	481 (5 mVs^{-1})	[37]
MWCNT-PSS/PPy:MnO_2	0.5 M Na_2SO_4	268 (5 mVs^{-1})	[38]
graphene/MnO_2/PEDOT:PSS	0.5 M Na_2SO_4	380 (5 mVs^{-1})	[39]
Graphene/SnO_2/polypyrrole	1M H_2SO_4	616 (1 mVs^{-1})	[40]

To further understand these reactions occurring at the electrode/electrolyte interface, electrochemical impedance spectroscopy (EIS) was used to study the electrodes over a frequency range from 10 KHz to 10 mHz. Supercapacitors generally behave as resistors at high frequency and pure capacitors at low frequencies where a near vertical Nyquist plot is observed. At high frequency, only a small amount of the electrode surface area is utilized as a capacitor while at low frequency most of the pore surface is utilized resulting in maximum capacitance.[144] Figure 6.7c represents a Nyquist plot of the MWCNT/rGO/NiO electrode in 1 M NaOH. At high frequencies, a semicircle, characteristic of resistive behaviour and the highly porous nature of the electrode was detected. An expanded view of this region (inset) shows the intersection of the impedance plot with the real axis which narrates to the bulk solution resistance (R_S) of 1Ω. This low bulk solution resistance is typical of aqueous electrolytes as they are more conductive compared to organic electrolytes and the low charge transfer resistance (R_{CT}) of 1.5 Ω is attributed to the conductive nature of the functionalised CNTs and rGO present in the final composition.

The transition from high to low frequency where the capacitor behaves as a resistance-capacitance (RC) transmission line can be clearly recognized in the middle frequency region in the Nyquist plot. [228] In this region, a Warburg-type line is almost non-existent due to the shortening of the diffusion path brought about by the combination of rGO and CNTs especially due to the ratio used in this work.[225] The Nyquist plot becomes more vertical at low frequency consequently influencing the phase angle that increases gradually towards -90° expected for ideal supercapacitors. In our case, a phase angle of -80° and a slope of -0.95 were observed on the Bode plot (Figure 6.7d) indicating pseudocapacitive behaviour in the low frequency region where ideal capacitors normally exhibit a slope of -1.[229] From the Bode plot, a

gradual increase in capacitance from 100 Hz can be seen with half of the total capacitance being reached at ca. 10 Hz representing good response from the supercapacitor electrode.

6.2.3 Two electrode asymmetric test results

To assess the feasibility of using the ternary composites in practical supercapacitors, we assembled an asymmetric supercapacitor in an ECC-STD Electrochemical Cell (El-Cell). Activated carbon (AC) was employed as the negative electrode while the ternary composite electrode was used as a cathode. The choice of activated carbon as an anode material was due to its typical EDLC behaviour as evidenced by the absence of redox peaks in the cyclic voltammograms obtained for the material in 1M NaOH as shown in figure 6.9a. On the other hand, the CV of the cathode electrode shows distinctive peaks reflecting the pseudocapacitive nature of the material as discussed earlier. A combination of the largely pseudocapacitive ternary system electrode and AC resulted in almost rectangular CV's expected for ideal capacitors even at a high scan rate of 100 mVs^{-1}. Additionally, the contribution of the AC to this remarkable stability cannot be overlooked as proven by a meagre 9.6% decrease in capacitance of the asymmetric device as scan rate increased (see figure 6.9b). This slight decrease in capacitance as scan rate was increased while maintaining the rectangular shape indicates desirable fast charge/discharge property for power devices. [153] This can be mainly attributed to the existence of larger pores especially those existing among adjacent spheres and throughout the whole cathode electrode structure and the isotropic nature of the materials as observed in the SEM images in figure 6.6c.[144]

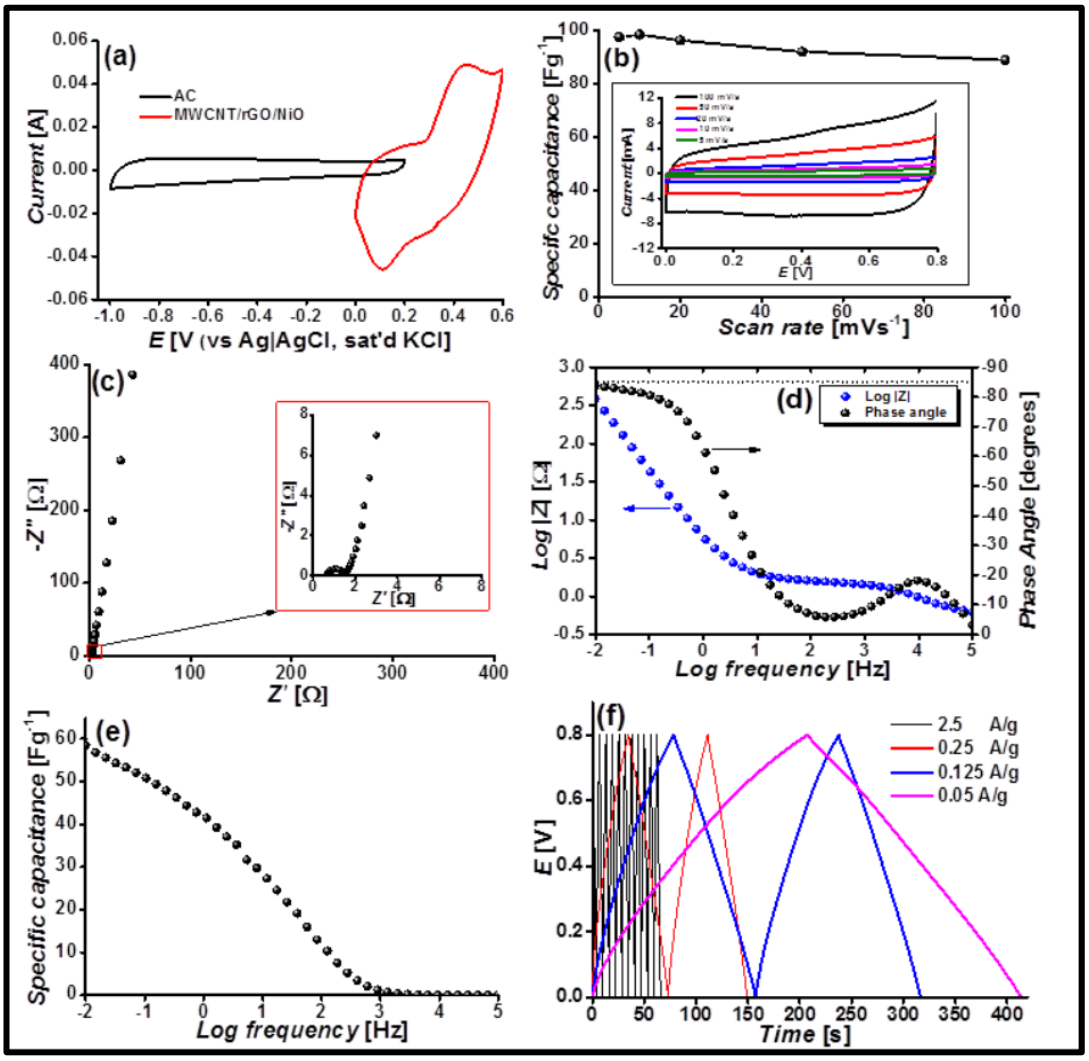

Figure 6.9: (a) Comparative CV's for the anode and cathode materials cycled in 1M NaOH at 100 mVs^{-1}. **(b)** Effect of scan rate on the overall capacitance of the asymmetric device. **(c)** Nyquist plot for the asymmetric supercapacitor device obtained at open circuit potential (OCV) **(d)** Bode plot showing maximum phase angle and log |Z| values. **(e)** Variation of specific capacitance as a function of frequency. **(f)** Charge discharge profiles at different current densities.

The overall capacitances were calculated for CV, CD, EIS and using equations 16, 18 and 23 respectively to yield maximum specific capacitances of, 60, 75 and 97 Fg^{-1}. The overall capacitances reported here for CV and CD are higher than those reported by Cheng et al.(70 Fg^{-1}) for ternary structures made of graphene/MnO_2/CNTs similar to our work.[167] Upon further analysis, the

experimental data which shows dependence of current on scan rate is seen (Figure 6.8c**)** to follow a linear response suggesting good power capability and reversibility of the device.[230] This is in agreement with the following equation where current is directly proportional to the scan rate.

$$I = \frac{dq}{dt} = C\frac{dE}{dt} = Cv \qquad (22)$$

Where *I*, is the current on the scan rate, dE/dt =v, *q* is the charge stored and *C* is the capacitance. These findings are further validated by the capacitance retention of 75.63% from 0.05 to 2.5 Ag^{-1} shown in figure 6.8d.

With the excellent interconnectivity between the constituent materials in the final electrode material, ions reach the whole porosity of the active material allowing fast charge transfer and shortening of the diffusion path to the active sites on the electrode. For that reason, a small semicircle indicating low charge transfer resistance was observed in the high frequency region on a Nyquist plot in figure 6.9c while a near vertical line was detected at lower frequencies. Again, small R_s and R_{CT} values derived from the intersection of the Nyquist plot and the x-axis and the radius of the semicircle respectively were detected inferring low ESR (equivalent series resistance) for the asymmetric device which in turn has a bearing on the response time of the device. A gradual increase in capacitance from 100 Hz can therefore be observed with half of the total capacitance being reached at ca. 10 Hz. From the Nyquist plot, a Bode plot (Figure 6.9d) was plotted to show the maximum phase angle of -85˚ which is close to -90˚ for an ideal supercapacitor. We also calculated the specific capacitance using EIS for all frequencies. A plot of specific capacitance versus log of frequency in figure 6.10e shows a maximum capacitance of 60 Fg^{-1} calculated from using equation 3.

$$C_s = -\frac{1}{2\pi f_o Z''} \qquad (23)$$

After calculating the capacitance using different methods, we compared these values to assess their validity. The overall capacitance values calculated using all three techniques are seen to be within the same range. It can however, be noted that the value obtained from EIS (60 Fg^{-1}) is lower than those obtained from CV (97 Fg^{-1}) and CD (75 Fg^{-1}) because alternating current penetrates into the bulk of the electrode material with some hindrance. Another important parameter, the energy density of the device was calculated to achieve a maximum energy density of 23 $Whkg^{-1}$ using formula reported in literature. [153] Figure 6.9f shows charge/discharge profiles obtained at different current densities. From the plot, the profile exhibits almost linear charging and discharging slopes which are symmetrical implying good capacitive behaviour and high coulombic efficiency. Additionally the plot was used to calculate a coulombic efficiency of 99.51% using the equation:

$$\eta(\%) = \frac{t_d}{t_c} \times 100 \qquad (24)$$

Where t_d is the discharge time in seconds and t_c is the charging time.

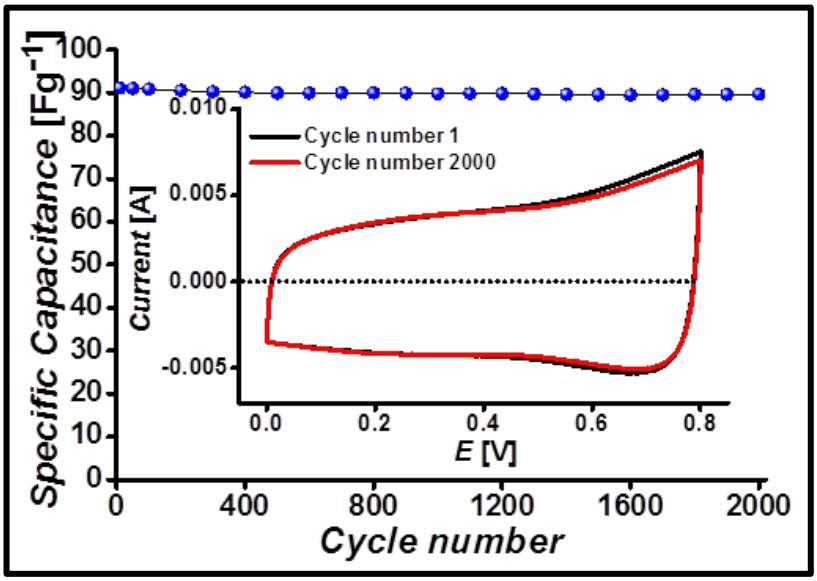

Figure 6.10: Cycle life of the asymmetric device in 1M NaOH tested at 100 mVs^{-1} showing stability of the device for 2000 cycles. Inset shows cyclic voltammograms of the first and last cycles.

Because the stability of a supercapacitor is of utmost importance as it determines its practicality, we cycled the asymmetric device for 2000 cycles at 100 mVs^{-1} and noted the change in capacitance at the end of experiment (Figure 6.10). Interestingly, we observed capacitance retention of 96.78% which is ideal for practical supercapacitors. We attribute this remarkable stability to the carbonaceous material in both the anode and cathode since EDLCs possess better stability than pseudocapacitors.

6.3 Summary

In this chapter, we employed a novel two-step synthesis approach to obtain high performance isotropic ternary architectures via a facile spray pyrolysis of graphene oxide based liquid crystals. The spray pyrolysis method enabled us to preserve the induced self-assembled LC state consequently resulting in an ordered isotropic architecture with superior inherent electrochemical properties. These electrodes were tested with the three electrode half-cell in 1M NaOH yielding a high specific capacitance of 2074 Fg^{-1}. By efficiently exploiting the synergistic effects of the constituent materials we fabricated supercapacitor electrodes ideal for asymmetric devices using activated carbon as an anode material. A maximum capacitance of 97 Fg^{-1} ,remarkable cycle life (96.78% capacitance retention over 2000 cycles) and energy density of 23 $Whkg^{-1}$ for the asymmetric supercapacitor were achieved due to the porous network, isotropic and pseudocapacitive nature of the composites which make them possible candidates for battery electrodes.

7 CONCLUSIONS AND RECOMMENDATIONS

7.1 Conclusions

The performance and practicality of supercapacitor electrodes hinges on two points. The first is the engineering of high performance materials to produce cost effective composites without compromising electrochemical performance. The second is the improvement of fabrication methods to be able to produce homogenous mixtures of electrode materials in bulk while maintaining the effective interactions between materials at nano level. The work done in this thesis was to improve the performance of already existing combinations of metal oxides and graphene oxide by introducing a scalable and cost effective spray pyrolysis method to produce a range of materials. The fabrication method allowed the synthesis of high performance graphene oxide and reduced graphene oxide in bulk while preserving the large structure of the GO/rGO sheets.

This work has therefore been dedicated to enhancing the interactions between GO/rGO and the pseudocapacitive metal oxides to improve the Faradaic processes across the interface so as to increase the electrochemical capacitance of the composites. These composites were successfully implemented in practical supercapacitor devices.

The results presented in this thesis show the effect of adding different metal oxide nanoparticles on the overall performance of the composite together with the different morphologies dictated by the fabrication method. The first metal oxide to be studied was manganese oxide due to its well documented high specific capacitance. Instead of producing single phase MnO_x, a mixture of oxides Mn_2O_3 and Mn_3O_4 anchored on rGO sheets after spray pyrolysis were obtained. We concluded that due

to the presence of different oxidation states of the manganese, urchin-like morphologies mixed with well dispersed MnO_x nanoparticles on the surface of the rGO were produced. By mixing GO with manganese nitrate, the composite resulted in MnO_x nanoparticles being anchored on the rGO after spray pyrolysis. This arrangement resulted in enhanced redox activity of the rGO-MnO_x composite and improved specific capacitance for the otherwise poorly conducting Mn_2O_3 and Mn_3O_4. For the first time, we reported the reduction of GO using spray pyrolysis method in less than 1s at 600˚C. The resultant 3D urchin-like structure contributed to the high specific capacitance of 425 Fg^{-1} and 133 Fg^{-1} in three-electrode and two-electrode asymmetric set ups. Also a high surface area of (139 m^2g^{-1}) was obtained due to the intertwining of nanoneedles creating a well-connected structure on the electrode surface. From this work, it is evident that a mixture of phases in composites is not detrimental to the performance of supercapacitor electrodes but can be exploited to achieve varied morphologies with excellent properties.

In the case of cobalt oxide and nickel oxide composites mixed with GO, distinct micro spheres of GO-MO composites were obtained after spray pyrolysis. Although the spray pyrolysis method is shown to produce uniform dispersions of these metal oxide nanoparticles, it is vital that ideal mass ratios of the individual materials be determined prior to electrode fabrication. We therefore concluded that the ratio of GO: MO affects the performance of supercapacitor electrodes. In this thesis, a ratio of 2:7 for the GO: MO is reported to be ideal as it gives the best performance with large specific capacitances of 687 and 656 Fg^{-1} for the rGO-Co_3O_4 and rGO-NiO respectively. Higher amounts of GO means a lower mass loading of pseudocapacitive metal oxides resulting in lower specific capacitances.

In alkaline solution, the redox activity of the NiO and Co_3O_4 gives rise to reversible oxidation peaks and consequently higher specific capacitance. Also, the rGO being a thin 1-D carbon nanostructure contributes positively to the charge transport and long cycle life of the supercapacitor electrode. Due to this, rGO's high conductivity coupled with the nanoscale dimension of the metal oxide are beneficial to the overall conductivity of the composites thereby decreasing the length of the diffusion path and improving the rate capability of the electrodes.

The observations from these two experiments mentioned above inspired the researcher to develop ternary structures using MWCNTs, NiO and rGO. In this work, we used the same mass ratio between NiO and rGO and introduced MWCNTs to the system to capitalise on the synergy between the three materials. This arrangement, due to the use of LC-GO in the preliminary mixing of the components makes it even more attractive by "locking" in constituent materials. Specifically, liquid crystalline graphene oxide provides a route for the efficient self-assembly of the constituent materials thereby anchoring the MWCNT and NiO onto the EDLC support. Upon spray pyrolysis this self-assembly results in very porous 3D architectures where MWCNTs act as conducting wires within the structures while the NiO nanoparticles contribute to the pseudocapacitive nature of the electrode. The main conclusion from this work was that 3D hierarchical architectures combining microstructures decorated by nanostructured NiO particles distributed uniformly on the surface of the rGO covered microstructures can produce high performance electrodes.

An exceptional specific capacitance of 2074 Fg^{-1}, which is close to the theoretical specific capacitance of NiO was therefore achieved. These same electrodes also proved to be suitable for an asymmetric supercapacitor device where an increased electrochemical window directly impacted the energy density.

7.2 Recommendations

Future work on supercapacitor electrodes should be focused on improving the interaction between individual components of the composites to produce cheap electrodes. The development of asymmetric devices is undoubtedly the best way to harness the individual benefits of battery and supercapacitor electrodes in a hybrid system. This set up results in an increased energy density and remarkable stability stemming from the EDLC behaviour of the supercapacitor electrode. To achieve the ultimate performance from such systems, it is important to tailor-make the morphology of the composites so that electrolyte ions can be effectively stored on the electrode surface. The dynamics of this system can therefore be illuminated by the careful study of impedance data collected from different electrolytes. In such a study, the expansion of the electrodes,porosity and changes in morphology as cycling continues can then be monitored by the different equivalent circuits generated from fitting impedance data.

There are limited reports in literature where ternary composite electrodes have been used for supercapacitor development. More studies should therefore be directed in this area in order to fully exploit the characteristics of the constituent materials. A host of cheap metal oxides such as Fe_2O_3 and VO_5 can be incorporated into the same systems reported in this thesis to produce robust supercapacitor electrodes. In order to improve the performance of these materials, different morphologies of the metal oxides can be fabricated by varying the spraying conditions such as temperature, altering the nozzle size, length of spray column and spraying in inert atmospheres.

.

8 REFERENCES

1. J. Schindall, *Spectrum, IEEE*, 2007, 44, 42-46.
2. *USA Pat.*, 1957.
3. B. E. Conway, *Electrochemical Supercapacitor: Scientific Fundamentals and Technological Application* New York:Kluwer Academic/Plenum Publisher, 1999.
4. M. Winter and R. J. Brodd, *Chemical Reviews*, 2004, 104, 4245-4270.
5. H. Ibrahim, A. Ilinca and J. Perron, *Renewable and Sustainable Energy Reviews*, 2008, 12, 1221-1250.
6. E. Frackowiak and F. Béguin, *Carbon*, 2001, 39, 937-950.
7. R. Kötz and M. Carlen, *Electrochimica Acta*, 2000, 45, 2483-2498.
8. L. L. Zhang and X. S. Zhao, *Chemical Society Reviews*, 2009, 38, 2520-2531.
9. B. E. Conway, V. Birss and J. Wojtowicz, *Journal of Power Sources*, 1997, 66, 1-14.
10. D. C. Grahame, *Journal of the American Chemical Society*, 1958, 80, 4201-4210.
11. X.-L. Wu and A.-W. Xu, *Journal of Materials Chemistry A*, 2014, 2, 4852-4864.
12. A. Burke, *Journal of Power Sources*, 2000, 91, 37-50.
13. A. G. Pandolfo and A. F. Hollenkamp, *Journal of Power Sources*, 2006, 157, 11-27.
14. G. Wang, L. Zhang and J. Zhang, *Chemical Society Reviews*, 2012, 41, 797-828.
15. A. S. Raut, C. B. Parker and J. T. Glass, *Journal of Materials Research*, 2010, 25, 1500-1506.
16. T. Christen and M. W. Carlen, *Journal of Power Sources*, 2000, 91, 210-216.
17. T. Christen and C. Ohler, *Journal of Power Sources*, 2002, 110, 107-116.
18. N. A. Choudhury, S. Sampath and A. K. Shukla, *Energy & Environmental Science*, 2009, 2, 55-67.
19. M. Zhi, C. Xiang, J. Li, M. Li and N. Wu, *Nanoscale*, 2013, 5, 72-88.
20. P. Simon and Y. Gogotsi, *Nat Mater*, 2008, 7, 845-854.
21. A. S. Arico, P. Bruce, B. Scrosati, J.-M. Tarascon and W. van Schalkwijk, *Nature Materials*, 2005, 4, 366-377.
22. J. R. Miller and P. Simon, *Science*, 2008, 321, 651-652.
23. Y. Fang, B. Luo, Y. Jia, X. Li, B. Wang, Q. Song, F. Kang and L. Zhi, *Advanced Materials*, 2012, 24, 6348-6355.
24. M. Armand and J.-M. Tarascon, *Nature*, 2008, 451, 652-657.
25. Y. Gogotsi and P. Simon, *Science*, 2011, 334, 917-918.
26. S. H. Aboutalebi, A. T. Chidembo, M. Salari, K. Konstantinov, D. Wexler, H. K. Liu and S. X. Dou, *Energy & Environmental Science*, 2011, 4, 1855-1865.
27. S. Chen, J. Zhu, X. Wu, Q. Han and X. Wang, *ACS Nano*, 2010, 4, 2822-2830.
28. A. Chidembo, S. H. Aboutalebi, K. Konstantinov, M. Salari, B. Winton, S. A. Yamini, I. P. Nevirkovets and H. K. Liu, *Energy & Environmental Science*, 2012, 5, 5236-5240.
29. Y. Zhu, S. Murali, M. D. Stoller, K. J. Ganesh, W. Cai, P. J. Ferreira, A. Pirkle, R. M. Wallace, K. A. Cychosz, M. Thommes, D. Su, E. A. Stach and R. S. Ruoff, *Science*, 2011, 332, 1537-1541.

30. A. T. Chidembo, K. I. Ozoemena, B. O. Agboola, V. Gupta, G. G. Wildgoose and R. G. Compton, *Energy & Environmental Science*, 2010, 3, 228-236.
31. M. F. El-Kady, V. Strong, S. Dubin and R. B. Kaner, *Science*, 2012, 335, 1326-1330.
32. Y. Chen, X. Zhang, D. Zhang, P. Yu and Y. Ma, *Carbon*, 2011, 49, 573-580.
33. A. L. M. Reddy, S. R. Gowda, M. M. Shaijumon and P. M. Ajayan, *Advanced Materials*, 2012, 24, 5045-5064.
34. C. Tan, K. Tan, Y. Ong, A. Mohamed, S. Zein and S. Tan, *Environ Chem Lett*, 2012, 10, 265-273.
35. Y. Fan, Q. Zhang, Q. Xiao, X. Wang and K. Huang, *Carbon*, 2013, 59, 264-269.
36. K. Fu, O. Yildiz, H. Bhanushali, Y. Wang, K. Stano, L. Xue, X. Zhang and P. D. Bradford, *Advanced Materials*, 2013, 25, 5109-5114.
37. Y. Wu, Y. Wei, J. Wang, K. Jiang and S. Fan, *Nano Letters*, 2013, 13, 818-823.
38. K. Wang, Q. Meng, Y. Zhang, Z. Wei and M. Miao, *Advanced Materials*, 2013, 25, 1494-1498.
39. J. Zhang, X. Wang, J. Ma, S. Liu and X. Yi, *Electrochimica Acta*, 2013, 104, 110-116.
40. L. Chen, K. Xia, L. Huang, L. Li, L. Pei and S. Fei, *International Journal of Hydrogen Energy*, 2013, 38, 3297-3303.
41. W. Y. Wong, W. R. W. Daud, A. B. Mohamad, A. A. H. Kadhum, E. H. Majlan and K. S. Loh, *Diamond and Related Materials*, 2012, 22, 12-22.
42. V. Neves, E. Heister, S. Costa, C. Tîlmaciu, E. Flahaut, B. Soula, H. M. Coley, J. McFadden and S. R. P. Silva, *Nanotechnology*, 2012, 23, 365102.
43. Z. Liu, K. Yang and S.-T. Lee, *Journal of Materials Chemistry*, 2011, 21, 586-598.
44. T. A. Saleh and V. K. Gupta, *Journal of Colloid and Interface Science*, 2012, 371, 101-106.
45. M. Cargnello, M. Grzelczak, B. Rodríguez-González, Z. Syrgiannis, K. Bakhmutsky, V. La Parola, L. M. Liz-Marzán, R. J. Gorte, M. Prato and P. Fornasiero, *Journal of the American Chemical Society*, 2012, 134, 11760-11766.
46. V. K. Gupta, I. Ali, T. A. Saleh, A. Nayak and S. Agarwal, *RSC Advances*, 2012, 2, 6380-6388.
47. A. Safavi, N. Maleki and M. M. Doroodmand, *Analytica Chimica Acta*, 2010, 675, 207-212.
48. J.-L. Chen, *Journal of Chromatography A*, 2010, 1217, 715-721.
49. A. V. Herrera-Herrera, M. Á. González-Curbelo, J. Hernández-Borges and M. Á. Rodríguez-Delgado, *Analytica Chimica Acta*, 2012, 734, 1-30.
50. M. Keidar, *Journal of Physics D: Applied Physics*, 2007, 40, 2388.
51. C. D. Scott, S. Arepalli, P. Nikolaev and R. E. Smalley, *Appl Phys A*, 2001, 72, 573-580.
52. P. Nikolaev, M. J. Bronikowski, R. K. Bradley, F. Rohmund, D. T. Colbert, K. A. Smith and R. E. Smalley, *Chemical Physics Letters*, 1999, 313, 91-97.
53. S. Iijima, *Nature*, 1991, 354, 56-58.
54. Y. Zhang and S. Iijima, *Applied Physics Letters*, 1999, 75, 3087-3089.
55. Z. F. Ren, Z. P. Huang, J. W. Xu, J. H. Wang, P. Bush, M. P. Siegal and P. N. Provencio, *Science*, 1998, 282, 1105-1107.
56. V. Sgobba and D. M. Guldi, *Chemical Society Reviews*, 2009, 38, 165-184.

57. J. P. Salvetat, J. M. Bonard, N. H. Thomson, A. J. Kulik, L. Forró, W. Benoit and L. Zuppiroli, *Appl Phys A*, 1999, 69, 255-260.
58. N. Jha, P. Ramesh, E. Bekyarova, X. Tian, F. Wang, M. E. Itkis and R. C. Haddon, *Scientific Reports*, 2013, 3, 1.
59. T. Sawatsuk, A. Chindaduang, C. Sae-kung, S. Pratontep and G. Tumcharern, *Diamond and Related Materials*, 2009, 18, 524-527.
60. H. Imahori and T. Umeyama, *The Journal of Physical Chemistry C*, 2009, 113, 9029-9039.
61. X. Cui, F. Hu, W. Wei and W. Chen, *Carbon*, 2011, 49, 1225-1234.
62. J. Y. Lee, K. Liang, K. H. An and Y. H. Lee, *Synthetic Metals*, 2005, 150, 153-157.
63. S. W. Lee, J. Kim, S. Chen, P. T. Hammond and Y. Shao-Horn, *ACS Nano*, 2010, 4, 3889-3896.
64. C. K. Lin, C. H. Wu, C. Y. Tsai, C. Y. Chen and S. C. Wang, *Surface and Coatings Technology*, 2010, 205, 1595-1598.
65. P. Lin, Q. She, B. Hong, X. Liu, Y. Shi, Z. Shi, M. Zheng and Q. Dong, *Journal of The Electrochemical Society*, 2010, 157, A818-A823.
66. S. Zhang, C. Peng, K. C. Ng and G. Z. Chen, *Electrochimica Acta*, 2010, 55, 7447-7453.
67. G. Du, C. Zhong, P. Zhang, Z. Guo, Z. Chen and H. Liu, *Electrochimica Acta*, 2010, 55, 2582-2586.
68. X. Li, F. Kang and W. Shen, *Electrochemical and Solid-State Letters*, 2006, 9, A126-A129.
69. V. V. N. Obreja, *Physica E: Low-dimensional Systems and Nanostructures*, 2008, 40, 2596-2605.
70. W. Lu, L. Qu, K. Henry and L. Dai, *Journal of Power Sources*, 2009, 189, 1270-1277.
71. M. Hoefer and P. R. Bandaru, *Applied Physics Letters*, 2009, 95, -.
72. A. Peigney, C. Laurent, E. Flahaut, R. R. Bacsa and A. Rousset, *Carbon*, 2001, 39, 507-514.
73. Y. Yamada, O. Kimizuka, K. Machida, S. Suematsu, K. Tamamitsu, S. Saeki, Y. Yamada, N. Yoshizawa, O. Tanaike, J. Yamashita, F. Don, K. Hata and H. Hatori, *Energy & Fuels*, 2010, 24, 3373-3377.
74. A. B. Dalton, S. Collins, J. Razal, E. Munoz, V. H. Ebron, B. G. Kim, J. N. Coleman, J. P. Ferraris and R. H. Baughman, *Journal of Materials Chemistry*, 2004, 14, 1-3.
75. P. G. Whitten, G. M. Spinks and G. G. Wallace, *Carbon*, 2005, 43, 1891-1896.
76. Y. Shang, Y. Li, X. He, S. Du, L. Zhang, E. Shi, S. Wu, Z. Li, P. Li, J. Wei, K. Wang, H. Zhu, D. Wu and A. Cao, *ACS Nano*, 2012, 7, 1446-1453.
77. G. Xu, C. Zheng, Q. Zhang, J. Huang, M. Zhao, J. Nie, X. Wang and F. Wei, *Nano Research*, 2011, 4, 870-881.
78. M. Zhang, S. Fang, A. A. Zakhidov, S. B. Lee, A. E. Aliev, C. D. Williams, K. R. Atkinson and R. H. Baughman, *Science*, 2005, 309, 1215-1219.
79. D. N. Futaba, K. Hata, T. Yamada, T. Hiraoka, Y. Hayamizu, Y. Kakudate, O. Tanaike, H. Hatori, M. Yumura and S. Iijima, *Nature Materials*, 2006, 5, 987-994.
80. E. Frackowiak, V. Khomenko, K. Jurewicz, K. Lota and F. Béguin, *Journal of Power Sources*, 2006, 153, 413-418.

81. V. Khomenko, E. Frackowiak and F. Béguin, *Electrochimica Acta*, 2005, 50, 2499-2506.
82. P. Lv, Y. Y. Feng, Y. Li and W. Feng, *Journal of Power Sources*, 2012, 220, 160-168.
83. Y. Hou, Y. Cheng, T. Hobson and J. Liu, *Nano Letters*, 2010, 10, 2727-2733.
84. V. Singh, D. Joung, L. Zhai, S. Das, S. I. Khondaker and S. Seal, *Progress in Materials Science*, In Press, Corrected Proof.
85. A. K. Geim and K. S. Novoselov, *Nat Mater*, 2007, 6, 183-191.
86. J. Wintterlin and M. L. Bocquet, *Surface Science*, 2009, 603, 1841-1852.
87. R. S. Edwards and K. S. Coleman, *Nanoscale*, 2013, 5, 38-51.
88. D. A. C. Brownson, D. K. Kampouris and C. E. Banks, *Journal of Power Sources*, 2011, 196, 4873-4885.
89. M. Pumera, *Chemical Society Reviews*, 2010, 39, 4146-4157.
90. W. S. Hummers, Jr and R. E. Offeman, *J. Am. Chem. Soc.*, 1958, 80, 1339.
91. G. Eda, G. Fanchini and M. Chhowalla, *Nat Nano*, 2008, 3, 270-274.
92. S. Stankovich, D. A. Dikin, R. D. Piner, K. A. Kohlhaas, A. Kleinhammes, Y. Jia, Y. Wu, S. T. Nguyen and R. S. Ruoff, *Carbon*, 2007, 45, 1558-1565.
93. D. Yang, A. Velamakanni, G. Bozoklu, S. Park, M. Stoller, R. D. Piner, S. Stankovich, I. Jung, D. A. Field, C. A. Ventrice Jr and R. S. Ruoff, *Carbon*, 2009, 47, 145-152.
94. D. R. Dreyer, S. Park, C. W. Bielawski and R. S. Ruoff, *Chemical Society Reviews*, 2010, 39, 228-240.
95. K. Jo, T. Lee, H. J. Choi, J. H. Park, D. J. Lee, D. W. Lee and B.-S. Kim, *Langmuir*, 2011, 27, 2014-2018.
96. H. Bai, Y. Xu, L. Zhao, C. Li and G. Shi, *Chemical Communications*, 2009, 1667-1669.
97. A. Chunder, T. Pal, S. I. Khondaker and L. Zhai, *The Journal of Physical Chemistry C*, 2010, 114, 15129-15135.
98. J. Geng and H.-T. Jung, *The Journal of Physical Chemistry C*, 2010, 114, 8227-8234.
99. X. Wang, L. J. Yu, X. L. Wu, F. L. Yuan, Y. G. Guo, Y. Ma and J. N. A. Yao, *J. Phys. Chem. C*, 2009, 113, 15553.
100. M. D. Stoller, S. Park, Y. Zhu, J. An and R. S. Ruoff, *Nano Letters*, 2008, 8, 3498-3502.
101. H. M. Jeong, J. W. Lee, W. H. Shin, Y. J. Choi, H. J. Shin, J. K. Kang and J. W. Choi, *Nano Letters*, 2011, 11, 2472-2477.
102. W. Zhou, J. Liu, T. Chen, K. S. Tan, X. Jia, Z. Luo, C. Cong, H. Yang, C. M. Li and T. Yu, *Physical Chemistry Chemical Physics*, 2011, 13, 14462-14465.
103. E. Yoo, J. Kim, E. Hosono, H.-s. Zhou, T. Kudo and I. Honma, *Nano Letters*, 2008, 8, 2277-2282.
104. J. Yan, Z. Fan, T. Wei, W. Qian, M. Zhang and F. Wei, *Carbon*, 2010, 48, 3825-3833.
105. X.-h. Xia, J.-p. Tu, Y.-j. Mai, X.-l. Wang, C.-d. Gu and X.-b. Zhao, *Journal of Materials Chemistry*, 2011, 21, 9319-9325.
106. Z.-S. Wu, D.-W. Wang, W. Ren, J. Zhao, G. Zhou, F. Li and H.-M. Cheng, *Advanced Functional Materials*, 2010, 20, 3595-3602.
107. H.-W. Wang, Z.-A. Hu, Y.-Q. Chang, Y.-L. Chen, H.-Y. Wu, Z.-Y. Zhang and Y.-Y. Yang, *Journal of Materials Chemistry*, 2011, 21, 10504-10511.
108. X. Yang, C. Lu, J. Qin, R. Zhang, H. Tang and H. Song, *Materials Letters*, 2011, 65, 2341-2344.

109. H. A. Andreas and B. E. Conway, *Electrochimica Acta*, 2006, 51, 6510-6520.
110. T. Nathan, M. Cloke and S. R. S. Prabaharan, *J. Nanomaterials*, 2008, 2008, 1-8.
111. M. Toupin, T. Brousse and D. Bélanger, *Chemistry of Materials*, 2002, 14, 3946-3952.
112. R. N. Reddy and R. G. Reddy, *Journal of Power Sources*, 2003, 124, 330-337.
113. A. Taguchi, S. Inoue, S. Akamaru, M. Hara, K. Watanabe and T. Abe, *Journal of Alloys and Compounds*, 2006, 414, 137-141.
114. Y.-C. Chen, Y.-K. Hsu, Y.-G. Lin, Y.-K. Lin, Y.-Y. Horng, L.-C. Chen and K.-H. Chen, *Electrochimica Acta*, 2011, 56, 7124-7130.
115. H. Jiang, T. Zhao, C. Yan, J. Ma and C. Li, *Nanoscale*, 2010, 2, 2195-2198.
116. B. Wang, K. Konstantinov, D. Wexler, H. Liu and G. Wang, *Electrochimica Acta*, 2009, 54, 1420-1425.
117. K. Prasad and N. Miura, *Applied Physics Letters*, 2004, 85, 4199 - 4201.
118. M. Xu, L. Kong, W. Zhou and H. Li, *The Journal of Physical Chemistry C*, 2007, 111, 19141-19147.
119. T. Zhu, J. S. Chen and X. W. Lou, *Journal of Materials Chemistry*, 2010, 20, 7015-7020.
120. L. Wang, X. Liu, X. Wang, X. Yang and L. Lu, *Current Applied Physics*, 2010, 10, 1422-1426.
121. K. Naoi, *Journal of The Electrochemical Society* 2008, 17, 34-37.
122. J. P. Zheng and T. R. Jow, *Journal of The Electrochemical Society*, 1995, 142, L6-L8.
123. C. D. Lokhande, D. P. Dubal and O.-S. Joo, *Current Applied Physics*, 2011, 11, 255-270.
124. V. D. Patake, S. M. Pawar, V. R. Shinde, T. P. Gujar and C. D. Lokhande, *Current Applied Physics*, 2010, 10, 99-103.
125. K. Liang, X. Tang and W. Hu, *Journal of Materials Chemistry*, 2012, 22, 11062-11067.
126. T. Lu, Y. Zhang, H. Li, L. Pan, Y. Li and Z. Sun, *Electrochimica Acta*, 55, 4170-4173.
127. M. Salari, K. Konstantinov and H. K. Liu, *Journal of Materials Chemistry*, 2011, 21, 5128-5133.
128. J.-H. Kim, K. H. Lee, L. J. Overzet and G. S. Lee, *Nano Letters*, 2011, 11, 2611-2617.
129. Y. Gao, S. Chen, D. Cao, G. Wang and J. Yin, *Journal of Power Sources*, 2010, 195, 1757-1760.
130. S. G. Kandalkar, J. L. Gunjakar and C. D. Lokhande, *Applied Surface Science*, 2008, 254, 5540-5544.
131. G. Wang, X. Shen, J. Horvat, B. Wang, H. Liu, D. Wexler and J. Yao, *The Journal of Physical Chemistry C*, 2009, 113, 4357-4361.
132. L.-J. Xie, J.-F. Wu, C.-M. Chen, C.-M. Zhang, L. Wan, J.-L. Wang, Q.-Q. Kong, C.-X. Lv, K.-X. Li and G.-H. Sun, *Journal of Power Sources*, 2013, 242, 148-156.
133. T.-Y. Wei, C.-H. Chen, K.-H. Chang, S.-Y. Lu and C.-C. Hu, *Chemistry of Materials*, 2009, 21, 3228-3233.
134. V. Srinivasan and J. W. Weidner, *Journal of Power Sources*, 2002, 108, 15-20.

135. S. Devaraj and N. Munichandraiah, *Electrochemical and Solid-State Letters*, 2005, 8, A373-A377.
136. K. Rajendra Prasad and N. Miura, *Electrochemistry Communications*, 2004, 6, 1004-1008.
137. Z.-S. Wu, W. Ren, D.-W. Wang, F. Li, B. Liu and H.-M. Cheng, *ACS Nano*, 2010, 4, 5835-5842.
138. M.-S. Wu, *Applied Physics Letters*, 2005, 87, 153102-153103.
139. R. K. Sharma, H.-S. Oh, Y.-G. Shul and H. Kim, *Journal of Power Sources*, 2007, 173, 1024-1028.
140. X. Tang, H. Li, Z.-H. Liu, Z. Yang and Z. Wang, *Journal of Power Sources*, 2011, 196, 855-859.
141. S. W. Donne, A. F. Hollenkamp and B. C. Jones, *Journal of Power Sources*, 2010, 195, 367-373.
142. W. Yang, Z. Gao, J. Wang, B. Wang, Q. Liu, Z. Li, T. Mann, P. Yang, M. Zhang and L. Liu, *Electrochimica Acta*, 2012, 69, 112-119.
143. D. Wang, Y. Li, Q. Wang and T. Wang, *European Journal of Inorganic Chemistry*, 2012, 2012, 628-635.
144. D. Wang, W. Ni, H. Pang, Q. Lu, Z. Huang and J. Zhao, *Electrochimica Acta*, 2010, 55, 6830-6835.
145. C. Yuan, X. Zhang, L. Su, B. Gao and L. Shen, *Journal of Materials Chemistry*, 2009, 19, 5772-5777.
146. W. Lv, F. Sun, D.-M. Tang, H.-T. Fang, C. Liu, Q.-H. Yang and H.-M. Cheng, *Journal of Materials Chemistry*, 2011, 21, 9014-9019.
147. P. A. Thrower, *Carbon*, 2010, 48, 2675-2676.
148. K. H. An, K. K. Jeon, J. K. Heo, S. C. Lim, D. J. Bae and Y. H. Lee, *Journal of The Electrochemical Society*, 2002, 149, A1058-A1062.
149. X. Wang, G. Li, Z. Chen, V. Augustyn, X. Ma, G. Wang, B. Dunn and Y. Lu, *Advanced Energy Materials*, 2011, 1, 1089-1093.
150. Z. Chen, V. Augustyn, J. Wen, Y. Zhang, M. Shen, B. Dunn and Y. Lu, *Advanced Materials*, 2011, 23, 791-795.
151. X. Zhang, W. Shi, J. Zhu, D. J. Kharistal, W. Zhao, B. S. Lalia, H. H. Hng and Q. Yan, *ACS Nano*, 2011, 5, 2013-2019.
152. J. Lang, X. Yan and Q. Xue, *Journal of Power Sources*, 2011, 196, 7841-7846.
153. Z. Fan, J. Yan, T. Wei, L. Zhi, G. Ning, T. Li and F. Wei, *Advanced Functional Materials*, 2011, 21, 2366-2375.
154. C. J. Jafta, F. Nkosi, L. le Roux, M. K. Mathe, M. Kebede, K. Makgopa, Y. Song, D. Tong, M. Oyama, N. Manyala, S. Chen and K. I. Ozoemena, *Electrochimica Acta*, 2013, 110, 228-233.
155. J. Yan, T. Wei, W. Qiao, B. Shao, Q. Zhao, L. Zhang and Z. Fan, *Electrochimica Acta*, 2010, 55, 6973-6978.
156. M. Salari, S. H. Aboutalebi, K. Konstantinov and H. K. Liu, *Physical Chemistry Chemical Physics*, 2011, 13, 5038-5041.
157. S. Q. Chen and Y. Wang, *Journal of Materials Chemistry*, 2010, 20, 9735-9739.
158. J. Yan, T. Wei, B. Shao, F. Ma, Z. Fan, M. Zhang, C. Zheng, Y. Shang, W. Qian and F. Wei, *Carbon*, 2010, 48, 1731-1737.
159. X. Yang, C. Lu, J. Qin, R. Zhang, H. Tang and H. Song, *Materials Letters*, 2011, 65, 2341-2344.

160. D. Wang, R. Kou, D. Choi, Z. Yang, Z. Nie, J. Li, L. V. Saraf, D. Hu, J. Zhang, G. L. Graff, J. Liu, M. A. Pope and I. A. Aksay, *ACS Nano*, 2010, 4, 1587-1595.
161. X. Li, G. Zhang, X. Bai, X. Sun, X. Wang, E. Wang and H. Dai, *Nat Nano*, 2008, 3, 538-542.
162. S.-Y. Yang, K.-H. Chang, H.-W. Tien, Y.-F. Lee, S.-M. Li, Y.-S. Wang, J.-Y. Wang, C.-C. M. Ma and C.-C. Hu, *Journal of Materials Chemistry*, 2011, 21, 2374-2380.
163. Y. Shao, J. Wang, M. Engelhard, C. Wang and Y. Lin, *Journal of Materials Chemistry*, 20, 743-748.
164. D. Yu and L. Dai, *The Journal of Physical Chemistry Letters*, 2009, 1, 467-470.
165. T. Lu, L. Pan, H. Li, C. Nie, M. Zhu and Z. Sun, *Journal of Electroanalytical Chemistry*, 2011, 661, 270-273.
166. R. B. Rakhi, W. Chen, D. Cha and H. N. Alshareef, *Advanced Energy Materials*, 2012, 2, 381-389.
167. Y. Cheng, S. Lu, H. Zhang, C. V. Varanasi and J. Liu, *Nano Letters*, 2012, 12, 4206-4211.
168. S. H. Aboutalebi, M. M. Gudarzi, Q. B. Zheng and J.-K. Kim, *Advanced Functional Materials*, 2011, 21, 2978-2988.
169. R. Jalili, S. H. Aboutalebi, D. Esrafilzadeh, K. Konstantinov, S. E. Moulton, J. M. Razal and G. G. Wallace, *ACS Nano*, 2013, 7, 3981-3990.
170. J. E. Kim, T. H. Han, S. H. Lee, J. Y. Kim, C. W. Ahn, J. M. Yun and S. O. Kim, *Angewandte Chemie International Edition*, 2011, 50, 3043-3047.
171. X. Zhao, B. M. Sanchez, P. J. Dobson and P. S. Grant, *Nanoscale*, 2011, 3, 839-855.
172. V. Ganesh, S. Pitchumani and V. Lakshminarayanan, *Journal of Power Sources*, 2006, 158, 1523-1532.
173. L. Demarconnay, E. Raymundo-Piñero and F. Béguin, *Journal of Power Sources*, 2011, 196, 580-586.
174. H. Wang, Y. Liang, T. Mirfakhrai, Z. Chen, H. Casalongue and H. Dai, *Nano Research*, 2011, 4, 729-736.
175. Y. Xiao, Y. Cao, Y. Gong, A. Zhang, J. Zhao, S. Fang, D. Jia and F. Li, *Journal of Power Sources*, 2014, 246, 926-933.
176. G. Gourdin, P. H. Smith, T. Jiang, T. N. Tran and D. Qu, *Journal of Electroanalytical Chemistry*, 2013, 688, 103-112.
177. S. R. Sivakkumar, J. Y. Nerkar and A. G. Pandolfo, *Electrochimica Acta*, 2010, 55, 3330-3335.
178. X. Hu, Y. Huai, Z. Lin, J. Suo and Z. Deng, *Journal of The Electrochemical Society*, 2007, 154, A1026-A1030.
179. A. T. Chidembo, S. H. Aboutalebi, K. Konstantinov, C. J. Jafta, H. K. Liu and K. I. Ozoemena, *RSC Advances*, 2014, 4, 886-892.
180. L. W. Winkler, *Berichte der deutschen chemischen Gesellschaft*, 1888, 21, 2843-2854.
181. A. T. Chidembo, S. H. Aboutalebi, K. Konstantinov, D. Wexler, H. K. Liu and S. X. Dou, *Particle & Particle Systems Characterization*, 2014, 31, 465-473.
182. R. Jalili, S. H. Aboutalebi, D. Esrafilzadeh, R. L. Shepherd, J. Chen, S. Aminorroaya-Yamini, K. Konstantinov, A. I. Minett, J. M. Razal and G. G. Wallace, *Advanced Functional Materials*, 2013, 23, 5345-5354.

183. A. L. Ryland, *Journal of Chemical Education*, 1958, 35, 80.
184. V. Singh, D. Joung, L. Zhai, S. Das, S. I. Khondaker and S. Seal, *Progress in Materials Science*, 2011, 56, 1178-1271.
185. P. T. Kissinger and W. R. Heineman, *Journal of Chemical Education*, 1983, 60, 702.
186. D. Antiohos, K. Pingmuang, M. S. Romano, S. Beirne, T. Romeo, P. Aitchison, A. Minett, G. Wallace, S. Phanichphant and J. Chen, *Electrochimica Acta*, 2013, 101, 99-108.
187. Y. Wu, S. Liu, H. Wang, X. Wang, X. Zhang and G. Jin, *Electrochimica Acta*, 2013, 90, 210-218.
188. Q. Jiangying, G. Feng, Z. Quan, W. Zhiyu, H. Han, L. Beibei, W. Wubo, W. Xuzhen and Q. Jieshan, *Nanoscale*, 2013, 5, 2999-3005.
189. B. Wang, J. Park, C. Wang, H. Ahn and G. Wang, *Electrochimica Acta*, 2010, 55, 6812-6817.
190. J. W. Lee, A. S. Hall, J.-D. Kim and T. E. Mallouk, *Chemistry of Materials*, 2012, 24, 1158-1164.
191. L. Ni, X. Cheng, X. Wang, Y. Tao, Y. Shen, T. Zhang, H. Sun and A. Xie, *Ionics*, 2013, 19, 259-264.
192. N. N. Greenwood and A. Earnshaw, *Chemistry of the Elements* Oxford: Butterworth-Heinemann, 2 edn., 1997.
193. C.-C. Hu, Y.-T. Wu and K.-H. Chang, *Chemistry of Materials*, 2008, 20, 2890-2894.
194. H. Zhang, C. Liang, Z. Tian, G. Wang and W. Cai, *CrystEngComm*, 2011, 13, 1063-1066.
195. D. Portehault, S. Cassaignon, E. Baudrin and J.-P. Jolivet, *Journal of Materials Chemistry*, 2009, 19, 7947-7954.
196. Y. Li, H. Tan, O. Lebedev, J. Verbeeck, E. Biermans, G. Van Tendeloo and B.-L. Su, *Crystal Growth & Design*, 2010, 10, 2969-2976.
197. D. Portehault, S. Cassaignon, E. Baudrin and J.-P. Jolivet, *Chemistry of Materials*, 2007, 19, 5410-5417.
198. S. Chen, J. Zhu, Q. Han, Z. Zheng, Y. Yang and X. Wang, *Crystal Growth & Design*, 2009, 9, 4356-4361.
199. C.-K. Lin, K.-H. Chuang, C.-Y. Lin, C.-Y. Tsay and C.-Y. Chen, *Surface and Coatings Technology*, 2007, 202, 1272-1276.
200. D. R. Rolison, J. W. Long, J. C. Lytle, A. E. Fischer, C. P. Rhodes, T. M. McEvoy, M. E. Bourg and A. M. Lubers, *Chemical Society Reviews*, 2009, 38, 226-252.
201. K. Zhang, L. L. Zhang, X. S. Zhao and J. Wu, *Chemistry of Materials*, 22, 1392-1401.
202. J. N. Lekitima, K. I. Ozoemena, C. J. Jafta, N. Kobayashi, Y. Song, D. Tong, S. Chen and M. Oyama, *Journal of Materials Chemistry A*, 2013, 1, 2821-2826.
203. S.-H. Ng, J. Wang, D. Wexler, K. Konstantinov, Z.-P. Guo and H.-K. Liu, *Angewandte Chemie International Edition*, 2006, 45, 6896-6899.
204. S. Yang, X. Feng, S. Ivanovici and K. Müllen, *Angewandte Chemie International Edition*, 2010, 49, 8408-8411.
205. M.-S. Wu, Y.-A. Huang, C.-H. Yang and J.-J. Jow, *International Journal of Hydrogen Energy*, 2007, 32, 4153-4159.
206. Y. Wang, Z. Shi, Y. Huang, Y. Ma, C. Wang, M. Chen and Y. Chen, *The Journal of Physical Chemistry C*, 2009, 113, 13103-13107.

207. B. Wang, Y. Wang, J. Park, H. Ahn and G. Wang, *Journal of Alloys and Compounds*, 2011, 509, 7778-7783.
208. X. Xia, J. Tu, Y. Mai, R. Chen, X. Wang, C. Gu and X. Zhao, *Chemistry – A European Journal*, 2011, 17, 10898-10905.
209. D. Chao, X. Xia, C. Zhu, J. Wang, J. Liu, J. Lin, Z. Shen and H. J. Fan, *Nanoscale*, 2014, 6, 5691-5697.
210. A. T. Chidembo, S. H. Aboutalebi, K. Konstantinov, D. Wexler, H. K. Liu and S. X. Dou, *Particle & Particle Systems Characterization*, 2013, n/a-n/a.
211. H. K. Bisoyi and S. Kumar, *Chemical Society Reviews*, 2011, 40, 306-319.
212. S. H. Aboutalebi, S. Aminorroaya-Yamini, I. Nevirkovets, K. Konstantinov and H. K. Liu, *Advanced Energy Materials*, 2012, 2, 1439-1446.
213. Z. Xu, H. Sun, X. Zhao and C. Gao, *Advanced Materials*, 2013, 25, 188-193.
214. R. Jalili, S. H. Aboutalebi, D. Esrafilzadeh, R. L. Shepherd, J. Chen, S. Aminorroaya-Yamini, K. Konstantinov, A. I. Minett, J. M. Razal and G. G. Wallace, *Advanced Functional Materials*, 2013, n/a-n/a.
215. M. Moazzami Gudarzi, S. H. Aboutalebi, N. Yousefi, Q. B. Zheng, F. Sharif, J. Cao, Y. Liu, A. Xiao and J.-K. Kim, *MRS Online Proceedings Library*, 2011, 1344, null-null.
216. J. Kim, L. J. Cote, F. Kim, W. Yuan, K. R. Shull and J. Huang, *Journal of the American Chemical Society*, 2010, 132, 8180-8186.
217. N. Yousefi, M. M. Gudarzi, Q. Zheng, S. H. Aboutalebi, F. Sharif and J.-K. Kim, *Journal of Materials Chemistry*, 2012, 22, 12709-12717.
218. L. J. Cote, J. Kim, Z. Zhang, C. Sun and J. Huang, *Soft Matter*, 2010, 6, 6096-6101.
219. B. Dan, N. Behabtu, A. Martinez, J. S. Evans, D. V. Kosynkin, J. M. Tour, M. Pasquali and I. I. Smalyukh, *Soft Matter*, 2011, 7, 11154-11159.
220. M. G. Mohsen, A. S. Hamed, Y. Nariman, Z. Q. Bin, S. Farhad, C. Jie, L. Yayun, X. Allison and K. Jang-Kyo, *MRS Proceedings*, 2011, 1334, 2011.
221. Z. Xu and C. Gao, *ACS Nano*, 2011, 5, 2908-2915.
222. L. Onsager, *Annals of the New York Academy of Sciences*, 1949, 51, 627-659.
223. E. M. Pouget, P. H. H. Bomans, J. A. C. M. Goos, P. M. Frederik, G. de With and N. A. J. M. Sommerdijk, *Science*, 2009, 323, 1455-1458.
224. J. Baumgartner, A. Dey, P. H. H. Bomans, C. Le Coadou, P. Fratzl, N. A. J. M. Sommerdijk and D. Faivre, *Nat Mater*, 2013, advance online publication.
225. L. Qiu, X. Yang, X. Gou, W. Yang, Z.-F. Ma, G. G. Wallace and D. Li, *Chemistry – A European Journal*, 2010, 16, 10653-10658.
226. J. W. Lee, T. Ahn, J. H. Kim, J. M. Ko and J.-D. Kim, *Electrochimica Acta*, 2011, 56, 4849-4857.
227. Q. Li, J. Liu, J. Zou, A. Chunder, Y. Chen and L. Zhai, *Journal of Power Sources*, 2011, 196, 565-572.
228. P. L. Taberna, P. Simon and J. F. Fauvarque *Journal of The Electrochemical Society*, 2003, 150, A292-A300.
229. M. E. Orazem, N. Pébère and B. Tribollet, *Journal of The Electrochemical Society*, 2006, 153, B129-B136.
230. C.-C. Hu and C.-C. Wang, *Journal of The Electrochemical Society*, 2003, 150, A1079-A1084.

PUBLICATIONS

1. S. H. Aboutalebi, **A. T. Chidembo**, M. Salari, K. Konstantinov, D. Wexler, H. K. Liu and S. X. Dou, *Energy & Environmental Science*, 2011, **4**, 1855-1865.

2. **A. Chidembo**, S. H. Aboutalebi, K. Konstantinov, M. Salari, B. Winton, S. A. Yamini, I. P. Nevirkovets and H. K. Liu, *Energy & Environmental Science*, 2012, **5**, 5236-5240.

3. M. Salari, S. H. Aboutalebi, **A. T. Chidembo**, I. P. Nevirkovets, K. Konstantinov and H. K. Liu, *Physical Chemistry Chemical Physics*, 2012, **14**, 4770-4779.

4. M. Salari, M. Rezaee, **A. T. Chidembo**, K. Konstantinov and H. K. Liu, *Journal of Nanoscience and Nanotechnology*, 2012, **12**, 4724-4728

5. **A. T. Chidembo**, S. H. Aboutalebi, K. Konstantinov, D. Wexler, H. K. Liu and S. X. Dou, *Particle & Particle Systems Characterization*, 2014, **31**, 465-473

6.

7. M. Salari, S. H. Aboutalebi, **A. T. Chidembo**, K. Konstantinov and H. K. Liu, *Journal of Alloys and Compounds*, 2014, **586**, 197-201.

8. **A. T. Chidembo**, S. H. Aboutalebi, K. Konstantinov, C. J. Jafta, H. K. Liu and K. I. Ozoemena, *RSC Advances*, 2014, **4**, 886-892.